BINARY HYPOTHESES FOR BIPOLAR MASS LOSS IN TRANSIENTS

by

Benedict Fitzpatrick

Submitted in conformity with the requirements
for the degree of Doctor of Philosophy
Subdepartment of Astrophysics
University of Oxford

Contents

1 Introduction **13**

1.1 Transients 13

1.2 Bipolar Mass Loss 14

1.3 Chemical evolution 16

1.4 Thesis outline 17

2 Smoothed Particle Hydrodynamics **19**

2.1 Introduction 19

2.2 Description 20

2.3 Gadget-2 and Implementation 26

2.3.1 Introduction 26

2.3.2 Rescaling units for Gadget 27

2.4 Initial conditions creation 28

2.4.1 Introduction 28

2.4.2 Particle distribution 28

2.4.3 Relaxation and Repressuring 29

2.4.4 Standard parameters 29

2.4.5 Plotting 30

2.5 Test cases 30

2.5.1 Sod shock tube 30

2.5.2 Wind code 32

2.5.3 Adiabatic collapse 34

2.5.4 Isothermal sphere 35

3 SN 1987A **40**
3.1 Introduction . . . 40
3.2 Background . . . 41
3.3 Inner Nebula . . . 41
3.4 Outer Nebula and Light Echoes . . . 42
3.5 Modelling background . . . 52
3.6 Binary hypothesis and reproduction of the inner nebula . . . 53
3.7 Method . . . 55
3.8 Results . . . 57
3.8.1 Parameter study - raw hydrodynamics . . . 57
3.8.2 Non-isotropic mass loss . . . 63
3.8.3 Simulation light echoes . . . 70
3.8.4 Offset study . . . 76
3.9 Conclusion . . . 78

4 Cassiopeia A **80**
4.1 Introduction . . . 80
4.2 Core-collapse supernovae and Cas A . . . 85
4.3 Binary hypothesis . . . 87
4.4 Modelling . . . 89
4.4.1 Primary jet . . . 89
4.4.2 Secondary jet . . . 101
4.5 Discussion . . . 107
4.6 Conclusion . . . 107
4.7 Future work . . . 108

5 Common envelope mergers and their ejecta **109**
5.1 Introduction . . . 109
5.2 Method . . . 113
5.3 Results . . . 117
5.3.1 Density profiles after spinup . . . 117
5.3.2 Explosion evolution . . . 120
5.3.3 Energy, momentum and structure effects . . . 125

5.3.4 Effects of energy deposition method 129
5.3.5 Adiabatic index effects 136
5.3.6 Extremely low mass loss 138
5.3.7 Planetary Nebulae 138
5.3.8 Population studies 139
5.3.9 Observability 139
5.4 Conclusion 140

6 Eta Carinae **141**
6.1 Introduction 141
6.2 Eta Carinae A and B 142
6.3 The Homunculus 142
6.4 Modelling the Homunculus 143
6.5 Binary companion and common envelope modelling 146
6.6 Testing the triple hypothesis 149
6.7 Method 149
6.8 Results 152
6.9 Discussion and future work 162

7 Conclusion **163**

8 Bibliography **166**

9 Appendices **175**
9.1 Geometric Warping 175
9.1.1 Introduction 175
9.1.2 Derivation 176

List of Figures

1.1 Messier 27 15

2.1 2D SPH kernel 25
2.2 Shock tube density profile 33
2.3 Shock tube internal energy profile 33
2.4 Shock tube internal energy profile 34
2.5 Radial velocity profile after rebound 36
2.6 Entropy radial profile after rebound 37
2.7 Isothermal collapse 37
2.8 Isothermal collapse, slightly higher viscosity 38
2.9 Isothermal collapse, lower softening 38
2.10 Isothermal collapse, higher viscosity 39
2.11 Isothermal collapse parameter study 39

3.1 Spherical shell 42
3.2 Spherical shell echo 43
3.3 Cylindrical shell echo 44
3.4 Tilted cylindrical shell 46
3.5 Tilted cylindrical shell echo 47
3.6 Napoleon's hat in 87A 48
3.7 Early light echoes near 1987A (Sugerman et al. 2005) 49
3.8 Later light echoes near 1987A (Sugerman et al. 2005) 50
3.9 Outer nebula structure in 87A 51
3.10 SN 1987A origin hypothesis (Morris and Podsiadlowski 2007) . . . 54
3.11 Outer 87A structure simulation 58

3.12 Density structures, v=350, a=10 60
3.13 Density structures, v=350, a=15 61
3.14 Density structures, v=350, a=20 61
3.15 Lower mass loss density structure in finished simulation - 20,350,15 62
3.16 Lower mass loss density structure in finished simulation - 30,350,15 63
3.17 Density structure in different density profiles 64
3.18 Distorted pre-merger RSG wind density structure, z*2 - 20,350,10 . 65
3.19 Distorted pre-merger RSG wind density structure, z*2 - 20,350,20 . 65
3.20 Distorted pre-merger RSG wind density structure, z*2 - 30,350,10 . 66
3.21 Distorted pre-merger RSG wind density structure, z*2 - 30,350,20 . 67
3.22 Distorted pre-merger RSG wind density structure rxy*2 - 20,350,10 68
3.23 Distorted pre-merger RSG density structure rxy*4 - 20,350,20 . . . 68
3.24 Distorted pre-merger RSG wind density structure rxy*2 - 30,350,10 69
3.25 Distorted pre-merger RSG wind density structure rxy*4 - 30,350,20 69
3.26 Early light echo, velocities and opening angle 350,10 70
3.27 Early light echo, velocities and opening angle 350,15 71
3.28 Early light echo, velocities and opening angle 350,20 71
3.29 Early light echo angle scattering 72
3.30 Lower mass loss - early light echo, velocities and opening angle 20,350,15 73
3.31 Lower mass loss - early light echo, velocities and opening angle 20,350,15 73
3.32 Late light echo, velocities and opening angle 350,10 74
3.33 Late light echo, velocities and opening angle 350,15 74
3.34 Late light echo, velocities and opening angle 350,20 75
3.35 Small NW offset echoes 77
3.36 Echo Red Blue difference 77

4.1 Cas A in X-rays 81
4.2 Cas A Chandra million second 82
4.3 Cas A knots 83
4.4 Cas A binary origin schematic 88
4.5 Early jet production 90

4.6 Later jet production 91
4.7 Late jet production 92
4.8 Early jet production coloured by radial velocity 94
4.9 Later jet production coloured by radial velocity 95
4.10 Late jet production coloured by radial velocity 96
4.11 Primary jet cross section 98
4.12 Primary jet radial origins 99
4.13 Primary jet small parameter study 100
4.14 Water droplet double jet 101
4.15 Displaced core jet 103
4.16 Displaced core schematic 104
4.17 Secondary jet, velocity and alpha 1000 and 0.4 105
4.18 Secondary jet, velocity and alpha 1000 and 0.8 105
4.19 Secondary jet, velocity and alpha 2000 and 0.8 106

5.1 Common envelope process schematic 112
5.2 Polytrope density profiles 114
5.3 Polytrope spinup coloured by density 118
5.4 Polytrope spinup coloured by density 119
5.5 Deposition of energy, early - low index polytrope 121
5.6 Deposition of energy, late - low index polytrope 122
5.7 Deposition of energy, early - high index polytrope 123
5.8 Deposition of energy, late - low index polytrope 124
5.9 Ejecta position plots 126
5.10 Ejecta velocity plots 127
5.11 Ejecta mass per solid angle histograms 128
5.12 Energy deposition effects - ejecta position plots 129
5.13 Energy deposition effects - ejecta velocity plots 130
5.14 Energy deposition effects - ejecta mass per solid angle 131
5.15 Geometry effects - ejecta position plots 133
5.16 Geometry effects - ejecta velocity plots 134
5.17 Geometry effects - ejecta mass per solid angle plots 135
5.18 Adiabatic index effects - ejecta position plots 137

6.1 Eta Car HST image 144
6.2 Common envelope origin schematic for Eta Car 147
6.3 Orbit limits - outer companion mass 150
6.4 Orbit limits - outer companion eccentricity 151
6.5 Wind profile from Smith et al. (2003) 153
6.6 Polynomial fit to wind profile 154
6.7 Model star ejecta at very early times 155
6.8 Model star ejecta wind simulation 156
6.9 Low index polytrope ejecta wind simulation, standard mass loss . . 157
6.10 Low index polytrope ejecta wind simulation, twice the mass loss . . 158
6.11 Low index polytrope ejecta wind simulation, 4 times the mass loss . 159
6.12 High index polytrope ejecta wind simulation, standard mass loss . . 160
6.13 High index polytrope ejecta wind simulation, twice the mass loss . . 161

Abstract

Binary Hypotheses for Bipolar Mass Loss in Transients

Benedict Fitzpatrick

We investigate binary hypotheses for the formation of bipolar nebulae using the smoothed particle hydrodynamics code Gadget-2. In the general case, we present a parameter study of mass loss from very simple common envelope models, which seems to show a strongly bipolar trend for sufficiently oblate envelopes and low enough spiral-in injection energy. The density profiles of the envelopes produce differing structure within the ejecta.

We also investigate 3 specific bipolar mass loss events. In the case of the outer nebula of SN 1987A, we study the effects of fast polar jets interacting with a pre-existing progenitor wind and find that these are consistent with the observed light echoes from the nebula, in particular for the feature known as 'Napoleon's Hat'. In the case of Cas A, we briefly study the effects of close binarity on supernova ejecta and suggest the influence of a close, compact companion may lead to at least one jet-like disturbance that may be observable in a supernova remnant. Finally, we study whether a fast bipolar wind, similar to that of Eta Car's present wind, may inflate ejecta similar to that produced in the common envelope models to a shape consistent with that of Eta Car's Homunculus Nebula.

Dedication

To Fiona

Acknowledgements

I would like to firstly thank Philipp Podsiadlowski for such an inspiring and enjoyable few years at Oxford. Thanks to the Science and Technology Facilities Council (STFC) for funding this project, and to the UK Met Office for giving me a great job while and after I wrote it up. I'd like to thank my mother for giving me a place to stay in the last 2 months writing up in Oxford, and my family in general. I would also like to thank my fellow members of the subdepartment, past and present, for support, sociability, and friendship. Thanks in particular to all the students who have been officemates as well, who have put up with mess, many, many coffee cups, and minor (sometimes major) distractions.

Declaration

The material contained within this report has not previously been submitted for a degree at the University of Oxford or any other university. The research reported within this report has been conducted by the author unless indicated otherwise.

Copyright Notice

Chapter 1

Introduction

1.1 Transients

The term transient is a label that is increasingly used to define some of the most interesting phenomena in stellar astrophysics. Broadly, it defines astrophysical observations of 'things that go bump in the night' - time dependent, galactically or extra-galactically located electromagnetic sources that are increasingly the focus of optical surveys such as Skymapper, PANSTARRS, the Palomar Transient Factory and others. It is also a catch-all for X-ray, radio, IR, UV and gravitational radiation time-varying sources.

Objects that exhibit human-level time variance mark a departure from a universe that measures time in galactic dynamical times or main-sequence lifetimes. We have gone from a 'celestial sphere' that was thought to be fundamentally unchanging (if with some periodicity with systems such as Algol) in medieval times until the evidence from the first documented observed 'nova' (SN 1572). In the modern day, instrumentation advances and heavily automated observation mean that many hundreds of supernovae, not to mention other transients, are detected per year.

Observed transients consist of a range of luminosities and rarities. There are statistically unlikely events in time, such observing the of order 100-day light curve of a core collapse supernova of a single massive star, whose observability (power in the electromagnetic spectrum) counteracts the sample size. There are also more frequent events, such as recurrent novae, that are relatively populous in the nearby

universe but may be far less luminous. Happily, in the case of stellar transients, the most time-infrequent events, or the most dynamic, seem to coincide with the most observable changes in luminosity (with the honourable exception of black hole mergers).

The class of transients, and stellar transients in particular for this thesis, therefore contains observed events such as supernovae, stellar flares, eclipsing and sunspotted stars, gamma ray bursts, soft gamma ray repeaters, pulsars, novae, neutron star quakes, black hole mergers, tidal disruption by a black hole, luminous red novae and others.

In general, any astrophysical phenomenon that varies in our timescales gives us much more specific information about the the physics of the source itself than normal near-static observations across a population. There are rare events within space and rare events within time - the new observational era (the imaging revolution) at its best gives us both. Theory must ramp up to drive, and match, the onslaught of new discoveries.

1.2 Bipolar Mass Loss

Many astrophysical objects exhibit bipolarity, which implies they have a preferred axis in mass distribution, kinematics, composition or emission.

A preferred axis implies a fundamental asymmetry at the heart of the object - angular momentum, in the case of spiral galaxies such as Andromeda, geometrical alignment such as phases of planets and reflection nebulae, poles of magnetic fields (themselves driven in stars and planets by rotation), movement through some ambient medium in the case of objects such as Mira and comets, and gravitational influence on certain perturbed mass distributions such as cosmic filaments.

Fundamentally, the properties of the object are different in one direction than another. When trying to understand astrophysical processes, morphological asymmetry such as bipolarity offers a valuable set of constraints - such as the still mysterious origin of the first planetary nebula discovered, and many like it (M27, Figure 1.1).

The manifestation of the asymmetry can be varied, from jet vectors defined by angular momentum and magnetic fields in active galactic nuclei (AGN), young

Figure 1.1: Messier 27, the first planetary nebula discovered, is strongly bipolar, with a bi-conical structure in the plane of the sky (e.g. Kwok et al. 2008). Image credit: Joe and Gail Metcalf / Adam Block / NOAO / AURA / NSF

stellar objects (YSOs) and pulsars, mass transfer defined and distorted by the gravitational geometry, to polar or equatorially enhanced mass loss from high angular momentum oblate stars.

In this thesis we will discuss various possible mechanisms for the bipolar asymmetry in supernova remnants (Cas A), planetary nebulae (through a study of common envelope ejecta), unsolved giant eruption (η Carinae), and progenitor mass loss (SN 1987A).

This thesis describes bipolar mass loss in the context of stellar astrophysics, where preferred axes arise from stellar rotation, binarity (including multiple systems), and magnetic fields. All of these mechanisms can be linked - high stellar angular momentum can result from tidal or merger spinup in a binary, and magnetic fields act to brake pre-main sequence stars to lower angular momenta to the point at which after leaving the main sequence they may require spinup to create any significant preferred axis. The same magnetic fields are strongly dependent on rotation, although their axis by no means has to be aligned near the rotation axis, and they may in fact be strongly multi-polar in many cases.

We do not examine the role of magnetic fields in shaping bipolar mass loss in detail in this thesis, although it is a rapidly advancing field of research in, for example, the planetary nebula community. We examine the role of binaries and multiple star systems in shaping mass loss, and provide evidence to support a binary hypothesis for bipolar mass loss in the areas we cover.

1.3 Chemical evolution

Big Bang nucleosynthesis is well constrained to produce almost none of the heavier elements past beryllium that we see in the universe today.

These are produced in stars as a result of the triple alpha process leading to fusing of existing nuclei and successively heavier products until nickel - the elements heavier than this being produced by slow or rapid neutron capture (s and r-process) by nuclei in conditions such as in asymptotic giant branch (AGB) stellar winds and in the classes of supernovae.

The extent to which stars enrich their surroundings and influence future star formation through their mass loss and supernova shocks is one of the major areas of

study in galaxy formation and evolution. Supernovae shocks can not only compress over-dense regions into the formation of stars, but they can enrich their surroundings to the point that dramatic line cooling from the heavy elements leaches energy, and they cool and fragment (see e.g. Slyz et al. 2005).

Mass loss from AGB stars, common envelope ejection, and giant eruptive variables such as Eta Carinae also has a large effect on the surrounding ISM. Asymmetry in kinematics or chemical abundance could affect the penetration of the enriched material into the surrounding ISM, and potentially enhance local chemical inhomogeneities (Sam Geen, private communication). The trend in hydrodynamical galaxy evolution simulations is to treat mass loss as spherical with isotropic chemical abundances, but in the case of Eta Carinae and Cas A the elemental abundances are either skewed to particular axes or missing altogether in certain directions.

1.4 Thesis outline

This thesis will describe binary hypotheses for bipolar mass loss in several transients and planetary nebulae, reproducing morphologies and kinematics with hydrodynamical modelling.

Chapter 2 describes the hydrodynamical method, smoothed particle hydrodynamics, and the particular code used, Gadget-2. It explains the choice of code and the particular method of solving the fluid equations.

Chapter 3 continues the work of Thomas Morris and Philipp Podsiadlowski (Morris & Podsiadlowki 2007) in providing evidence for a binary merger origin for the nebulae around SN 1987A - in this case, the outer bipolar nebulae and the light echo features within it, such as the famous 'Napoleon's hat'.

Chapter 4 contains a study of the asymmetric supernova remnant Cas A which presents a new origin method, based on binary interaction, for the main jets and reproduces most of the peculiarities of the remnant.

Chapter 5 discusses the differing morphologies produced by shocked, spunup polytropic model envelopes and the implications for bipolar objects such as some planetary nebulae.

Chapter 6 continues Chapter 5 in methodology, but attempts to model the Homunculus nebula of Eta Carinae by incorporating an interacting winds model.

Finally, Chapter 7 summarises the results and conclusions of this thesis.

Chapter 2

Smoothed Particle Hydrodynamics

2.1 Introduction

Smoothed Particle Hydrodynamics (SPH) is a Lagrangian based approach to computational fluid dynamics developed by Lucy (1977) and Gingold & Monaghan (1977). Instead of discretising the fluid as sets of grid points (the Eulerian approach), tracer particles are mapped onto the density distribution, and used as interpolation points for the local fluid properties. Each particle's properties are determined by a local interpolation of the properties of the nearest neighbours, through an appropriate function of the separation of the particles. The cut off separation beyond which a particle has no direct influence on the other is the SPH smoothing length h (or $2\mathrm{h}$ in most codes), and defines a natural resolution minimum. In most modern SPH codes such as Gadget-2, the smoothing length is allowed to vary for each particle, defined by a set number of neighbours that a particle is allowed to influence. This allows a very high dynamic range, equalling or surpassing current grid based methods in refinement on density.

The principal strength of SPH methods is their Lagrangian nature. They obey easily-defined conservation laws (naturally conserving mass) and do not require the 'advection' of fluid properties due to bulk motion, as in grid methods. As the approach is based on following flow, rather than mapping a volume, they trace structure naturally through the movement of the particles - equivalent to a continual (and very cost-efficient) remapping of grid points. This is especially important in prob-

lems with non-trivial geometries, in which calculating distributions of grid points can be computationally expensive. This ability has the the associated penalty of only being able to map the density structure, rather than the distribution of other variables such as the divergence of the velocities or accelerations.

SPH methods also suffer from relatively poor resolution of shocks (in more than 1 dimension) - the particular nature of the discretisation universally results in a smearing of the shock over smoothing lengths, while grid based methods can target and adapt to shock fronts, resolving them more precisely. SPH methods also rely on an 'artificial viscosity' formulation to accurately simulate the entropy generation of shocks and the behaviour of the fluid near fronts (see e.g. Monaghan 1984). This, in essence, prevents particles from approaching too closely or freely interpenetrating, while parametrising shock microphysics. While these are tailored to reduce unphysical results, the need for this 'ad hoc' addition is a flaw in the SPH approach.

However, SPH offers numerous other advantages. It conserves mass, momentum and energy (or entropy) naturally in modern formulations. It is generally relatively easy to add new physics, and it allows for simultaneous simulation of components of different types and masses. SPH was chosen for this thesis above all other reasons for the geometric fluency of the approach, which allows rigorous exploration of the morphology parameter space.

2.2 Description

It is necessary to distinguish between Eulerian and Lagrangian methods of tracking changes in fluid properties. In the Eulerian picture, a volume element or grid cell is modelled, through which the fluid may flow - the rate of change of the cell fluid properties with respect to time needs to incorporate a term dealing with the inflow and outflow of fluid with slightly different properties. In the Lagrangian picture, a parcel of fluid is followed along its path, and there is no need for this extra term. This makes the Lagrangian fluid equations simpler, as can be seen by writing the material (or total) derivative:

$$\frac{\mathrm{D}\psi(\mathbf{x},t)}{\mathrm{D}t} = \frac{\partial\psi(\mathbf{x},t)}{\partial t} + \frac{\mathrm{d}\mathbf{x}}{\mathrm{d}t} \cdot \nabla\psi(\mathbf{x},t) \tag{2.1}$$

where the left hand side of the equation (LHS) is the time derivative of a scalar field $\psi(\mathbf{x},t)$ in the Lagrangian picture, and the right hand side of the equation (RHS) contains the partial time derivative from the Eulerian picture.

The rate of change of density of our parcel of fluid is:

$$\frac{\mathrm{D}\rho}{\mathrm{D}t} = \frac{\mathrm{d}}{\mathrm{d}t}(\frac{\Delta M}{\Delta V}) = \frac{1}{\Delta V^2}(\Delta V\frac{\mathrm{d}\Delta M}{\mathrm{d}t} - \Delta M\frac{\mathrm{d}\Delta V}{\mathrm{d}t}) \tag{2.2}$$

where, in the Lagrangian paradigm, the change of mass with time $\frac{\mathrm{d}\Delta M}{\mathrm{d}t}$ in our fluid element is zero, so the expression reduces to:

$$\frac{\mathrm{D}\rho}{\mathrm{D}t} = -\frac{\Delta M}{\Delta V^2}(\frac{\mathrm{d}\Delta V}{\mathrm{d}t}) = -\frac{\rho}{\Delta V}\frac{\mathrm{d}\Delta V}{\mathrm{d}t} \tag{2.3}$$

and taking $\Delta V = \Delta x\Delta y\Delta z$,

$$\frac{\mathrm{D}\rho}{\mathrm{D}t} = -\frac{\rho}{\Delta V}(\Delta y\Delta z\frac{\mathrm{d}\Delta x}{\mathrm{d}t} + \Delta x\Delta z\frac{\mathrm{d}\Delta y}{\mathrm{d}t} + \Delta x\Delta y\frac{\mathrm{d}\Delta z}{\mathrm{d}t}) \tag{2.4}$$

which is

$$\frac{\mathrm{D}\rho}{\mathrm{D}t} = -\frac{\rho}{\Delta V^2}(\frac{1}{\Delta x}\frac{\mathrm{d}\Delta x}{\mathrm{d}t} + \frac{1}{\Delta y}\frac{\mathrm{d}\Delta y}{\mathrm{d}t} + \frac{1}{\Delta z}\frac{\mathrm{d}\Delta z}{\mathrm{d}t}) \tag{2.5}$$

The change in extent of the fluid element along one axis is just the differential velocity between the two extremes multiplied by the (infinitesimal) time interval:

$$\mathrm{d}(\Delta x) = \Delta v_x \mathrm{d}t \tag{2.6}$$

and so

$$\frac{\mathrm{D}\rho}{\mathrm{D}t} = -\rho(\frac{1}{\Delta x}\Delta v_x + \frac{1}{\Delta y}\Delta v_y + \frac{1}{\Delta z}\Delta v_z) \tag{2.7}$$

which in the limit of $\Delta V -> 0$ becomes

$$\frac{\mathrm{D}\rho}{\mathrm{D}t} = -\rho(\frac{\partial v_x}{\partial x} + \frac{\partial v_y}{\partial y} + \frac{\partial v_z}{\partial z}) \tag{2.8}$$

If we then express the RHS term in brackets as the divergence of the velocity,

this gives us:

$$\frac{\mathrm{D}\rho}{\mathrm{D}t} = -\rho\nabla\cdot\mathbf{v} \tag{2.9}$$

which is the Lagrangian form of the continuity equation. This is an expression of the principle of conservation of mass, which is implicitly obeyed in standard Lagrangian computational fluid dynamics formulations such as SPH (discussed below) with fixed particle (very roughly analogous to parcel) numbers and masses.

The forces acting to accelerate our parcel of fluid arise from the integrated pressure force over the surface of our fluid parcel:

$$F_P = \int P\mathrm{d}\mathbf{S} = -\int \nabla P\mathrm{d}V \tag{2.10}$$

using Greens theorem, and from gravity:

$$F_G = \int \rho\mathbf{g}dV \tag{2.11}$$

We then have the rate of change of momentum in our parcel as

$$\int \rho\frac{\mathrm{D}\mathbf{v}}{\mathrm{D}t}\mathrm{d}V = F_P + F_G \tag{2.12}$$

and finally:

$$\frac{\mathrm{D}\mathbf{v}}{\mathrm{D}t} = -\frac{\nabla P}{\rho} + \mathbf{g} \tag{2.13}$$

The rate of change of internal energy of our parcel of fluid follows from the first law of thermodynamics, which for adiabatic processes is simply:

$$\mathrm{d}U = -P\mathrm{d}V \tag{2.14}$$

where U is the total internal energy, P pressure, and V volume. For our parcel of fluid, it is convenient to work with the specific internal energy, or internal energy per unit mass, u. Since the mass m is constant, our $\mathrm{d}V$ term becomes:

$$\mathrm{d}V = \mathrm{d}(\frac{m}{\rho}) = -\frac{m}{\rho^2}\mathrm{d}\rho \tag{2.15}$$

which, dividing by parcel mass, results in:

$$\mathrm{d}u = \frac{P}{\rho^2}\mathrm{d}\rho \tag{2.16}$$

taking the time derivative, and using our result from Equation 2.9, gives us a time derivative of specific internal energy for our fluid parcel of

$$\frac{\mathrm{d}u}{\mathrm{d}t} = -\frac{P}{\rho}\nabla \cdot \mathbf{v} \tag{2.17}$$

SPH is a computational hydrodynamics approach that treats a fluid in a Lagrangian fashion by sampling it with tracer points. Each of these is responsible for a given mass of fluid, but requires a summation over its nearest neighbours to recover fluid properties - this collection of neighbours around a particle is analogous to the fluid parcel described above. The tracer particle number density follows the fluid density (for equal mass points).

A fluid property $\psi(\mathbf{r})$ is approximately recovered by integrating over nearby space, using a smoothing or weighting function that gives increasing weight to decreasing distances $\mathbf{r}'$, and cuts off at a maximum distance h:

$$\psi(\mathbf{r}) = \int \psi(\mathbf{r}')W(\mathbf{r}-\mathbf{r}', h)\mathrm{d}\mathbf{r}' \tag{2.18}$$

The weighting function should be normalised such that

$$\int W(\mathbf{r}-\mathbf{r}')dV' = 1 \tag{2.19}$$

and approach a delta function at very small h.

The value of the fluid property in the SPH method, 'at' a given position $\mathbf{r}$ is given by the summation

$$\psi(\mathbf{r}) = \sum_N \psi_n \frac{m_n}{\rho_n} W(\mathbf{r}-\mathbf{r_n}, h) \tag{2.20}$$

where our previous integration over volume has been discretised, and substituted for a summation of mass over density. Essentially, only a set of the nearest N particles, no further away than a maximum distance h, are allowed to contribute, with contributions weighted by their distance and their $\frac{m_n}{\rho_n}$ value.

The density calculated at a tracer point is therefore calculated via:

$$\rho(\mathbf{r}) = \sum_{N} m_n W(\mathbf{r} - \mathbf{r_n}, h) \tag{2.21}$$

which is substantially more accurate than a raw density calculation using approximately the same set of particles, for good choices of kernel. Common choices are truncated Gaussians, or cubic splines. For example, in the SPH code we use (described in section 2.3) the 3D kernel is as follows:

$$W = 0, (r > h) \tag{2.22}$$

$$W = \frac{8}{\pi h^3}\left(2\left[1 - \frac{r}{h}\right]^3\right), \left(\frac{h}{2} < r \leq h\right) \tag{2.23}$$

$$W = \frac{8}{\pi h^3}\left(1 - 6\left[\frac{r}{h}\right]^2 + 6(\frac{r}{h})^3\right), \left(0 \leq r < \frac{h}{2}\right) \tag{2.24}$$

where r is our $\sum |\mathbf{r} - \mathbf{r_n}|$, the absolute distance between the particles, and the first term is a normalisation. The kernel thus has units of inverse volume.

A qualitative plot of this particular kernel, adapted to 2D, is shown for an N of 33 particles in Figure 2.1. The kernel strongly favours a few nearby particles in the density estimate.

The pressure in an entropy formulation of SPH is given by $\mathrm{P_i} = \mathrm{A_i}\rho_\mathrm{i}^\gamma$, where $\mathrm{A_i}$ is the entropy of the particle and γ the adiabatic index of the gas. This then defines the accelerations of the particles as

$$\begin{aligned}\frac{dv_i}{dt} = -\sum_{j=0}^{N_{\mathrm{ngb}}-1} m_j(f_i A_i \rho_i^{\gamma-2}\nabla_i W(r_{ij}, h_i) + \\ f_j A_j \rho_j^{\gamma-2}\nabla_i W(r_{ij}, h_j) + \\ \Pi_{ij}\nabla_i \frac{W(r_{ij}, hi) + W(r_{ij}, hj)}{2})\end{aligned} \tag{2.25}$$

where the last term is an 'artificial viscosity' (see Springel, 2005) that damps kinetic energy into the entropy parameter A_i in the presence of shock-triggering criteria and f is a correcting factor for the variation of density with smoothing

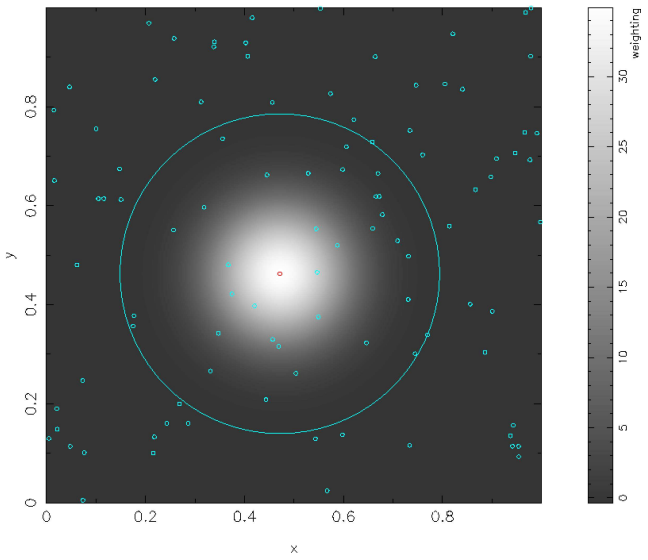

Figure 2.1: The 2D kernel weighting map around a central particle in red for a random 2D distribution of SPH particles in blue. The large blue circle defines the limit of the smoothing length h.

length variation. (These equations are based on or taken from the formulation in Gadget-2, also attributable to Springel & Hernquist, 2002). This equation, apart from the viscosity term, follows from the SPH discretisation of the $-\frac{\nabla P}{\rho}$ RHS term in equation 2.13, where

$$(\nabla P)_i = \sum_{n}^{N_{\rm ngb}-1} \frac{m_j}{\rho_j} P_j \nabla W(r_{ij}, h_j) \tag{2.26}$$

in the most simplistic case, but is now usually symmetrised via a more complex solution to include both particle pressure terms, as seen in equation 2.25 (see Rosswog 2009).

Entropy is generated by using a parameterisation of 'artificial viscosity' - automatically generating entropy during conditions where particles approach each other quickly. For example, in the code we use, the prescription for the viscosity between a pair of particles is:

$$\Pi_{ij} = -\frac{\alpha_{\rm visc}}{2} \frac{(c_i + c_j - 3u_{ij})u_{ij}}{\rho_{ij}} \tag{2.27}$$

where $\alpha_{\rm visc}$ is a constant of around $0.5 - 1$, c_i and c_j are the sound speeds at particles i and j, and u_{ij} is the relative approach speed of the two particles, or zero if they diverge. ρ_{ij} is the arithmetic mean of the two particles' densities. The rate of change of entropy due to this viscosity is

$$\frac{\mathrm{d}A_i}{\mathrm{d}t} = \frac{\gamma - 1}{2\rho^{\gamma-1}} \sum_{j=0}^{N_{ngb}-1} m_n \Pi_{ij} \mathbf{v}_{ij} \cdot \nabla_i (\frac{W_{ij}(h_i) + W_{ij}(h_j)}{2}) \qquad (2.28)$$

which, taking entropy as the particle property to be tracked, is the only equation necessary to define the rate of change of a particle's entropy or internal energy. Equations 2.27 and 2.28 are taken from, and discussed further in Springel (2005).

2.3 Gadget-2 and Implementation

2.3.1 Introduction

Gadget-2 is a massively parallel Tree-PM SPH code (Springel et al 2005), developed as a successor to the popular original GADGET, primarily as a cosmological hydrodynamics simulation tool. It has found uses in a wide range of other astrophysical fields as well, owing to the highly optimised and parellised code and the range of different environments that can be simulated. These range from n-body dark matter cosmological simulations such as the Millennium Simulation (Springel et al. 2005b) to idealised 2D pure SPH simulations. There is a relatively large community of Gadget users, and good user support through a mailing list. The documentation and code are also quite user-friendly - in particular the code is appropriately modular, with many distinct single-purpose routines that are easily understood and modified.

A strength of using a hybrid N-body SPH code as opposed to a purely hydrodynamical code is the ease with which additional mass or modes of operation can be incorporated. In the repetition of the SN 1987A calculations, SPH particles could be briefly converted to dark matter particles for ballistic extrapolation. In another example, emplacing a gravitational potential source (the central star) in the centre of an otherwise hydrodynamically-dominated simulation can easily be accomplished by adding a few hundred massive collisionless dark matter particles with negligible

velocity vectors in the core. Accomplishing this with SPH particles would require very many particles (to represent the large mass of the star) with finely tuned energies (to prevent explosion/implosion or particle ejection) or fewer, but very massive particles, potentially causing problems with unequal-mass particles. In either case it is possible that these central SPH particles would thermally or kinematically pollute the surrounding regions. Achieving this with non-hydrodynamical dark matter particles is cleaner and more elegant in this situation.

Gadget-2 does not need to run on a power of 2 number of processors, unlike some older SPH codes, as its domain decomposition is not based on bisection or oct-tree splitting of the particles between processors. This allows a lot more flexibility in day to day running of the code with limited numbers of processors, and in particular on newer 12-core machines that were available for the work undertaken in this thesis.

An important advantage of Gadget-2 is the asymmetric nature of the equation 2.25. This improves the handling of shocks originating from a low number of high internal energy particles, which is particularly important for the models in Chapter 5.

2.3.2 Rescaling units for Gadget

Gadget-2, in line with many other codes, demands that problems on an astrophysical scale be rescaled before they can be run. A usual method of doing this is to set the relevant timescale of the problem to unity - as an example we set the freefall time of a massive, extended sphere of gas to 1. We set the mass units, length units, and velocity units to 1 in cgs, hence setting the time (length/velocity units) in seconds, and our remaining parameters G and the initial velocities as follows:

$$t_{\mathrm{freefall}} = 2^{\frac{1}{2}} \sqrt{\frac{R_{\mathrm{sphere}}^3}{GM_{\mathrm{sphere}}}} = 1\mathrm{s} \tag{2.29}$$

$$G_{\mathrm{new}} = G_{\mathrm{old(cgs)}} \frac{R_{\mathrm{sphere}}}{\mathrm{cm}}^3 \frac{M_{\mathrm{sphere}}}{\mathrm{g}}^{-1} \frac{t_{\mathrm{freefall}}}{\mathrm{s}}^{-2} \tag{2.30}$$

$$v_{i_{\mathrm{new}}} = v_{i_{\mathrm{old}}} \frac{R_{\mathrm{sphere}}}{\mathrm{cm}} \frac{t_{\mathrm{freefall}}}{\mathrm{s}}^{-1}. \tag{2.31}$$

2.4 Initial conditions creation

2.4.1 Introduction

Gadget-2 requires, at a basic level, (with the exception of randomly seeded gravitational glass making - see section 2.4.2) the input of a set of positions, velocities, and internal energies for the SPH particles used in the simulation. Where the masses are different for a given particle type, this should also be included. The densities of the particles are calculated from their positions and masses in the standard weighted neighbour-number kernel way for Gadget-2. The problem of creating the initial conditions reduces to creating the positions of the SPH particles (optionally varying masses) in such a way that the desired density mapping is achieved, and then assigning the correct internal energy to each particle based on their distribution.

2.4.2 Particle distribution

Sampling the required density field can be approached by Monte Carlo particle seeding in regions with a certain mass (for example, for a spherically symmetric problem, in radial shells) coupled with a form of rejection algorithm to reduce particles being placed too close to one another. However, this will inevitably result in quite a noisy initial distribution. Another approach is to create a uniform density field of particles and then either shrink it into binned regions or apply a transformation to obtain the needed distribution (see Appendix 9.1). This can be considerably less noisy.

The easiest homogeneous distributions to use are regular grids or crystalline structures - cartesian and hexagonal are usually favoured. However, as these are not isotropic they can occasionally create morphological artefacts. As this thesis is primarily concerned with morphology, randomly seeded, approximately isotropic gravitational glasses were used as the basis distribution. These are created as a special option in Gadget-2; collisionless (non-hydro) particles with random positions are placed in a periodic box, gravitational force reversed to repel each other and then evolved for ≈ 1000 timesteps. This creates a distribution where particles are nearly equidistant from their nearest neighbour, without imposing any repeating motif. These positions are then used as input to create the density field needed.

For a spherically symmetric density distribution, the particles can be redistributed from the glass positions by iterating out in radius from a point within the glass distribution (in effect a sort by radius). Densities of a power law form in radius can be dealt with using a geometric transform described in Appendix 9.1. Otherwise, using equal mass particles, the desired distribution mass $M_{\rm d}(r_{{\rm d}_i})$ in the shell $(r_{{\rm d}_i} \longrightarrow r_{{\rm d}_{i+1}})$ is represented by the set of particles of number $n_{\rm p} \approx \frac{M_{\rm d}(r_{{\rm d}_i})}{m_{\rm p}}$ between the radii in the glass positions of $r_{{\rm g}_i}$ and $r_{{\rm g}_{i+1}}$ where $M_{\rm g}(< r_{{\rm g}_i}) = M_{\rm d}(< r_{{\rm d}_i})$. These particle positions can be remapped in a linear fashion by setting their radii as follows:

$$r_{{\rm p}_i} \longrightarrow \frac{r_{{\rm d}_{i+1}} - r_{{\rm d}_i}}{r_{{\rm g}_{i+1}} - r_{{\rm g}_i}}(r_{{\rm p}_i} - r_{{\rm g}_i}) + r_{{\rm d}_i}. \tag{2.32}$$

The particles are then assigned an internal energy based on their radius.

2.4.3 Relaxation and Repressuring

The initial conditions are produced with a certain amount of noise noise due to particle clumpiness and any effects due to the SPH treatment of the gas. They are run under damping conditions to evolve into equilibrium, as in Morris (DPhil Thesis). Velocity and acceleration are damped by a factor of $\frac{1.0}{1.0+\Lambda}$ where $\Lambda < 1$, and $\Lambda << 1$ for conditions with little noise.

This evolves towards a sharply defined density distribution for resolved areas, but produces a badly defined internal energy / radius relation. The internal energies are binned by radius and then a continuous monotonic internal energy-radius profile is reimposed on the particles. The conditions are then fed back into the damping simulation, and the results are re-binned as before. This is normally sufficient to produce a well-defined density-radius and pressure-radius profile.

2.4.4 Standard parameters

Table 2.4.4 shows some of the standard parameters used in the following simulations. Where the parameters differ, they are noted in the text.

A value for γ of $\frac{5}{3}$ is the standard index for a monatomic gas, and the Courant factor is also a Gadget standard parameter, corresponding to 0.3 for other codes

Parameter	Value	Definition
γ	5/3	adiabatic index
Courant factor	0.15	Courant parameter (/2)
Artificial visc	0.8	Gadget2 α in equation 2.27
N_{ngb}	50	SPH neighbour number

Table 2.1: Standard SPH parameters used in this thesis.

using the standard non-Gadget definition of a smoothing length. The artificial viscosity parameter is also a standard within Gadget-2 as distributed, within the range 0.5-1, although the user guide now recommends 1.0. The SPH neighbour number of 50 was chosen as a middle ground number between the trade-off range of resolution vs performance (33-75 as a rough lower/upper bound), although the trend in the last few years has been towards slightly higher numbers.

2.4.5 Plotting

Some plots presented here were generated using the SPLASH plotting package created by Dan Price (Price 2007). This has the capability of generating cross sections by projecting particle properties based on their smoothing lengths onto the cross sectional plane. In the cross-sectional plots that utilise this, no cross section width is given for this reason.

2.5 Test cases

In order to assess the reliability of the code we use, we work through several test cases and compare the results to the literature.

2.5.1 Sod shock tube

The Sod shock tube problem (Sod 1978) is an example of a Riemann problem, widely used as a test for hydrodynamical codes (Hernquist & Katz 1989, Monaghan & Gingold 1982, Springel 2005). A hot, dense region of gas is initially directly bordered by a colder, less dense region, with gravity taken to be null. A shock, and

a rarefaction wave develop, as well as the pre-existing contact discontinuity, and the resolution of these is an important benchmark for the code. Here we take the denser region to be on the left, and the less dense region to be on the right.

Parameter	Value
P_{left}	1.0
ρ_{left}	1.0
P_{right}	0.1
ρ_{right}	0.125
γ	1.4

Table 2.2: Table of values used for the Sod shock tube simulation.

The semi-analytical solution for the time evolution is obtained from the Euler equations, using the Rankine-Hugeniot conditions. The shock propagates through the under-dense region at the speed of sound:

$$c_{\text{sndright}} = \sqrt{\gamma}\frac{P_{\text{right}}}{\rho_{\text{right}}} \tag{2.33}$$

and a rarefaction wave develops in the denser region, progressing at the local speed of sound. After a short period of time, the system consists of 5 distinct regions:

1. The undisturbed region of dense gas.
2. The region bounded by the head and tail of the rarefaction wave.
3. The region between the tail of the wave and the contact discontinuity.
4. The region between the contact discontinuity and the shock wave.
5. The undisturbed region of under-dense gas that the shock wave has yet to reach .

The pressure, density, size and position of these regions can be obtained from the Rankine-Hugeniot conservation laws

$$\rho_1 v_1 = \rho_2 v_2 \tag{2.34}$$

$$p_1 + \rho_1 v_1^2 = p_2 + \rho_2 v_2^2 \tag{2.35}$$

$$\frac{p_1}{\rho_1} + \frac{1}{2} v_1^2 = \frac{p_2}{\rho_2} + \frac{1}{2} v_2^2 + \Delta u \tag{2.36}$$

(where the subscript 1 denotes the region upstream of the shock and 2 the region downstream, and Δu represents the difference in the internal energy per unit mass between the two regions) , and the use of the generalised Riemann invariants across the rarefaction wave:

$$\Gamma = v + \frac{2c(\rho)}{\gamma - 1} = \text{constant} \tag{2.37}$$

A fuller account can be found in the appendix to Pfrommer et al. (2006).

We set up the system with 1179648 particles, using two glass-like distributions a factor of 8 different in particle density and a factor $\rho_2 P_1 / \rho_1 P_2$ different in internal energy to reproduce the initial conditions. A small amount of artificial conductivity was added in Figure 2.4 as per Price (2008), using a fixed multiplier constant of α^u_{cond} of 0.25. This improves the internal energy behaviour over the discontinuity. The results can be seen in Figures 2.2 to 2.4, and show a good agreement with the analytical result.

2.5.2 Wind code

Modelling nebulae of the Eta Carinae / 1987A type requires simulating the effects of stellar wind on gas structure. This was implemented in a serial Gadget-1 version by Thomas Morris (Morris & Podsiadlowski 2007, Morris DPhil thesis).

We updated the code to Gadget-2 and parallelised the wind code for use on the Oxford Astrophysics Beowulf cluster. The advantages of Gadget-2 over its predecessor include improvements in raw speed and efficiency, the ability to run with

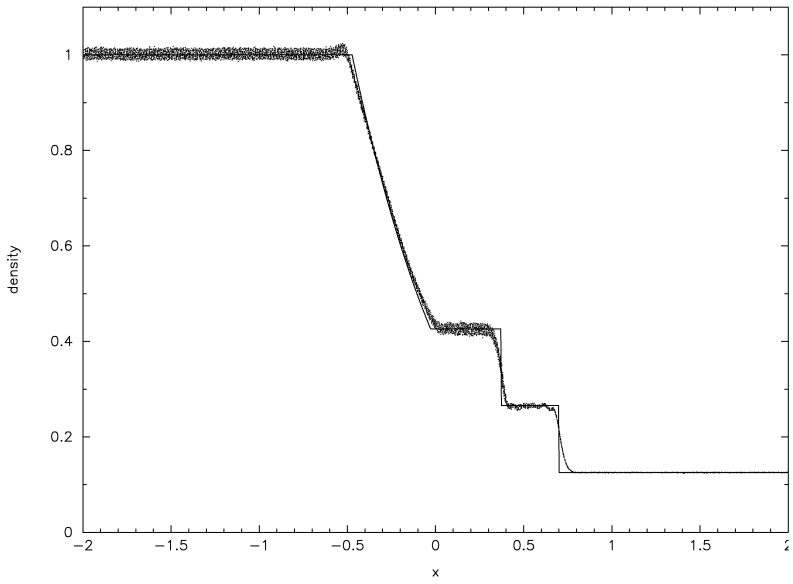

Figure 2.2: Density profile of the gas in the shock tube at time $t = 0.8$. The rarefaction wave, contact discontinuity and shock locations can be seen.

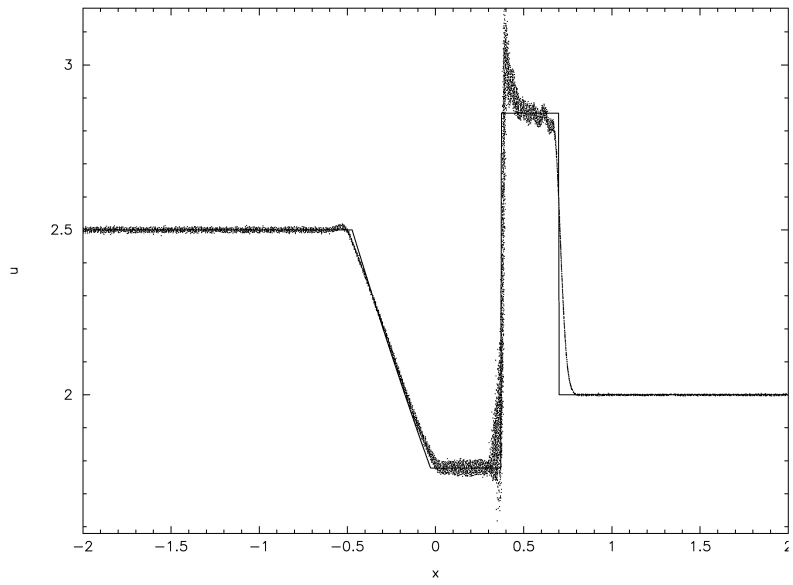

Figure 2.3: Specific internal energies of the gas in the shock tube at time $t = 0.8$.

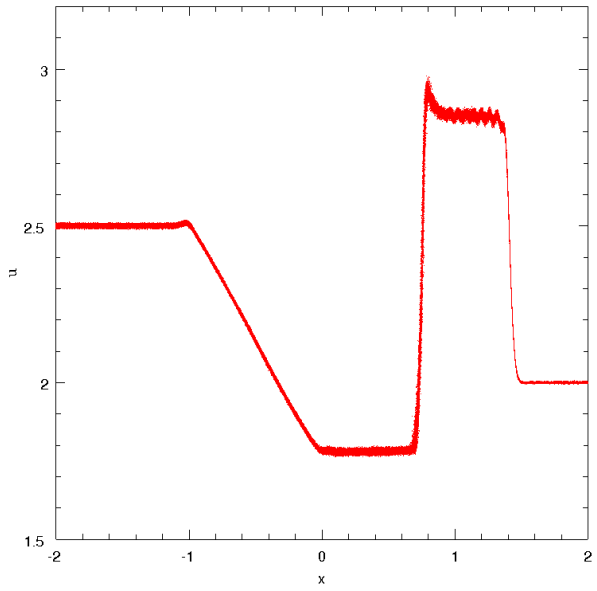

Figure 2.4: As Figure 2.3 but including some artificial conductivity to improve the code over discontinuities.

any number of processors (rather than power-of-two), and running SPH simulations in arbitrary aspected and sized periodic boxes. Parallelisation and the use of the code on the astrophysics Beowulf cluster has greatly reduced wall-clock simulation length.

2.5.3 Adiabatic collapse

An isothermal sphere of gas initially at rest and with a density profile $\rho\alpha\frac{1}{r}$ collapses adiabatically under gravity, rebounds with a shock, and eventually becomes virialised. This is again a classic test for hydrodynamical codes, first proposed by Evrard (1988) and performed in various forms many times since (eg Hernquist & Katz 1989, Theuns 1992, Navarro & White 1993).

Following Evrard (1988) and Springel et al. (2005), the units are set to $G = M = R = 1$, resulting in a freefall time of unity. The specific internal energy of the gas is set to $u = 0.05\frac{GM}{R}$, setting relatively low pressure support for the sphere compared to the gravitational force. The SPH particles are placed according

to a glass-like distribution, with coordinates warped to create the necessary density distribution. Note that it is also possible to use a normal grid, with varying mass particles - however in situations with strong mixing of particles , high dynamic range in mass can cause errors. Additionally, regular grids can impose strong artefacts and departures from symmetry, even with larger numbers of particles; we use the irregular glass making available in Gadget-2 to evolve an asymmetric, evenly spaced distribution of particles.

A shock develops at time $t = 1.1t_{\rm freefall}$, and propagates outwards. The radial velocity and specific internal energy profiles at this time can be seen in Figures (2.5 & 2.6). The results compare favourably to those in Springel (2005). Purely analytic solutions are difficult for this problem.

2.5.4 Isothermal sphere

In this test case, a rotating sphere of gas with radius $R = 5 \times 10^{16}{\rm cm}$, mass $M = 1{\rm M}_{\odot}$, and temperature $T = 100{\rm K}$ collapses isothermally (Boss & Bodenheimer 1979, Burkert & Bodenheimer 1993). As a result of a small density perturbation around the equator the gas forms a bar structure and fragments. This test problem is particularly relevant in star formation studies. It is useful when measuring mass and structure resolution in hydrodynamical codes. To that end, we study the effects of parameter variation on the results.

We rescale the units in order to bring the timesteps within the allowed range of Gadget - we set the sphere to have unit radius and mass (cgs internal code units), and define the unit time as one freefall time. We then scale the value of G and the velocity units according to these definitions. See section (2.3.2) for brief notes.

A complete survey of Gadget-2 parameters can be found in the appendix, and demonstrate the convergence of the code. The minimum resolved mass in an SPH code is $M = N_{\rm ngb} m_{\rm particle}$ (eg Whitworth 1998), and this must be below the Jeans mass in order to resolve fragmentation. We find that this should occur at roughly the 12k particle level.

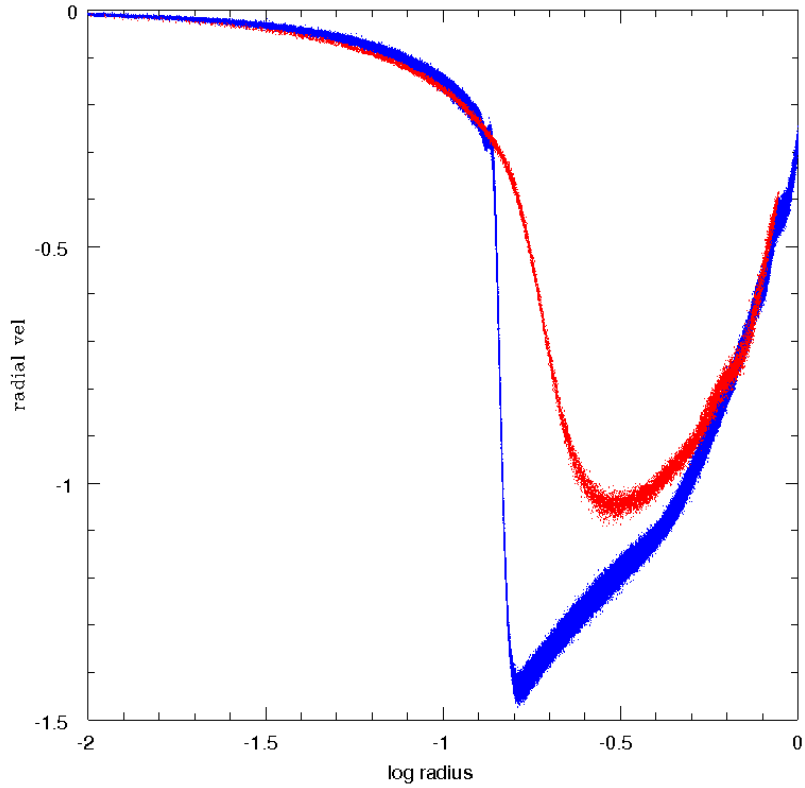

Figure 2.5: Radial velocity profile of the gas after rebound. Blue particles are from a $\approx$ 1 million particle simulation, red from $\approx$ 16k particle simulation. The Gadget-2 artificial viscosity was increased to α_{visc} = 1.6.

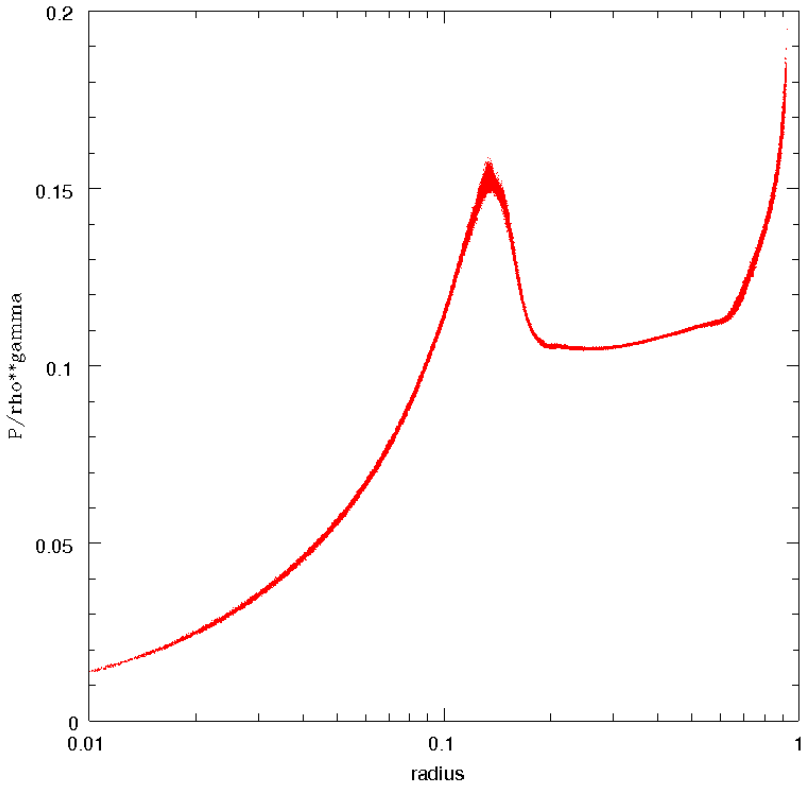

Figure 2.6: Entropy radial profile of the gas after rebound. The simulation used $N_{\rm ngb} = 200$ and 137000 particles.

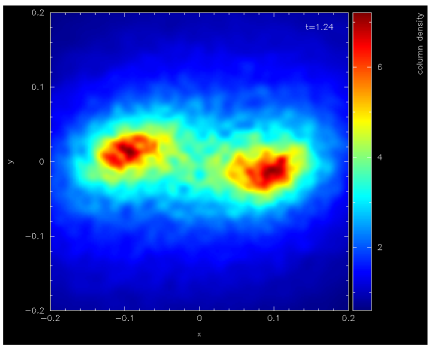

Figure 2.7: Isothermal collapse after 1.24 freefall times. Artificial viscosity = 0.8, particles = 17k, grav softening = 0.004.

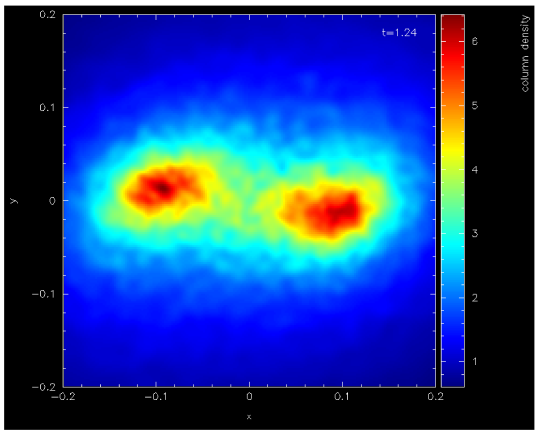

Figure 2.8: Isothermal collapse after 1.24 freefall times. Artificial viscosity = 1.0, particles = 17k, grav softening = 0.004.

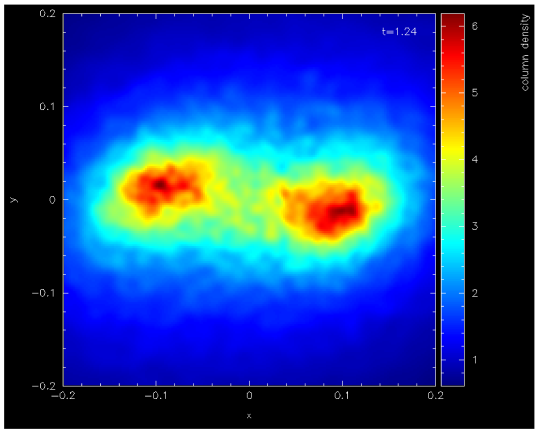

Figure 2.9: Isothermal collapse after 1.24 freefall times. Artificial viscosity = 1.0, particles = 17k, grav softening = 0.0001.

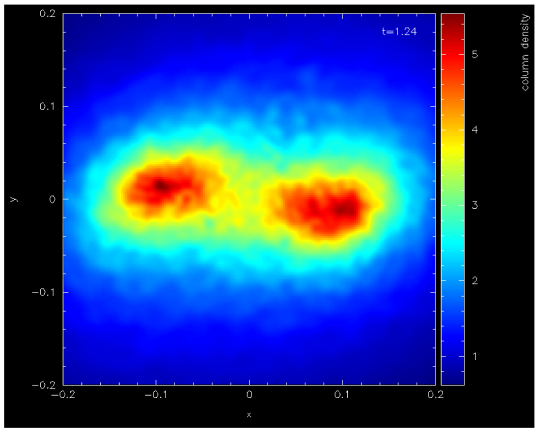

Figure 2.10: Isothermal collapse after 1.24 freefall times. Artificial viscosity = 1.2, particles = 17k, grav softening = 0.001.

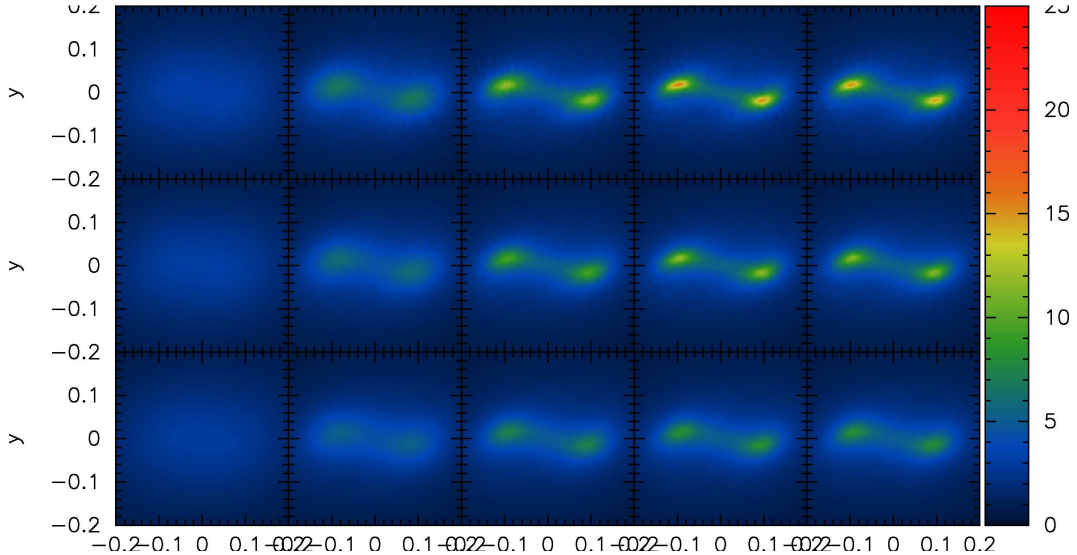

Figure 2.11: A parameter study of isothermal collapse after 1.24 freefall times. The number of particles is 137000. Viscosity varies along the y axis: top to bottom (0.8,1.6,2.4) and the x axis is softening = 0.1, 0.01, 0.001, 0.0001 and adaptive (proportional to smoothing length). Note how large values of softening relative to the structure, and higher viscosity, suppress the higher density regions.

Chapter 3

SN 1987A

3.1 Introduction

The light from the supernova SN 1987A reached Earth on February 23, 1987. It was hailed as the closest observed supernova in 400 years, originating in the Large Magellanic Cloud (LMC) at a distance of 51 kpc (Panagia 1999). As a type II supernova (Gregg, Kimble, and Davidsen 1987) it was one of only a few with measured time-discrete spectra (Menzies et al. 1987) and helped confirm theoretical models of core-collapse with the measurement of its neutrino flux (Hirata et al. 1987, Bionta et al. 1987).

It became apparent that 87A was somewhat unusual - originating from the star $\mathrm{Sk}-69202$ (Sonneborn et al. 1987, White and Malin 1987), a blue rather than red supergiant as had been expected (Woosley 1987). It was a relatively subluminous Type II supernova, at an absolute magnitude of -15.5, with a slower core ejecta expansion velocity (Phillips et al. 1988) that exploded with an intact hydrogen envelope (Woosley, Pinto and Weaver 1988).

Over time the UV flash ionisation and light echoes revealed the circumstellar nebula around SN 1987A, first revealing an equatorial ring, two outer polar rings and several larger, unusual structures. These structures encode the mass-loss and chemical history of the progenitor star; modelling them successfully can help define the nature of one of the most important and best-studied supernovae.

3.2 Background

Type II supernovae such as SN 1987A are a hydrogen-rich subset of core-collapse supernovae. Core-collapse is a phenomenon belonging to relatively massive stars that reach the central pressures and densities to fuse successively heavier elements down to the limit of silicon 'burning' (fusion).

At this point, the star is extremely centrally condensed, and is about to reach the limit of the fusable resources left in the core. However the star normally still retains an extended hydrogen envelope, somewhat masking the internal events in the core, and is classically observable as a red supergiant. No more energy can be extracted via fusion after the silicon is fused, and the burning must progress extremely fast to support the core against the self gravity of the star.

Once silicon burning has been completed, the pressure support against gravity drops, and the core collapses. The internal contents of the star can collapse to create a black hole, or can create a proto-neutron star object, in which case the infall can rebound and cause a core-collapse supernova (for more details and references, see section 4.2). The neutrinos emitted during this conversion were one of the most important diagnostic tests of this picture, and the measurement of 87A's neutrino flux on Earth helped cement the standing of this theory.

3.3 Inner Nebula

The nebula consists of the three major rings lying with their plane at approximately 45 degrees from the line of sight. The two outer rings were observed some time after the event (as a result of light travel time) and were initially hypothesised to be merely light echoes (Crotts, Kunkel and McCarthy 89) until a later study found their apparent motion was undetectable, proving they were relatively discrete and illuminated by the flash ionisation from the SN (Plait et al. 1995, Burrows et al. 1994).

The outer rings contain less CNO processed material (resulting from the Carbon-Nitrogen-Oxygen cycle which dominates in massive stars) than the equatorial ring, pointing to an earlier origin at about 10^4 years prior (Panagia et al. 1996). This is disputed however by Maran et al. (2000). The radial velocity of the equatorial ring

and the known spatial extent suggests an origin of 2×10^4 years ago.

3.4 Outer Nebula and Light Echoes

Light echoes as a method of mapping circumstellar or interstellar material were first studied by Couderc (1939) in the case of dust-scattered light from Nova (GK) Persei. Light echoes of this form, over time, trace the 3D distribution of material around the light source in a non-intuitive (but recoverable) form (for a recent review, see Rest et al. 2011).

Figure 3.1 shows the cross-sectional distribution of light echo parabolas over time from the focus point marked with an X, superimposed on a cross-section through a spherical shell centred on the focus.The intersections between the parabola (in reality, 3D paraboloids of revolution) and the shell map the points which will be illuminated as viewed at extreme angular distance from the right, over time.

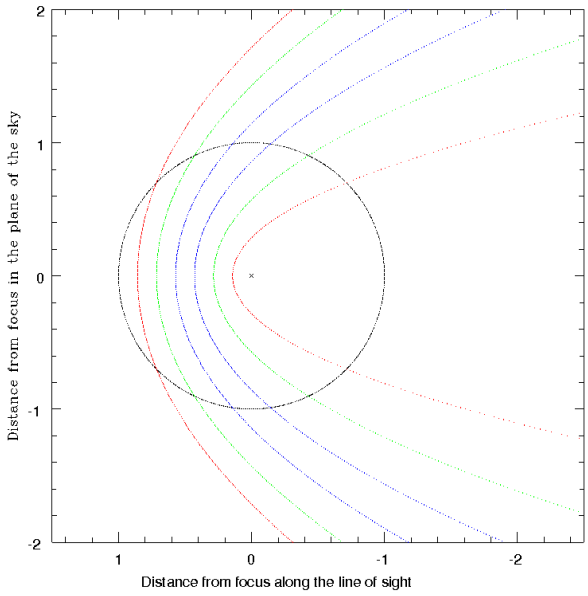

Figure 3.1: A cross section through equally spaced in time light echo paraboloids emanating from the central cross, intersecting a spherical shell of material. Units are arbitrary, with the provision that the angular extent in the plane of the sky is small.

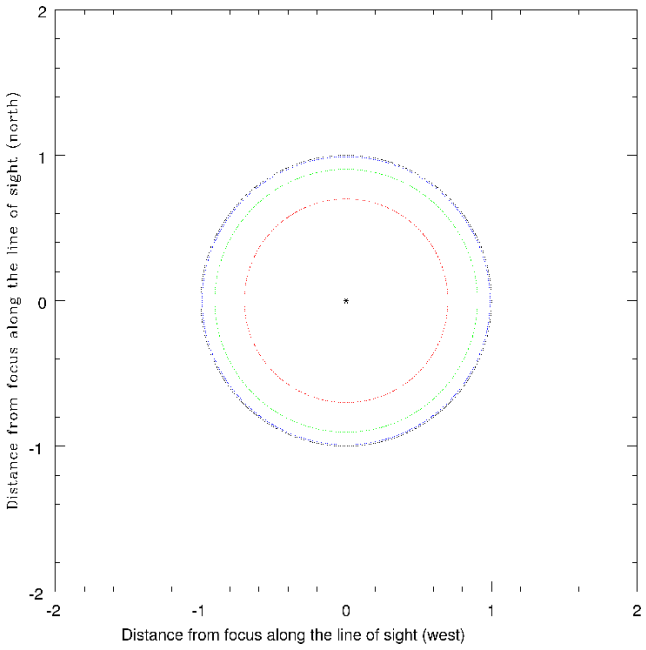

Figure 3.2: As Figure 3.1 but from the observers perspective of the spherical shell material illuminated by the paraboloids. Early light echoes widen extremely rapidly (central point to red), but linger at the maximum radial extent of the sphere (green, blue) before rapidly shrinking on the far face of the shell (red to point) in time symmetry.

The zero-time echo will be on a straight, horizontal line extending right from the focus, and thereafter a series of circles on the spherical shell, shown in Figure 3.2. However, although the paraboloids marked are spaced equally in time (seen by their minimum distance spacing from the focus) the angular extent of the echoes from the spherical shell is certainly not. The echoes will grow very rapidly from a point at the focus, then spend a long time near the maximum angular extent of the sphere, and then shrink rapidly again. The equation for the angular extent of the echoes from a spherical shell is

$$\theta = \sqrt{2ctr - c^2t^2} \tag{3.1}$$

where c is the speed of light, t the (positive) time after the first light has reached the observer, and r the radius of the shell.

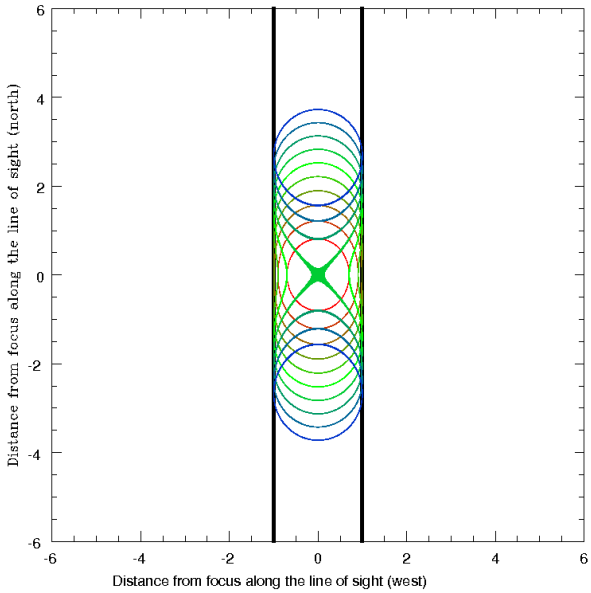

Figure 3.3: A cylindrical shell of material illuminated by light echoes from a source on the cylindrical axis, equally spaced in time. As with previous figures, red through to blue follows early through to late. The light echoes follow an unusual pattern as the path length becomes longer than twice the cylindrical radius (the X shaped green echo progressing to the blue separate lobes).

A sheet placed in front of the shell perpendicular to the line of sight, at a distance x would still display some non-linearity at early times; the equation is $\theta = \sqrt{2ctx + c^2t^2}$.

Light echoes from a cylinder placed with its axis in the plane of the sky will have characteristics of a sheet in the axial direction and characteristics of a spherical shell in the plane of the cylindrical radius.

These are shown in Figure 3.3. An important note is that every point on the cylinder is mapped at a unique time, and the geometry is recoverable from the time distribution of light echoes provided that the origin time is known.

Angle dependent scattering by dust can also be used to help trace the structure, although it is strongly dust grain size dependent. Grains in the Rayleigh limit for UV-visible light (less than a few nm) will isotropically scatter light - this behaviour has an extreme wavelength dependence $\frac{I_o}{I} \propto \lambda^4$ where I is the intensity received at a given angle after scattering from a particle, I_o the original incoming intensity, and λ the wavelength). Larger grains up to micron level have less wavelength dependent scattering and an extremely strong bias against back scattering, of around 2 orders of magnitude in efficiency; the difference between small and large grains can be calculated by density, obscuration and colour measurements in the case of 1987A (Sugerman et al. 2005).

We have considered spherical shells, and sheets and cylinders in the plane of the sky, but it is also useful to supplement intuition by considering a tilted shape - in the case of SN 1987A, a tilted cylinder is particularly relevant.

The light echoes from a cylinder at 45° to the line of sight are shown in Figure 3.4, and display a slightly more unusual light echo distribution. Whereas the northern, nearest part of the cylinder is nearly perpendicular to the direction of parabola movement, the southern nearest face is almost parallel to it, and increasingly parallel at later times. This results in a faster apparent motion for the echo in the south, and if angle dependent scattering is a factor, an increasingly brighter southern echo as well.

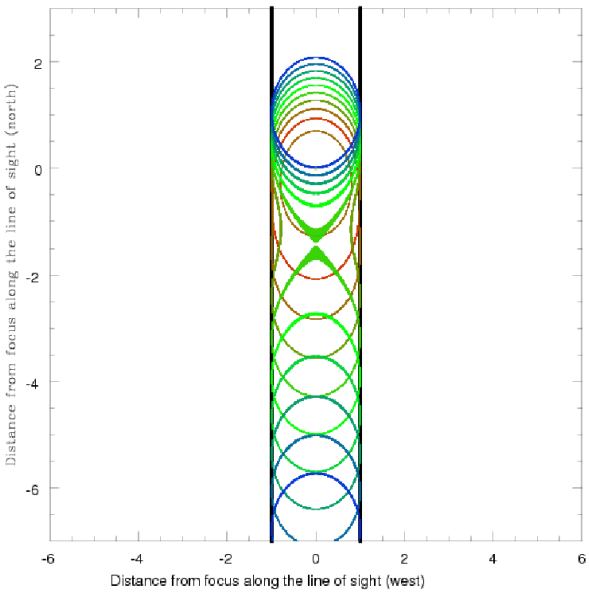

Figure 3.4: A tilted cylindrical shell of material illuminated by light echoes from a source on the cylindrical axis, equally spaced in time.

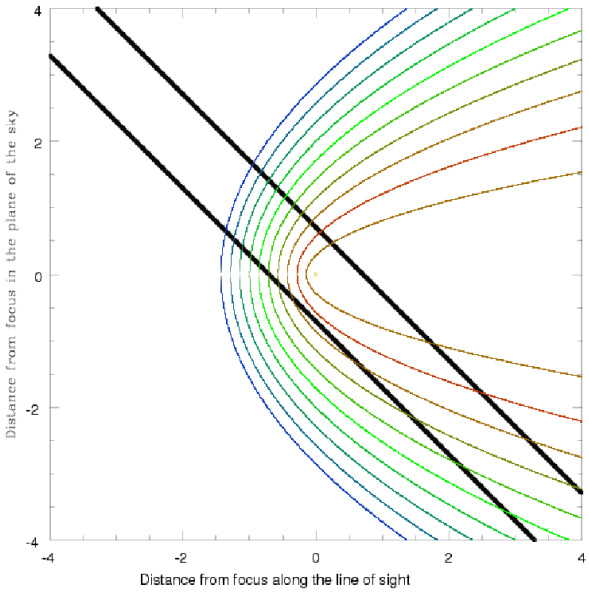

Figure 3.5: A tilted cylindrical shell of material illuminated by light echoes from a source on the cylindrical axis, equally spaced in time. The light echoes follow an unusual pattern as the path length becomes longer than twice the cylindrical radius (the X shaped green echo progressing to the blue separate lobes).

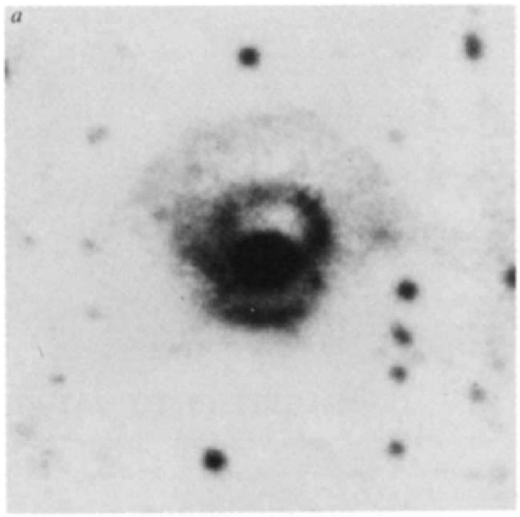

Figure 3.6: Early observations by Wampler et al. (1990), showing the three rings of 1987A and the Napoleon's hat feature to the north.

Density enhancements exterior to the three ionised rings began to be apparent approximately 2 years after the supernova with the detection of a curved bright nebulosity 6" north of the SN extending west and east, named 'Napoleon's Hat' (Wampler et al. 1990). An approximately circular light echo of radius $>$ 8-9", stronger in the east, was discovered by Bond et al. (1989) and was observed to move rapidly outwards in subsequent observations. A summation and full analysis of light echoes is found in Sugerman et al. (2005), from which the main observational tests are drawn for this work.

Figures 3.7 and 3.8 show the positions of the light echoes at various times from approximately 2 years post-supernova to 10.4 years.

Sugerman et al. (2005) under the assumption of reflective (about the equatorial ring plane) and rotational (approximately around the polar axis through the triple rings) analysed light echoes from the more distant parts of the nebula to build a rough picture of the surroundings, reproduced in Figure 3.9. Especially in the outer regions, most of the shape is inferred from assumptions about rotational symmetry - only a small fraction of the shape is returned by the observed light echoes. The outer structure implied has an over-density in the equatorial plane, and two almost closed polar lobes.

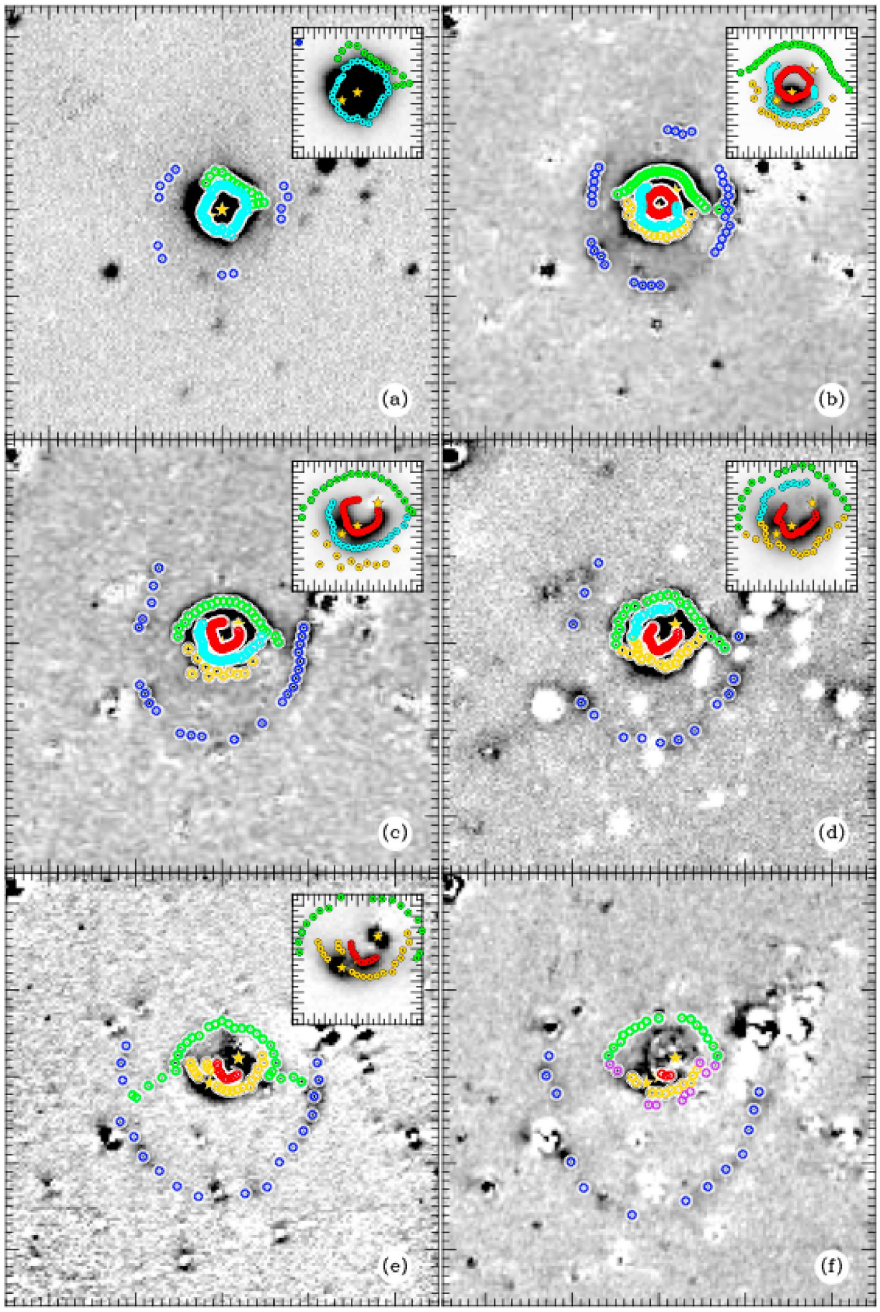

Figure 3.7: Early light echoes from Sugerman et al. (2005), showing 50 arc second by 50 arc second star-PSF subtracted fields centred on the supernova and colour coded by structure 'type' from 1.8 years post-peak SN to 4.8 years. The structures of particular interest to this work are the Napoleon's hat echoes (in green) and the largest, extended structure (in blue).

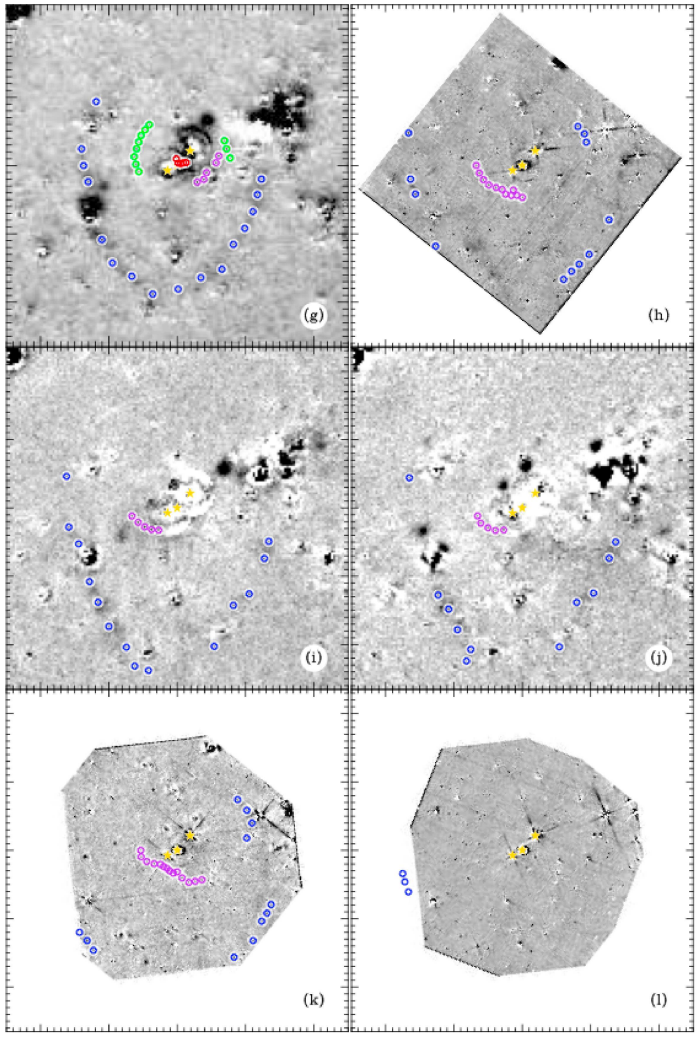

Figure 3.8: Later light echoes from Sugerman et al. (2005), showing 50 arc second by 50 arc second star-PSF subtracted fields centred on the supernova and colour coded by structure 'type' from 5.7 years post-peak SN to 10.4 years. The Napoleon's hat echoes are highlighted in green, a southern inner echo identified as its counterpart in pink, and the larger, extended structure in blue.

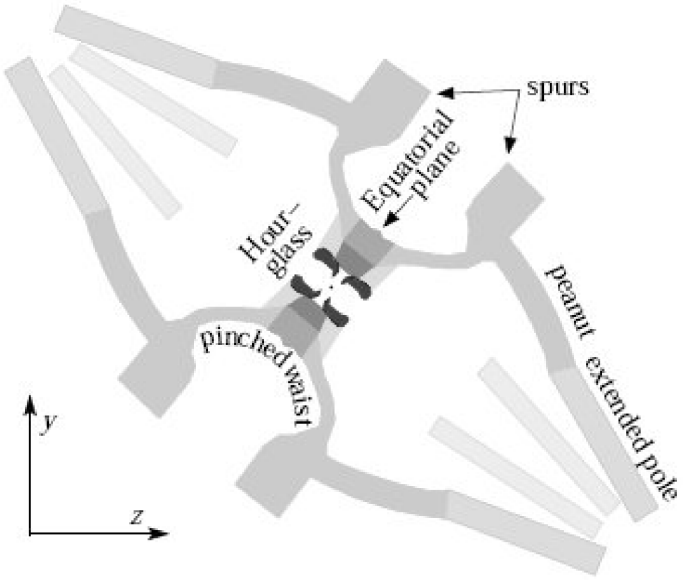

Figure 3.9: Inferred outer nebula structure around SN 1987A from Sugerman et al. (2005). It is clearly bipolar, with two lobes and an equatorial enhancement.

As mentioned earlier, the properties of the dust can be disentangled from the wavelength angle dependence of the light echoes - these suggest a large grain distribution for the largest echoes, which is strongly biased against back-scattering; only the nearest parts of the structure should have light travel path angles close enough to $180°$ to have detectable flux. This, together with time constraints, means that the structure is necessarily incomplete, instead of being mapped out fully in all dimensions in the case of isotropic, small dust grain scattering. Sugerman et al. (2005) suggest that the Napoleon's hat locality contains smaller grains, which is the reason for the illuminated 'Napoleon's collar' despite the acute light path angle.

3.5 Modelling background

The standard model in the early years after 1987A consisted of generalised interacting winds implementations with a single star (e.g. Luo + McCray 1991, Wang and Mazzali 1992, Blondin and Lundqvist 1993) where a fast, low-density wind hits an equatorially enhanced, pre-existing slow high density wind. This leads to a deflection around the equator and an hourglass form for the nebula. This had some success, but ultimately was not compatible with the discoveries that the outer rings were not mere limb brightening (Burrows et al 1994) and possibly originated at a different point in the star's evolution (Panagia 1996).

In addition, single star hypotheses rely on convective overshooting / rotational dredge up /metallicity in order to make the RSG-BSG (red supergiant to blue supergiant) transition, which is perhaps not actually present in the observed LMC Hertzsprung-Russell diagram (Podsiadlowski 1992).

Early binary models of the nebula created the outer rings through a truncated double cone formed by a colliding wind interface between the binary stars - after the stars merged, an excretion disk was ejected forming the inner ring, and the BSG fast wind swept up the outer ring material into limb density enhancements (Podsiadlowki et al 1991, Lloyd et al 1995). Models that suggest a surviving companion are not borne out by observations.

3.6 Binary hypothesis and reproduction of the inner nebula

Binary merger models can produce the dredge-up / rejuvenation relatively easily (Hillebrandt and Meyer 1989; Podsiadlowski et al 1990; Podsiadlowski 1997), the latest of which predict a 15 $M_{\odot}$ and a 5 $M_{\odot}$ binary merger from a common envelope pathway (Podsiadlowski and Ivanova 2003).

These progenitors were then invoked in a model to reproduce in detail the three rings of the SN 1987A inner nebula by Morris and Podsiadlowki (2007). A schematic of the stages in this hypothesis is shown in Figure 3.10.

Originally, the 87A system was hypothesised to be a binary, with the 15 $M_{\odot}$ and 5 $M_{\odot}$ members from the chemical analysis work. The primary (the most massive, 15 $M_{\odot}$ star) began to transfer mass to the secondary (the first stage in the schematic). This process was unstable, and the mass transfer accelerated to the point that the secondary became engulfed in the same hydrogen envelope as the primary (the common envelope phase, second stage in the schematic). Over a course of hundreds of years, the cores of the primary and secondary tightened their orbit and spiralled in towards each other, losing angular momentum to the envelope, which became spun up and oblate.

The separation between the cores exponentially decays, and the cores merge - the energy released is sufficient to release a shock and drive some of the envelope off (the third stage in Figure 3.10. This was modelled using SPH, in a parametrised way, with the cores not individually modelled. This produced an asymmetric flow of ejecta from the distorted envelope, for lower energy shocks, which later provided the north and south material for the two outer rings. Shortly afterwards, some of the rapidly spinning outer envelope was shed, which created a torus of expanding material that would become the equatorial ring.

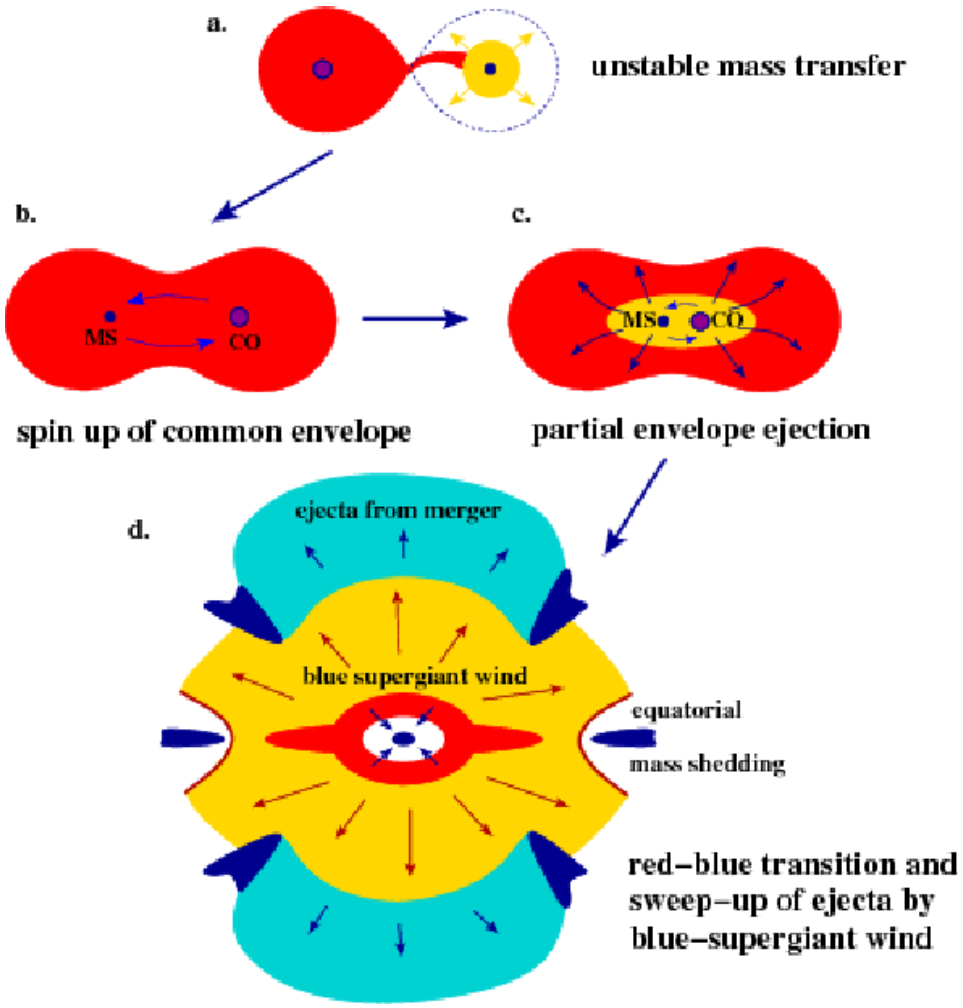

Figure 3.10: Schematic from Morris and Podsiadlowski (2007) showing their binary progenitors origin hypothesis for creating the inner rings. A binary system evolves into a common envelope phase after mass transfer, and mass ejection from the end of the common envelope phase forms the material for the rings. These are shaped by a wind from the merged star. The merged star goes supernova twenty thousand years later as SN 1987A.

After rejuvenation, the now blue supergiant star then begins to evacuate its surroundings with a fast, hot wind. This shapes the north and south polar envelope ejecta into a more hourglass shaped morphology and to a lesser extent, shapes the equatorial outflow ejecta. This phase lasts for approximately 20000 years, in line with the findings above. After this point, Morris and Podsiadlowski simulated the observed emission from the flash-ionisation of this ejecta created by SN 1987A, and found very good agreement with the observations.

The focus of this work is to explore whether the outer nebulae of 1987A can be well explained by this picture. To do this, we start at an earlier point, in the unstable mass transfer phase (first stage in Figure 3.10, and hypothesise that the accretion of this mass onto the secondary could have launched jets into the surroundings. We further hypothesise that there would have been a pre-existing, slow red supergiant wind from the binary members before the merger, out to the parsecs-level needed for the scale of these outer nebula features. We investigate the effects of these jets propagating into this pre-existing wind.

3.7 Method

This work will attempt to model the outer regions of the nebulae, in particular the well-constrained Napoleon's Hat arc feature to the north of the rings (Figure 3.6), and the larger bipolar structures as summarised in Sugerman et al. (2005). This is a missing part of the 1987A picture of Morris and Podsiadlowski (2007, 2009), and provides a further test of the common envelope merger hypothesis for the progenitor of SN 1987A.

We attempt to reproduce the bipolar outer nebula with a bipolar BSG wind expanding into an ambient, slow spherical RSG wind. This is possible in the stage immediately prior to a common envelope phase, when Roche lobe overflow leads to mass accretion onto the companion, driving a brief jet phase before engulfment. Physically realistic reproductions of this phase and their comparison to data would be a valuable test of the binary theory of SN 1987A.

We use hot (10000K, initially) bipolar jets to simulate the effect of possible jets arising from the mass transfer to the companion, with a mass no more than 0.5 $M_{\odot}$ in 500-1000 years. In practice, the leading edge of the jets decelerates, and the jet

becomes shell-like rather than conical when driving it through the whole time period of 20000 years. The time period is relatively unconstrained within the range given. The mass lost in the jets is also not critical, as above a certain point (much lower than $0.5M_{\odot}$) it does not decelerate significantly when driving into the medium that we use and causes much the same morphological effects on it.

We drive a 10000K bipolar jet with total mass 0.5 $M_{\odot}$ into a slow, cold (10K-100K) spherical wind. The temperatures used are roughly based on expected cold/warm dust temperatures for an old wind, and a photospheric temperature for the jets, but are not particularly significant due to the overwhelming kinetic energy of the jets in this frame. The jet phase lasts 10^3 years in the simulations below, corresponding to the rough timescale of unstable mass transfer before the common envelope phase. We choose realistic values for the speed and mass loss rates of both winds - a few hundred kms^{-1} and $10^{-4}M_{\odot}\mathrm{yr}^{-1}$ for the jets, and 20-30 kms^{-1} and around $10^{-5}M_{\odot}\mathrm{yr}^{-1}$ for the ambient RSG wind. The speed of the jets was chosen to give the 8 parsec length scale after the approximate 20000 year lifetime of the merged remnant - hence, around $350\mathrm{kms}^{-1}$. This is also in rough agreement with main sequence surface escape velocities, which are good proxies for final stellar wind speeds. The opening angle of the jets was experimented with - it is worth noting that extremely small opening angles are ruled out by the smoothing effect of the jet-launching star's orbital velocities. The numbers that gave the best general fits to data were opening angles of between 10 and 20 degrees, representing a total angle per jet of 20 to 40 degrees. The speed and mass loss of the wind forming the ambient medium was chosen to be broadly in line with observed mass loss velocities from red supergiants, although mass loss from red supergiants is relatively loosely constrained as a whole. The mass loss rates give of order a solar mass in the red supergiant progenitor wind, which is a reasonable number for the 15 solar mass post-mass loss primary star.

4000 years after the end of the jet phase, we could emplace the ballistically extrapolated ejecta (from the standard A4 model in Morris (DPhil thesis)) from the common envelope into the simulation and switch on the BSG wind exactly as in Morris and Podsiadlowski (2007). This would give a complete picture of the system. However, as the interaction between this ejecta and our outer nebula structure is minimal, we omit it for the sake of computational speed.

The detailed reproduction of the triple rings is not the aim of this work, as it has been amply explored in Morris (DPhil thesis) and subsequent papers (Morris & Podsiadlowski 2007, Morris & Podsiadlowski 2009). However, the material that comprises the ring structures - the common envelope ejecta and the equatorial torus - can be simulated within the context of the outer nebula. Their structure can be seen below in Figure 3.11.

We test the simulated structures in a similar way to the light echo demonstration cases shown earlier. We create a time series of paraboloids, enclosing a width of 100 days (a square wave approximation to the core collapse light curve), as seen from an observer at 45° to the axis of symmetry. Each image is composed of a 100×100 grid in the simulated plane of the sky, and each particle that falls within the paraboloids volume produces a reflection based on its density which is summed into the grid cell value. Each grid cell should have a few particles illuminated, if it has any, as seen from the particle plots above. As any scattering is likely to be angle dependent, and the mass loss not well constrained, these are presented as qualitative geometrical illustrations rather than in a realistically observable form - if this was done, column density along the centre of the pixel bin should be calculated from the particle distribution as in the SPLASH visualisation code.

3.8 Results

3.8.1 Parameter study - raw hydrodynamics

In our example simulations presented here, the outer structure of the interacting winds bears some striking similarities to the sketch in Sugerman et al. (2005).

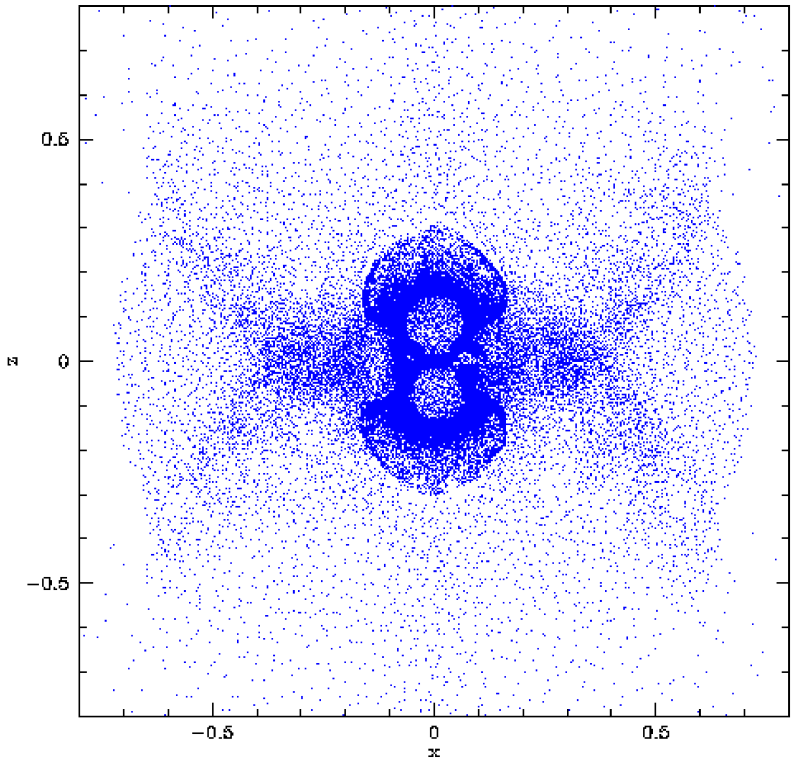

Figure 3.11: A cross section of the full 87A nebula simulation, showing the swept out bipolar structure and equatorial enhancement. Structures analogous to the 'spurs' in the Sugerman results are found at the equatorial edges of the wind shock. Axes are in units of 8 parsecs.

Parameter	Value
Jet velocity	350 km/s
Jet opening angle	20 deg
RSG wind velocity	20 km/s
RSG wind mass loss rate	$2.0 \times 10^{-5} M_{\odot} \mathrm{yr}^{-1}$
Jet initial launch time to SN 1987A delay	22800 years
Jet production lifetime	1000 years
Jet mass loss	0.06 $M_{\odot}$
Total number of particles	900000 (approx)

Table 3.1: Table showing the standard parameters used in the simulation.

Figure 3.11 shows the results of a typical SPH run in a pure particle plot - these can be taken as tracing the density structure of the simulation. While the equatorial enhancement and spurs can be seen, the larger bipolar structure is too wide. The following simulations use the following parameters:

Where a higher progenitor pre-existing wind velocity was used, the progenitor pre-existing mass loss rate was correspondingly increased such that the total mass in the 8 parsec sphere of wind remained constant. The mass loss rate in this wind is compatible with known red supergiant wind mass loss rates (see e.g. Groenewegen et al. 2009 for a study of evolved LMC/SMC (Large Magellanic Cloud and Small Magellanic Cloud) stars). The velocities used for this wind, 20 and $30 \mathrm{kms}^{-1}$, are within the observed ranges of red supergiant winds such as that of VY CMa (as discussed in Decin et al. 2008).

The delay between the start of the jet launching from the unstable mass transfer, to the merger remnant resulting in SN 1987A and the light echoes, is here taken to be 23000 years. This is slightly over the sum of the 20000 years delay between the rings material production (the common envelope ejection phase in Figure 3.10), and the delay between the start of the jet launch phase and the ejection of the common envelope. However, it encompasses a range of jet phase lifetimes that may be longer than our canonical 1000 years, and gives a slightly better fit to the data than 20000 or 21000 year jet expansion times. A higher jet mass loss rate would allow the ejecta to decelerate less, and produce roughly the same results for a slightly lower lifetime.

The jet mass loss parameter was chosen to be a rough minimum that would

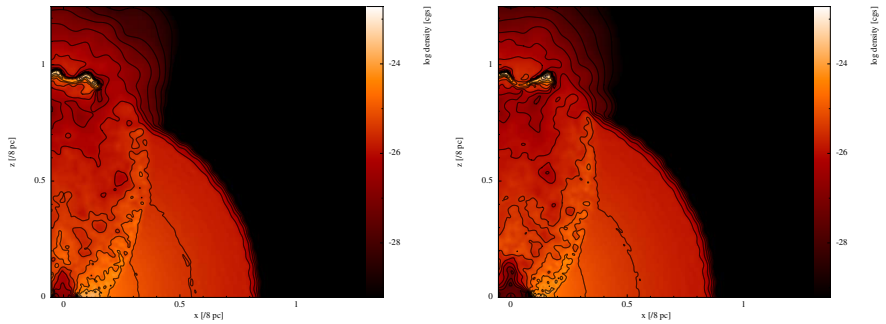

(a) RSG wind = $20\mathrm{kms}^{-1}$ (b) RSG wind = $30\mathrm{kms}^{-1}$

Figure 3.12: Final wind structures at the point of the supernova, without considering the inner CE ejecta, for a jet velocity of $350\mathrm{kms}^{-1}$, an RSG wind of $20\mathrm{kms}^{-1}$ (left figure) and $30\mathrm{kms}^{-1}$ (right figure) and a jet opening angle of $10°$. The smaller opening angle results in a smaller width cavity, which appears to be exacerbated by the higher RSG wind in the right hand figure.

produce a jet that began to fragment and decelerate slightly, in order to produce some axial jet material as in the Sugerman findings. It is well below a physically believable upper bound (compared to the total mass transfer involved in creating a common envelope) of 0.5 solar masses, and represents quite a believably small fraction of the mass transfer from the 15 solar mass star to the 5 solar mass star, as well as a low amount of energy needed to fuel the jet launch mechanism compared to the power released in the mass transfer and any accretion disk. Indeed, the 'jets' here could be realistically said to be a relatively high-mass, bipolar, average velocity massive star wind rather than classic microquasar jets.

Figures 3.8.1 to 3.8.1, show the differing morphologies produced by a variation in jet and RSG wind parameters. We choose 2 values of RSG wind velocity, 20 and 30 kms^{-1}, and three values of jet opening angle (10, 15 and $20°$. We keep the mass in the RSG wind constant, which implies a differing mass loss rate. In fact, we assert that the cavity shapes are not very sensitive to the mass in the RSG wind; simulations with the mass 10 x lower demonstrate much the same cavity shapes, albeit slightly wider (Figures 3.15 and 3.16). To the extent that the BSG wind is not too strongly decelerated, the raw kinematics ensure that variations in the mass in the BSG wind has little effect as well - the fragmentation and instabilities in the BSG jet material is a function of mass and resolution, however.

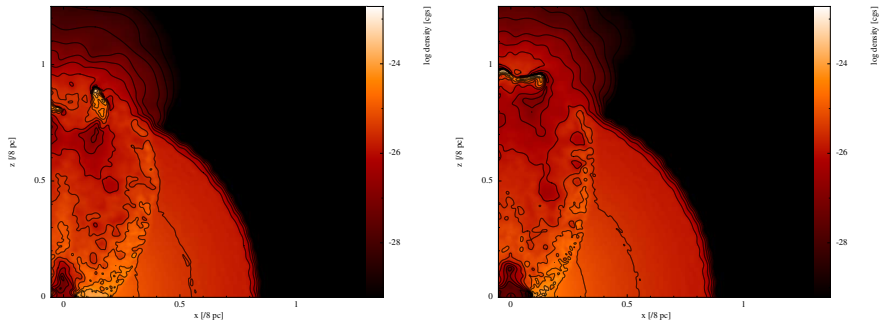

(a) RSG wind = $20\mathrm{kms}^{-1}$ (b) RSG wind = $30\mathrm{kms}^{-1}$

Figure 3.13: Final wind structures at the point of the supernova, without considering the inner CE ejecta, for a jet velocity of $350\mathrm{kms}^{-1}$, an RSG wind of $20\mathrm{kms}^{-1}$ (left figure) and $30\mathrm{kms}^{-1}$ (right figure) and a jet opening angle of $15°$. A slightly wider jet opening angle increases the breadth of the cavity, but does not produce a tapering towards the jet material. As in Figure 3.12(b) the right hand cavity is wider than the smaller opening angle examples (Figures 3.12(a) and 3.12(b)), but is mitigated by the faster wind.

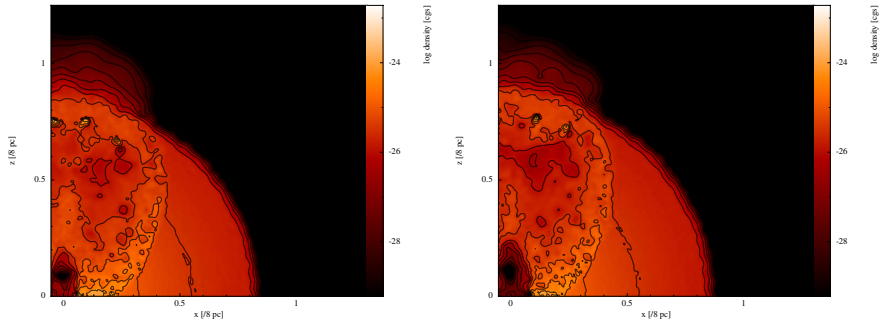

(a) RSG wind = $20\mathrm{kms}^{-1}$ (b) RSG wind = $30\mathrm{kms}^{-1}$

Figure 3.14: Final wind structures at the point of the supernova, without considering the inner CE ejecta, for a jet velocity of $350\mathrm{kms}^{-1}$, an RSG wind of $20\mathrm{kms}^{-1}$ (left figure) and $30\mathrm{kms}^{-1}$ (right figure) and a jet opening angle of $20°$. These figures show the most bulbous cavities of this set of 6 - the left hand figure has a combination of relatively slow RSG wind and relatively large jet opening angle. The right hand figure produces an equally wide cavity, but, in terms of the reproduction of the schema found in Sugerman et al. (2005), is still affected negatively by the speed of the wind.

The figures show a relative trend of increasing cavity 'breadth' with increasing jet opening angle, and a trend of decreasing cavity 'breadth' with increasing RSG wind velocity. They also belong to the same density regime found in Sugerman's study of around 1-3 atoms per cubic centimetre in the light echoes (approximately 1.67e-24 - 5e-24 gcm^{-3}) decreasing to around 0.03 (5e-27 $gmcm^{-3}$) and have a roughly similar mass (of order a solar mass of material, or slightly less).

In our attempt to create the general type of cavity found in the Sugerman et al. 2005 schema (Figure 3.9), it appears wider jet opening angles may create larger equatorial breadth, but at the expense of tapering polar ends. Larger RSG wind velocities, while plausible, would act to slim the cavities further. We should also note that although Figure 3.9 appears clearly defined in shape, the morphology is only very partially observed, with an assumed offset from the light source; these points are elaborated further in the paper. We will therefore also test our jet cavities directly against observations in the form of light echoes, as described above.

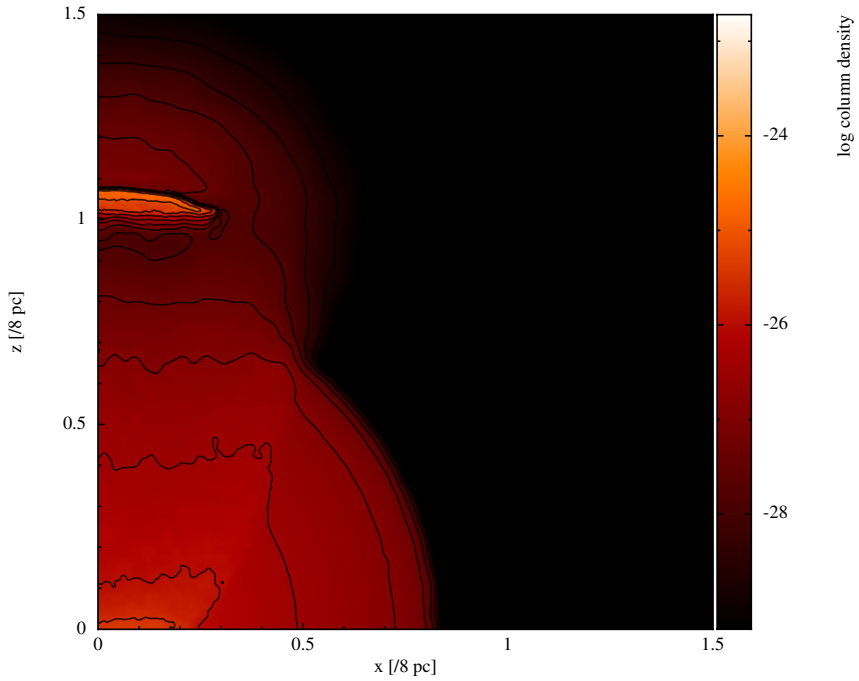

Figure 3.15: Final wind structure as in Figure 3.13(a), with spherical red supergiant (indirect progenitor) wind mass loss a factor of 10 lower. The cavity shape is qualitatively similar to the above simulation results, but wider in breadth.

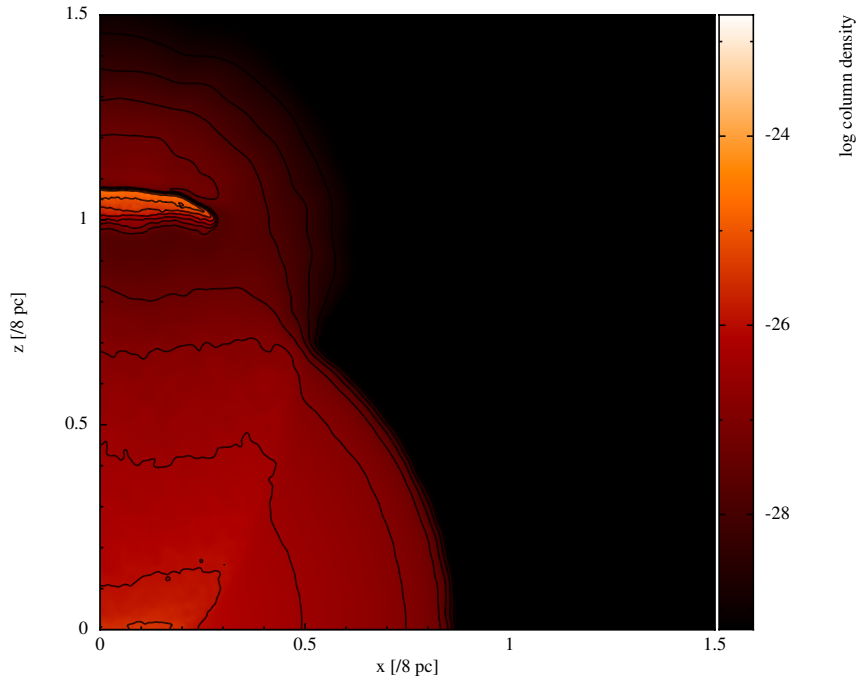

Figure 3.16: Similarly to the above Figure 3.15, the final wind structure with the same parameters as Figure 3.13(b), with spherical red supergiant (indirect progenitor) wind mass loss a factor of 10 lower. Already a wider cavity, the lower mass loss rate increases the breadth.

While a constant velocity, constant mass loss win will always produce a $\rho \propto r^{-2}$ profile, variations in these parameters over time will produce a deviated profile. The cavity shape should be sensitive to the profile because of the differential shock velocities as it propagates through different density material at different radii. Figure 3.17 shows a comparison between a standard parameter run with the normal density profile and one with a $\rho \propto r^{-2.5}$ profile. The newer profile shows a wider base for the cavity, nearer the equatorial plane. It has also disrupted the jet as it has passed through the higher density centre and left both jet residual fragments and some entrained core material close to the axis.

3.8.2 Non-isotropic mass loss

RSG stars such as our indirect progenitor producing the red supergiant wind (when free of binary or planetary interaction) are not expected to be fast rotators due to

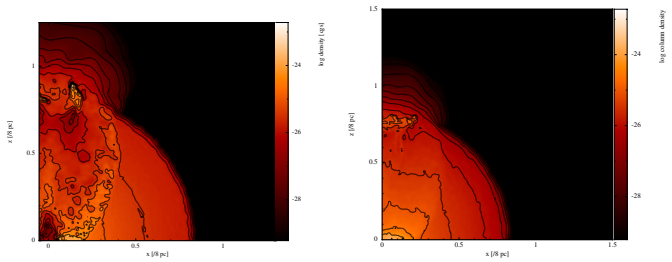

(a) normal wind profile (b) $\rho \propto r^{-2.5}$ profile

Figure 3.17: A comparison of the jet cavities in the normal $\rho \propto r^{-2.5}$ profile (3.17(a)) and a $\rho \propto r^{-2.0}$ profile (3.17(b)). Both models have the same exterior mass, but the $r^{-2.5}$ profile has a more concentrated central density. It has a greater extent near the equatorial plane, and has fragmented the jet appreciably in the early stages.

the conservation of angular momentum when expanding from solar radius to astronomical unit scales. However the progenitor in question could well have been spun up to a degree, especially in the outer envelope, for a substantial period of time in the pre-CE pre-fast mass transfer phase. The rotational effects would then produce a bipolar asymmetry in the mass loss - perhaps not enough to help create a strongly bipolar cavity from a weakly bipolar fast, hot post-merger BSG wind, but potentially enough to alter the shape of the cavities we produce with jets. Given the long axis incompleteness of the light echoes observed, a local inhomogeneity in the surrounding ISM affecting the expansion of the indirect progenitor's red supergiant wind is also quite possible.

We therefore repeat a selection of the above jet simulations with a simplistically distorted red supergiant wind. We distort the red supergiant wind both to have an equatorial plane over-density and under-density.

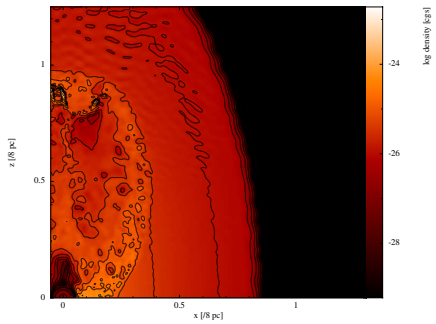

Figure 3.18: Finished jet simulation using a distorted pre-merger RSG progenitor wind (z velocities increased by a factor of 2) for a $20\mathrm{kms}^{-1}$ equatorial plane velocity RSG wind, $350\mathrm{kms}^{-1}$ fast, hot companion jet with a $10\,\mathrm{deg}$ opening angle. The cavity is initially wider, with a much flatter gradient at mid to low z values than in Figure 3.12(a), the control test for this simulation.

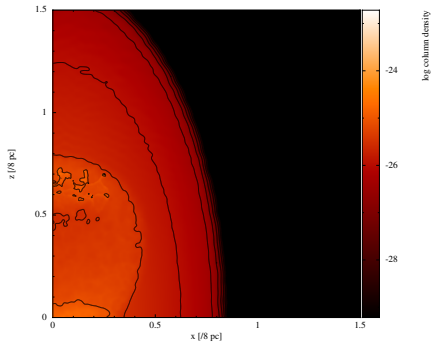

Figure 3.19: Finished jet simulation using a distorted pre-merger RSG progenitor wind (z velocities increased by a factor of 2) for a $20\mathrm{kms}^{-1}$ equatorial plane velocity RSG wind, $350\mathrm{kms}^{-1}$ fast, hot companion jet with a $20\,\mathrm{deg}$ opening angle. The cavity, while more bulbous owing to the opening angle than in Figure 3.18, is far wider at the base than in Figure 3.14(a), the control test for this simulation.

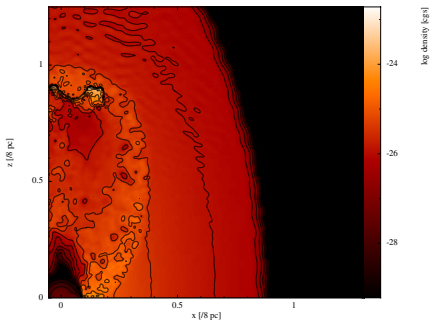

Figure 3.20: Finished jet simulation using a distorted pre-merger RSG progenitor wind (z velocities increased by a factor of 2) for a $30\mathrm{kms}^{-1}$ equatorial plane velocity RSG wind, $350\mathrm{kms}^{-1}$ fast, hot companion jet with a $10\,\mathrm{deg}$ opening angle. The cavity is more tubular and broader initially, with a flatter gradient at mid to low values of z than in the control Figure 3.12(b).

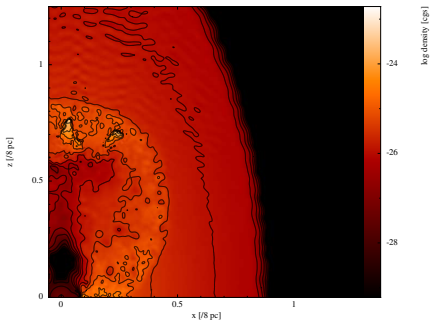

Figure 3.21: Finished jet simulation using a distorted pre-merger RSG progenitor wind (z velocities increased by a factor of 2) for a $30\mathrm{kms}^{-1}$ equatorial plane velocity RSG wind, $350\mathrm{kms}^{-1}$ fast, hot companion jet with a $20\,\mathrm{deg}$ opening angle. The cavity is more tubular than in the standard case in Figure 3.14(b), the control test for this simulation, and it is broader at the base than most standard results above.

The cylindrical axis 'under-density'/over-velocity simulations, seen in Figures 3.18 to 3.21, show a general broadening of the base of the cavity relative to the standard 'control' simulations with undistorted pre-merger, pre-existing RSG winds. Given the significant inner breadth of the cavity calculated by Sugerman et al. (2005), this should allow a greater parameter space within companion jet opening angle and pre-merger RSG wind baseline velocity - solutions that produced cavities with insufficient width would be expected to fall within acceptable bounds given this kind of distortion in initial conditions. It should be noted that relative equatorial over-densities have been extensively used in the literature, notably in many interacting winds simulations, to force bipolarity - unusually, although the causes are quite different, in our simulations it decreases the bipolarity inherent in our jet simulations. It is particularly striking that the cavities begin to display very little curvature in their outer regions, becoming increasingly tubular and bearing a strong resemblance to the outer shells of many bipolar planetary nebulae.

Conversely, an equatorial under-density appears to force a narrowing of the base of the cavities. This, together with the observation that the maximum cylindrical radius extent of cavities in the simulations above tends to be roughly constant, gives the cavities a more conical, less tubular shape. It gives an increase in the strength of the bipolarity as measured in opening angles (Figures 3.22 to 3.25). However, a greater outwards tapering does not fit well with the inferred results of the light

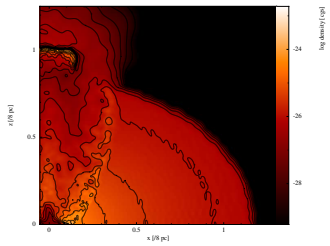

Figure 3.22: Finished jet simulation using a distorted pre-merger RSG progenitor wind (equatorial plane velocities increased by a factor of 2) for a $20\mathrm{kms}^{-1}$ z-velocity RSG wind, $350\mathrm{kms}^{-1}$ fast, hot companion jet with a $10\,\mathrm{deg}$ opening angle. The cavity is initially thinner with a higher gradient at low z than in Figure 3.12(a), the control test for this simulation, and naturally, thinner than the oppositely-distorted Figure 3.18.

echoes (the curvature appears to be mostly at least flat, and possibly tapering inwards). Given these initial conditions, judging by the cavity geometry alone, less of the parameter space explored in the standard simulations would be a good fit to the extrapolated Sugerman et al. (2005) result.

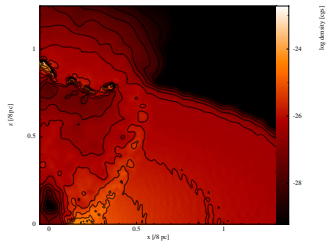

Figure 3.23: Finished jet simulation using a distorted pre-merger RSG progenitor wind (equatorial plane velocities increased by a factor of 4) for a $20\mathrm{kms}^{-1}$ equatorial plane velocity RSG wind, $350\mathrm{kms}^{-1}$ fast, hot companion jet with a $20\,\mathrm{deg}$ opening angle. The cavity is far more conical than in the control, with jet material further out. See Figure 3.13(a).

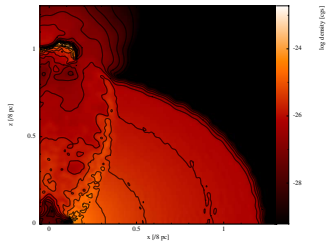

Figure 3.24: Finished jet simulation using a distorted pre-merger RSG progenitor wind (equatorial plane velocities increased by a factor of 2) for a $30\mathrm{kms}^{-1}$ equatorial plane velocity RSG wind, $350\mathrm{kms}^{-1}$ fast, hot companion jet with a $10\,\mathrm{deg}$ opening angle. The distortion gives an initial narrowing of the cavity, tapering to slightly broader relative to the control at higher z as in Figure 3.12(b).

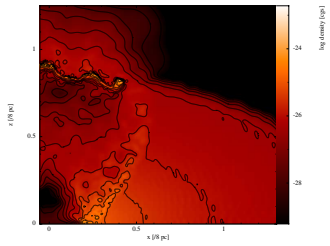

Figure 3.25: Finished jet simulation using a distorted pre-merger RSG progenitor wind (equatorial plane velocities increased by a factor of 4) for a $30\mathrm{kms}^{-1}$ equatorial plane velocity RSG wind, $350\mathrm{kms}^{-1}$ companion jet with a $20\,\mathrm{deg}$ opening angle. The cavity is even broader than in Figure 3.14(b), the control test for this simulation - quite significantly more conical than the cavity shape extrapolated in Sugerman et al. (2005).

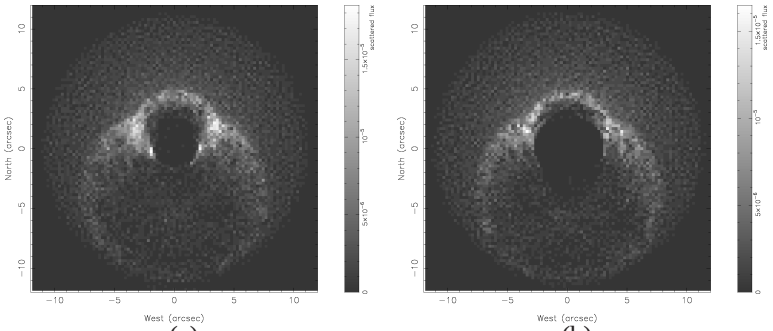

(a) (b)

Figure 3.26: A simulated light echo, 1.8 years post supernova, with a square pulse light curve of 0.3 years duration, in a 24” by 24” field of view, for the following parameters: jet velocity $350\mathrm{kms}^{-1}$, jet opening angle $10°$, and RSG progenitor wind velocity $20\mathrm{kms}^{-1}$ (3.26(a)) and $30\mathrm{kms}^{-1}$ (3.26(b)). Pixel brightness is an approximate proxy for integrated flux. As in Napoleon’s Hat, a central protrusion flanked by wider arcs can be seen, although smaller in extent than observed. In 3.26(b), the central ’bulge’ is shallower in angle where it meets the flanking spurs, and is mildly smaller in distance from the central point, at slightly less than 5” North at maximum.

3.8.3 Simulation light echoes

The simulated light echoes (at 1.8 years post-SN) in Figures 3.26(a) to 3.28(b) contain a mix of apparent geometries - all show a larger southern oval, with a smaller, partially completed northern oval. These correspond to the intersections of the light paraboloid with the northern (further away) and the southern (closer to) cavities, once they have been rotated to an assumed $45°$ angle from the line of sight about the east-west line passing through the origin / light source. Where these align is a function of the curvature and breadth of the cavity near the equatorial plane, and produces an effect similar to the Napoleon’s Hat feature observed at that time in Figures 3.26(a) - 3.27(b), while the larger cavities in the later figures have a much larger northern extent of the southern-based echo and are not satisfactory reproductions. In all cases, the northern extent of the feature at this time is approximately 5”.

Figures 3.28(a) and 3.28(b) demonstrate an envelopment of the central echo by the wider ellipse, and are clearly inaccurate representations of the Napoleon’s Hat features seen in 3.7. We do not observe any particular wide northern echoes,

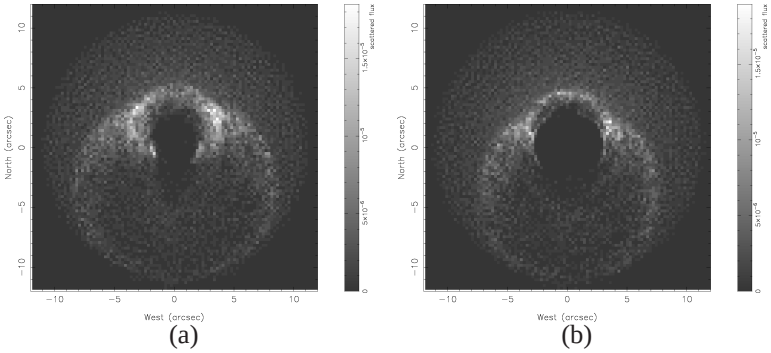

(a) (b)

Figure 3.27: A simulated light echo, 1.8 years post supernova, with a square pulse light curve of 0.3 years duration, in a 24” by 24” field of view, for the following parameters: jet velocity $350\mathrm{kms}^{-1}$, jet opening angle $15°$, and RSG wind velocity $20\mathrm{kms}^{-1}$ (3.27(a)) and $30\mathrm{kms}^{-1}$ (3.27(b)). Compared to Figure 3.26, the flanking arms are much wider, reflecting the larger width of the cavity, and are beginning to flatten the ’hat’ shape found in the earlier figure. The shapes of the echoes between these two are broadly similar, due to the opposing effects of the opening angle and RSG wind velocity on the breadth of the cavity.

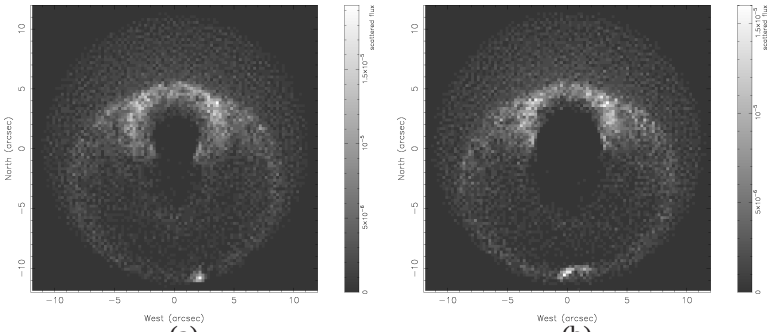

(a) (b)

Figure 3.28: A simulated light echo, 1.8 years post supernova, with a square pulse light curve of 0.3 years duration, in a 24” by 24” field of view, for the following parameters: jet velocity $350\mathrm{kms}^{-1}$, jet opening angle $20°$, and RSG wind velocity $20\mathrm{kms}^{-1}$ (3.28(a)) and $30\mathrm{kms}^{-1}$ (3.28(b)). Compared to Figure 3.26, The pattern of expanding flanking arms has continued, and the central protrusion has been almost completely enveloped. The northwards extent of the echo is still approximately 5”, although slightly larger than the aforementioned figure. Both figures show that the arc of the central protrusion is no longer distinct from the larger flanking arc of the echo from the southern cavity. In 3.28(b), some jet material has been encompassed within the light travel time sphere as well.

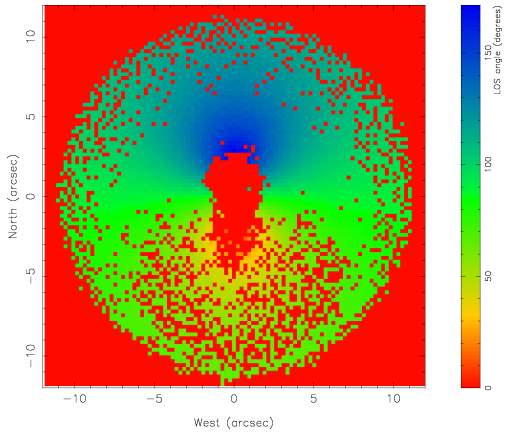

Figure 3.29: The light echoes in a simulation colour coded by mean light deflection - a very rough proxy for the diminution in brightness due to angle-dependent scattering in dust. Blue areas should be relatively decreased in flux, whereas red and green should be relatively brighter. The simulation used was the BSG wind velocity and opening angle $350\mathrm{kms}^{-1}$, $15°$ and the RSG wind velocity $20\mathrm{kms}^{-1}$.

although the natural bounds to the north shown could show a relative enhancement due to angle dependent scattering. The other figures do show the requisite features - in particular Figure 3.28(a) shows a very clear Napoleon's Hat morphology. The southern inner echo or 'Napoleon's Collar' could also be produced here with the addition of the inner CE ejecta, which we have not done in these figures.

Figure 3.29 demonstrates, in a crude way, the angle dependence of the echoes produced - the average LOS (line of sight) angle of the binned (in-pixel) particles is shown colour coded from blue to red, with absolutely red pixels where there is no data (no lit particles). Without assuming an explicit dust scattering angle relation, it is nevertheless likely that the northern echoes should be slightly diminished and the southern echoes slightly enhanced in the Figures 3.26(a) - 3.28(b). It is also important to note that at this point, we have only considered the particle count per bin in determining our flux proxy.

Figure 3.30 demonstrates the echo given by the wider cavity resulting from a lower mass loss rate - an order of magnitude less than in Figure 3.27(a) to which it should be compared. The fit to the observations suggests that exploring lower mass rates trends towards larger disparities (although only two data points are used here). Figures 3.31 and 3.27(b) are the complementary set with companion jet wind

velocity $30\mathrm{kms}^{-1}$ and give the same conclusions.

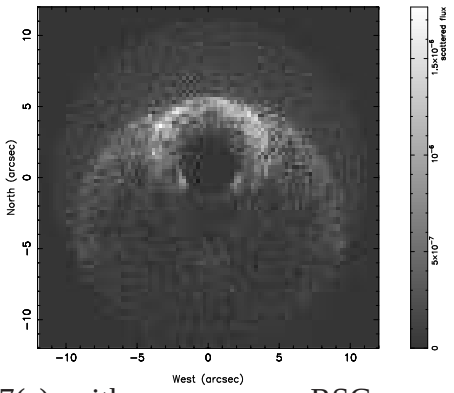

Figure 3.30: As Figure 3.27(a), with a pre-merger RSG progenitor mass loss rate reduced by a factor of 10. The echo shape reflects the trend seen in Figures 3.26(a) to 3.28(b) of broader cavities giving worse fits to observational results at early light delay times.

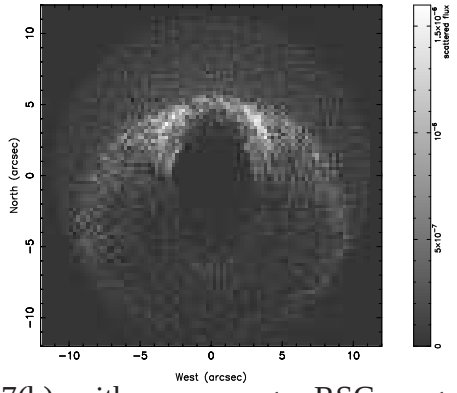

Figure 3.31: As Figure 3.27(b), with a pre-merger RSG progenitor mass loss rate reduced by a factor of 10. As seen in the comparable Figure 3.30, the very broad cavity gives a poor observational fit due to the co-incidence of the two arcs - it is a worse fit than the above-referenced figure.

It is also important to examine the later echoes, which we present in Figures 3.32(a) - 3.34(b), including the simulations which failed to match earlier in order to qualitatively measure the effects of their morphology in the outer layers. The light echoes are simulated at 4 years, corresponding to Figure 3.7e.

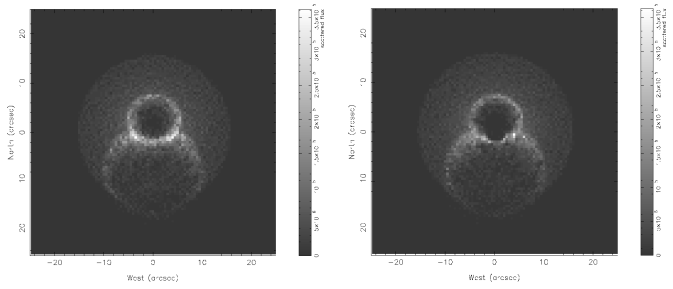

(a) v=20, angle=10 (b) v=30, angle=10

Figure 3.32: Simulated light echoes at a delay of 4 years after the SN. The parameters used were RSG wind: $20\mathrm{kms}^{-1}$ (3.32(a) & $30\mathrm{kms}^{-1}$ (3.32(b), BSG wind velocity and opening angle $350\mathrm{kms}^{-1}$ and $10°$ respectively.

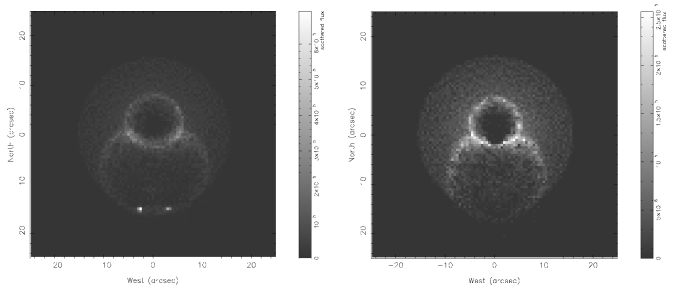

(a) v=20, angle=15 (b) v=30, angle=15

Figure 3.33: Simulated light echoes at a delay of 4 years after the SN. Parameters for the simulations are as Figure 3.32, but with an opening angle of $15°$.

Figures 3.32 to 3.34 show the larger scale light echoes in the simulations, 4 years post SN. The flux is based on column density, as before, and makes no allowances for angle dependent scattering. They are intended to be compared to Figure 3.7 e), which shows a wider half-ellipse (blue) around a central oval/Napoleon's Hat echo. The southern extent of the large echo is approximately 15 arcseconds, whereas the northern extent of the Napoleon's Hat structure is well below 10 arcseconds at this time. In our figures, the Napoleon's Hat wings and larger ellipse are part of the same structure, and we do not reproduce the isolated eastern northern parts of the large ellipse seen in Figure 3.7. We do however reproduce the general morphology quite well, including in particular the southern 'Napoleon's Collar' and the southern extent of the southern echo.

Figure 3.34(a) particularly well represents the southern extent of the echo, al-

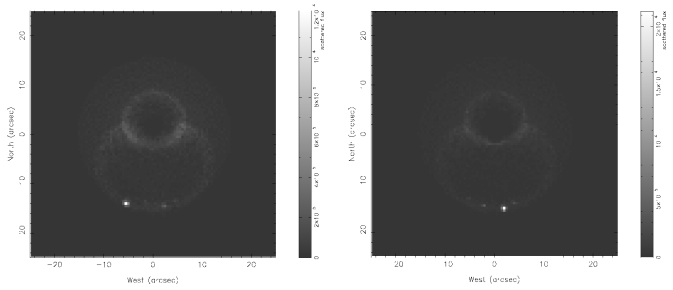

(a) v=20, angle=20 (b) v=30, angle=20

Figure 3.34: Simulated light echoes at a delay of 4 years after the SN. Parameters for the simulations are as Figure 3.33, but with an opening angle of $20°$.

though the curvature at the southern edge is more defined in the figure above it, Figure 3.33(b). We find that for the large scale echoes, the mid to large opening angles better represent the morphology and extent, although the Napoleon's Hat structure is slightly over large in all of these.

3.8.4 Offset study

The best fit found in Sugerman et al. (2005) was found under the assumption that the assumed axis of symmetry of the bipolar cavity passed through the light echo source (the supernova and its originating star). We note that the best fit found in Morris (DPhil thesis) for the triple ring nebula also included a small displacement of the central star due to a merger kick. It is clearly worth exploring the effect this would have on our models.

A 2 kilometres per second kick at merger, slightly out of the equatorial plane and north-west in the plane of the sky gave the best fit to the offset within the three rings - this equates to 0.04 parsecs, or 0.13 light years over 20000 years, using the approximate metric that 1000 kms^{-1} for 1000 years gives a displacement of 1 parsec.

An offset in the plane of rotation could lead to an east-west distortion in the echo shapes, with greater echo curvature in the direction of the offset. We note that large asymmetries in the east-west echoes are not well supported by the observations, suggesting that if there was a mechanism producing an especially large offset, it would need to be 'fine tuned' to the correct set of directions.

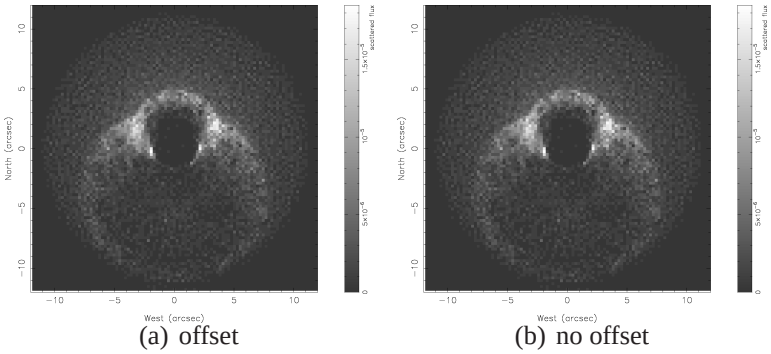

(a) offset (b) no offset

Figure 3.35: The offset (3.35(a)) compared to the control (3.35(b) as Figure 3.26(a)), with a 0.14 light year offset north and west, up and right in the image, of the cavity from the central source.

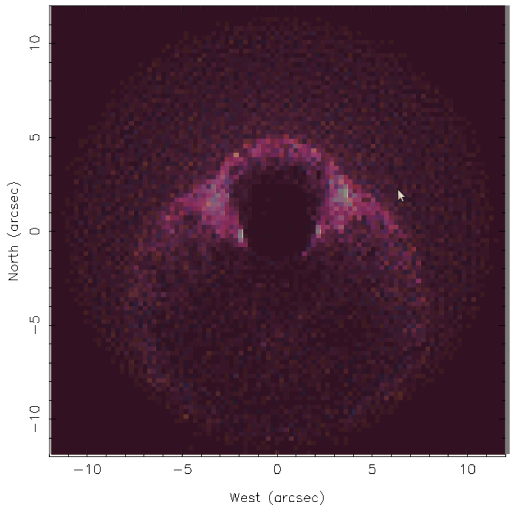

Figure 3.36: Red - blue differences between Figure 3.35 and Figure 3.35. The echo from an offset light source (red) produces a larger southern echo.

We compare the effect of an offset on a light echo with the original in Figures 3.35 and 3.36, where we show the offset, the original, and finally a red/blue difference image in the last figure. Figure 3.36 shows areas in the two images that are different - redder pixels are the offset echo, and bluer ones are the original. Although it is a noisy image, it displays a clearly larger southern echo for the offset. However, compared to the differences between our set of simulations shown, a 0.14 light year offset does not significantly change the conclusions. For larger scale

echoes, a 0.14 light year displacement in a 4 year delayed echo should produce a smaller effect.

3.9 Conclusion

We studied the effect of varying speeds and geometries, amongst other factors, in an interacting winds, fast jet to slow wind, series of models. We then directly matched the effects of these parameters to observed light echoes. Early time echoes support smaller opening angles, less than 15 degrees, with slower winds being a better fit to the Napoleon's Hat feature and others (20 rather than 30 kms^{-1}). In later echoes, mid to large opening angles give a better fit to the large southern echo. However, it is striking that simulations which produce quite significantly different shapes of cavity support the same basic set of echo features.

All standard simulations can be affected significantly by variations in the pre-merger RSG progenitor wind mass loss rate and velocity distribution. However, it seems quite difficult, with our choice of ranges of parameters, to reproduce a inwardly tapering double cone as inferred by Sugerman et al. *2005). Tubular and outwardly tapering cavities are relatively easy to produce - outwardly tapering or conical cavities are a natural convergence in the limit of very low mass loss and conical jets. Tubular cavities result when the collision shock velocity is sufficiently great in the denser interior to counteract this.

It should be noted that in addition to the natural breadth of any jets produced, an additional spread due to the orbital motion of the jet-producing companion would lead to a larger opening angle, as the jet producing phase should be much longer than a single orbit. Although the results are not shown here, in the limit of a very small natural opening angle and large tangential orbital velocity (a significant fraction of the $350\mathrm{kms}^{-1}$ jet) a conical, 'hollow' jet can be produced. A hollow jet gives very similar results to the standard one, where deceleration is negligible. It does produce some interior structure on the axis of the jets, where the pre-merger RSG progenitor wind has been 'threaded' through the hollow and jet material has been stripped. However these structures, which correspond to Sugerman et al. (2005) 'jet' material, can easily be replicated by the hydrodynamic instability shredding of the jet in other simulations.

In summary, we have shown that the 'outer structure' short to long term light echo features of the last 20-odd years can be reproduced by small to medium opening angle jets launched into an existing slow $\rho \propto \mathrm{r}^{-2}$ wind, with parameters consistent with the binary picture elucidated in papers such as Morris & Podsiadlowski (2007). We find, as in Sugerman et al. (2005), that it can be explained by a bipolar waisted cavity, with the famous three rings at the very centre. Light scattering and light ionisation features have played a central part in the gradual unravelling of the mystery of SN 1987A's nebula, which is integral to the mystery of the supernova itself. The last-discovered, earliest-time features of the mass loss history of SN1987A seem to suggest the last piece of the nebular mystery is the earliest part of the binary story.

Chapter 4

Cassiopeia A

4.1 Introduction

The supernova remnant Cassiopeia A (Figure 4.1) is one of the youngest and most unusual in the Galaxy. The light from the supernova itself reached Earth in 1681 ± 19 AD (Fesen et al. 2006), but it appears to have been too faint to be detected unambiguously (although see Hughes 1980). Instead, the remnant was detected in the radio by Ryle and Smith (1948).

When identified in the optical, the remnant was found to have distinct asphericity. It had a prominent jet (Minkowski 1968), a weaker counter-jet and both low and high-velocity knot ejecta (Fesen et al. 2001, 2006, Hammell & Fesen 2008), with pronounced structural elemental abundance differences indicating substantial mixing (Chevalier and Kirschner 1978,9). An X-ray point source, presumably the remnant neutron star (NS), was discovered (Tananbaum 99), and found to be displaced orthogonal to the jet/counter-jet axis of Cas A - if it is the remnant star, it would have a transverse velocity of approximately $350 \mathrm{kms}^{-1}$ (Thorstensen et al. 2001, Fesen et al. 2006).

This is particularly interesting, as if the jets were driven by a bipolar instability in the heart of the supernova, the neutron star might be expected to be displaced along this axis, instead of orthogonal. The X-ray source can be seen as a yellow point near the centre of Figure 4.1. This stellar object, which is likely to be a neutron star, does not appear to be a pulsar - it is devoid of a pulsar wind nebula (Hwang et

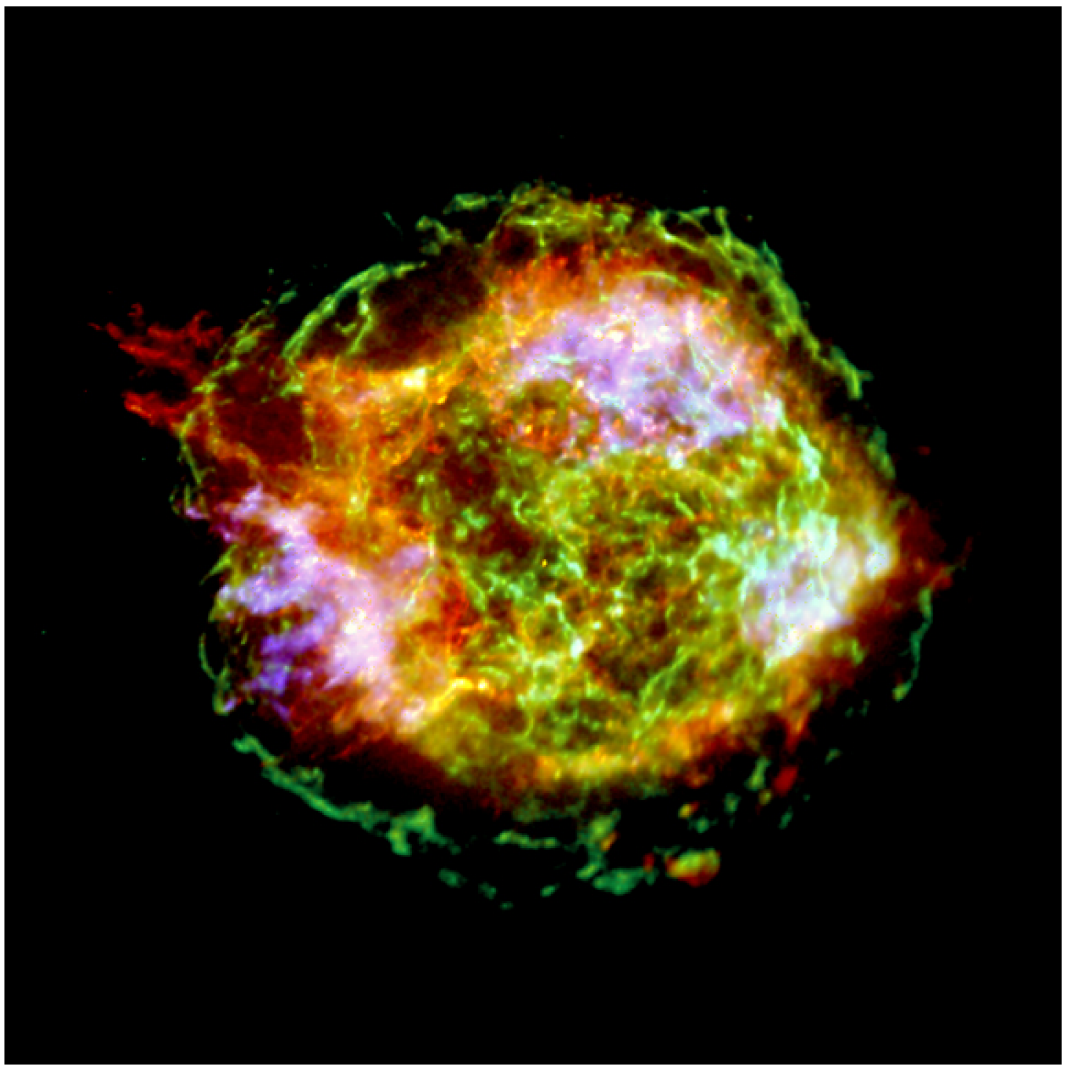

Figure 4.1: The Cassiopeia A supernova remnant in X-rays (Hwang et al. 2004). The jet extending towards the top left of the figure, the weaker counter-jet extending opposite it, and the yellow displaced X-ray point source can be seen clearly.

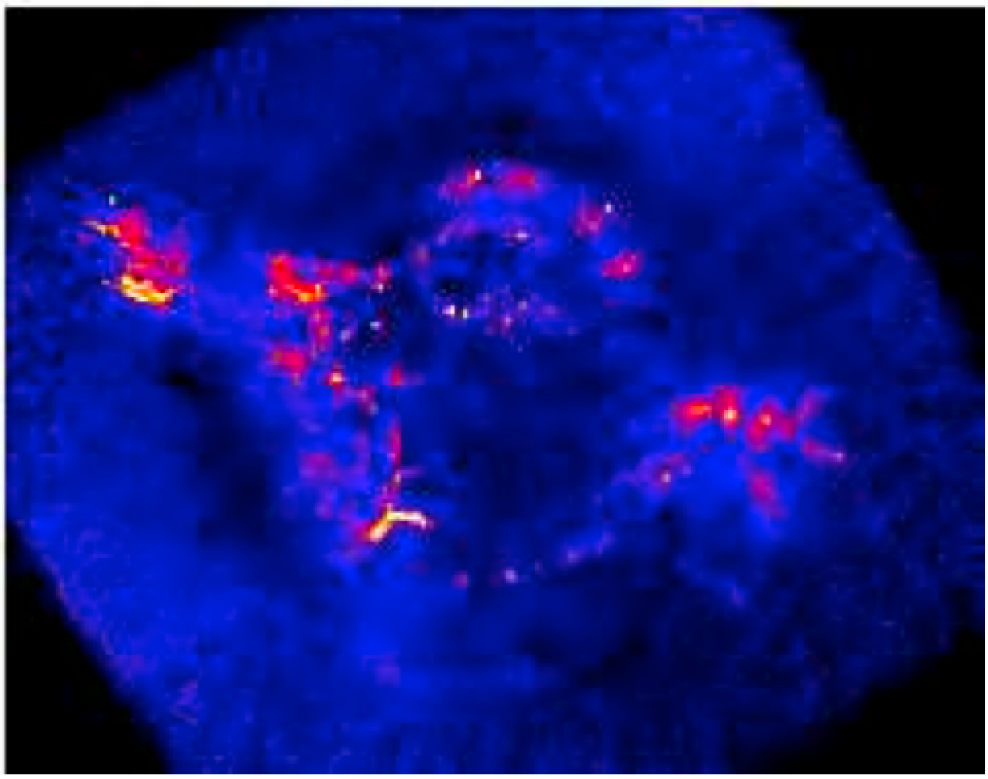

Figure 4.2: Cas A X-ray band ratio (1.78-2.0 keV to 1.3-1.6 keV) showing Si emission in the reverse shock and jets (Hwang et al. 2004).

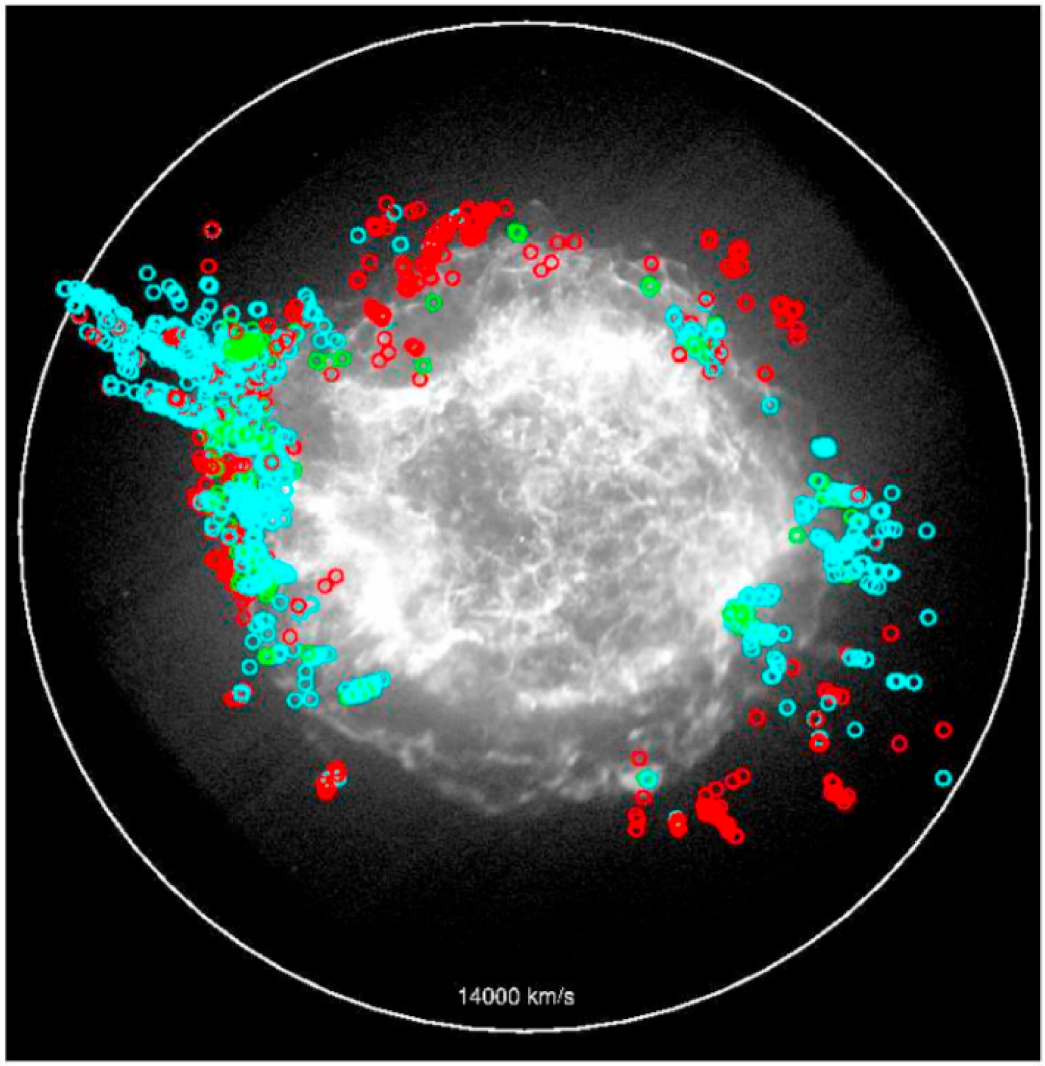

Figure 4.3: Knot positions figure from Fesen et al. 2006 showing [N II] emission in red, [O II] in green, and [S II] in blue. Normal stellar elemental layering is preserved except in the jet regions.

al. 2004) and no regularity in emission has been detected (e.g. De Luca 2007). It has been hypothesised to be a dormant magnetar from infrared light echoes pointing to a possible flare-like event in the last century (Krause et al. 2005).

The study of Cas A is of huge relevance to many other fields; in particular in the fields of core-collapse and GRB simulations, the mechanics of which remain two of the outstanding mysteries in stellar astrophysics. If Cas A had been a typical core-collapse supernova (to the extent to which they can be characterised as standard,) it would still remain a very interesting supernova remnant by virtue of its proximity and young age. However, in common with SN1987A (discussed elsewhere in this thesis), the supernova appears to have been quite unusual in its luminosity and asphericity [1]. Cas A is a 'laboratory' for remnant cosmic ray production (Ona-Wilhelmi et al. 2008, Abdo et al. 2010), neutron star equation of state and outer envelope studies (Heinke & Ho 2010), and ISM studies (e.g. Kim et al. 2008). It has also been used to probe Type II supernova dust production, a vital question for the unresolved problem of over-abundance of dust at high redshift (e.g. Rho et al. 2007).

Cas A is chemically inhomogeneous as well as kinematically inhomogeneous. In the south-eastern limb the normal stellar onion-like layering of elements is largely preserved in N, O and S with some Fe infiltration (see Figure 4.3) into the S layer (Fesen et al. 2005), while the NE jet is largely S-rich (Fesen et al. 2006) with very little Fe (Hughes et al. 2000). Successful models must introduce some kind of turbulent motion or dramatic instability to disturb the progenitor chemical profile.

Although chemical and kinematical evidence establishes the NE and SW jets as unambiguous phenomenona, there have been suggestions that the main mass axis of the explosion lies in the N-S direction along the presumed neutron star kick, defined by two significantly Ne-rich 'crescents' in the north and south of the remnant (Burrows et al. 2005, Wheeler et al. 2008, DeLaney et al. 2010, Rest et al. 2011) - although these are in part hypothetical based on jet-NS alignment predicates (Wheeler et al. 2008). Rest et al. (2011) in particular associates a higher kinetic energy to the northwards, compared with NE and SW directions, from a light echo

[1] Although an analogue has been recently discovered - SNR 1R 0102.2-7219 - with an apparently intrinsic bipolar asymmetry (Vogt & Dopita 2010). SN 2008ax also had an intrinsically aspherical explosion, as revealed by Hα polarisation (Chornock et al. 2010).

study. This axis also passes through areas identified by Fesen et al. (2006) and Hammell & Fesen (2008) where no high-velocity knots appear. This introduces yet another potential axis for modellers to consider.

Light echo spectra establish the supernova as Type IIb (Krause et al. 2008) or 1993J-like (Matheson et al. 2000) - indicating that the progenitor had lost nearly all its hydrogen envelope before undergoing core collapse. However, the circumstellar medium (CSM) appears not to have been consistent with a WR phase, indicating possible binary influence (Schure et al. 2008, Van Veelen et al. 2009); instead it appears to have been a $\rho \propto r^{-2}$ profile fast wind (Chevalier & Fransson 1993, Hwang & Laming 2009, Nozawa et al. 2009). A CSM-induced asymmetry in the ejecta has also been ruled out, based on knot survival and reverse shock propagation (Laming et al. 2006), and it appears that the supernova explosion itself was asymmetrical (Rest et al. 2010). Typical estimated mass loss rates for a pre-SN wind are of order $2 \times 10^{-5} M_{\odot} \mathrm{yr}^{-1}$ (Chevalier & Oishi 2003, Nozawa et al. 2010). It appears that the causes of the unusual features in Cas A were tightly coupled to the early explosion, and the mass loss certainly suggests binary influence.

The total mass in the ejecta is estimated at approximately $2 - 4 M_{\odot}$ (Vink et al. 1996, Franssen et al. 1997, Willingale et al. 2003).

4.2 Core-collapse supernovae and Cas A

Events with energies of order 1 Bethe (10^{51} ergs) that do not show strong absorption in the Si II 6150 angstrom line region are strongly believed to be the result of gravitationally-powered core-collapse in massive ($> 8 M_{\odot}$) stars. The natural endpoint for nuclear fusion is silicon fusion, which produces functionally inert iron nuclei. When a core of iron nuclei is built up whose mass exceeds the Chandrasekhar limit of approximately $1.4 M_{\odot}$, a critical moment is reached. Neutrino losses from electron-positron annihilation at the extremely high core temperatures, electron capture, and photodisintegration of the Fe nuclei by extremely high energy photons force the core to contract, either reaching a limit in neutron degeneracy pressure at nuclear densities or, in more massive stars, forcing the creation of a black hole in the inner core (for a review, see Woosley & Janka 2005). In the case where the collapse does not immediately create a black hole, but stops at the creation of a small core

of nuclear-density material (a proto-neutron star) the transition from almost unopposed infall to active repulsion generates a shock wave or 'bounce' in the outer core regions which was originally proposed as the driver for the injection of the extracted gravitational potential energy into the envelope, powering the supernova (Colgate et al. 1961). However some of the same mechanisms that accelerated the collapse of the core also affect the shock - photodisintegration and electron capture leading to neutrino losses stall the shock and lead to accretion back onto the proto neutron star, which can then collapse into a black hole (see Janka et al. 2007). However the neutrino luminosity from the proto-NS (from approximately 10% of the NS rest mass energy) is theorised to revitalise the shock if a tiny fraction is absorbed - of order 1% - to create the 1 Bethe, 10^{51}erg explosion. Strong evidence supporting the basic core-collapse theory comes from the detection of neutrinos from 1987A, as discussed in Chapter 4.

However, the successful re-launching of the shock from delayed neutrino absorption appears to be a strongly three-dimensional fluid dynamics/neutrino physics problem (although a different possible mechanism is proposed in Burrows et al. (2006)), beyond the state of the art computing capabilities at present (Nordhaus et al. 2010). The evidence suggests that the detailed physics involved in relaunching the shock is strongly non-spherically-symmetric, with a bipolar component noted in 2D simulations (Blondin et al. 2003). If the jets in Cas A were proved, or proved not, to be a result of a bipolar core instability, this would be particularly relevant for this ongoing research. Our simple models can't compete with the state of the art in the core of the supernova, and these, arguably, cannot yet compete with reality in three dimensions. We therefore only consider 'toy' models rather than attempting more sophisticated modelling.

Core collapse supernovae can lead to neutron star natal kicks, which are thought to be derived from some asymmetry in the supernova itself - these are implicated in the anomalous velocity distribution of radio pulsars (Lyne & Lorimer 1994) and the close orbits of NS-MS low mass x-ray binaries (LMXBs) (Kalogera 1997) amongst other evidence. The observed kick of the Cas A X-ray source can give valuable constraints on this process, which is normally statistically recovered - however this is only really the case if we assume the X-ray source is the remnant of the Cas A supernova. We assume that the X-ray source could also have been a companion

object, and to that end don't consider the supernova to create a 'kicked' object explicitly. This also would create a much larger parameter space for the simulations, which is out of the scope of this work.

If the Cas A NE/SW asymmetry and the NS kick are produced by the supernova explosion mechanism itself, in a simple dipolar model the jets of Cas A should then be on the same axis as the neutron star candidate displacement, instead of almost perpendicular. If the supernova was jet-powered, the jets should have more energy as well and be more enriched in core elements - some of the main reasons Wheeler et al. 2008 cite as evidence that the real polar axis of the supernova is approximately along the NS kick. However, no models account for the lack of an equatorial torus in a plane perpendicular to the plane of the sky, which should be produced by jet-driven supernovae and is not found - instead the ejecta appears flattened in the plane of the sky (DeLaney et al. 2010). This provides the motivation for considering alternative hypotheses for creating the asymmetries.

Cas A and its interesting departure from classical soap-bubble shaped, onion layered core collapse 'piston' models has implications for high redshift dust production, ISM chemical enrichment, and many other fields, but most of all in the detailed, as yet unsolved workings of the heart of core-collapse supernovae.

4.3 Binary hypothesis

We believe that the alignment of the jets and the orthogonality to this of the neutron star kick, together with non-WR hydrogen stripping (as has been noted elsewhere, see above) and confinement of the ejecta towards their plane, is evidence for a high angular momentum, probably binary interaction-induced environment.

Production of jets along the line connecting the binary stars, and the subsequent unbinding of the system could replicate the orthogonal kick of the remnant NS relative to the jet axis, as shown schematically in Figure 4.4. In this picture, a jet is formed by the gravitational influence of the companion on proximal ejecta (labelled P, termed the primary jet in this work) and another enhancement is due to tidal displacement of the core relative to the envelope in the other direction (labelled S, termed the secondary jet). This hypothesis allows us to dropping the requirement that the jets be integral to the supernova mechanism itself, and keep the jets only

weakly energetically distinct, as observed.

In addition, the plane of the jets and NS-kick should be the orbital plane where most material could be shed, possibly reproducing the flattened ejecta seen in DeLaney et al. (2010). The motivation for studying the possible link between binarity and the jets of Cas A and the idea for the physical mechanism for the secondary jet came through Danail Obreschkow, which is discussed in the 'Secondary jet' section.

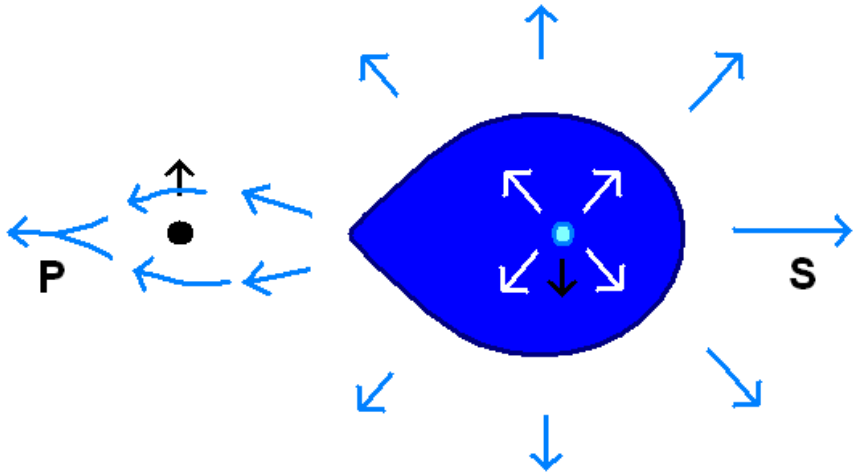

Figure 4.4: A SN progenitor in a binary system could provide the required geometry seen in the Cas A remnant. Jets would outflow towards the companion, and be enhanced away from it by an asymmetry in the core-envelope position. After the supernova, the proto-neutron star and the companion would move away from the explosion centre, approximately orthogonal to the jet axis, as is seen in Cas A.

Parameter	Description	Values used
α	Fraction of binding energy deposited	0.4, 0.8
M_{pp}	Companion (point potential) final mass	7, 10

Table 4.1: Parameters used in these simulations.

4.4 Modelling

4.4.1 Primary jet

Method

To test the binary hypothesis, we set up a $7.7M_{\odot}, \approx 1R_{\odot}$ core radius helium star model (the primary in our binary paradigm), provided by my supervisor's stellar evolution codes, in close orbit with a point gravitational potential which represents a compact companion - either a white dwarf, neutron star, or black hole. We refer to this compact companion as the secondary. We then explode the 'primary' and explore the effects of the compact companion on the ejecta.

The stellar model for the primary is limited at the stage of carbon burning, but can be centrally condensed artificially by selective, gradual core cooling. However, as the condensation of the central core does not significantly affect the shock propagating into the envelope we have neglected this. It would certainly be preferable in future work.

In order to set up the binary, the point potential initially has zero mass, in effect a test particle, with the central model rotating synchronously to the particle orbit. We then increase the mass of the point potential in increments, preserving orbital separation and increasing the spin of the primary as the period decreases.

The velocity field imposed on the SPH particles of the primary has an effect on mass transfer where the conditions for Roche lobe overflow apply, until the point potential mass is incremented fully. For this reason, and because significant mass transfer on dynamical timescales is unstable and unlikely to coincide with the supernova, systems with parameters that cause rapid mass transfer to the secondary are not considered.

We then deposit a fraction of the binding energy of the primary into the inner 1.5 solar masses of its core, as a rough analogue (almost cartoon) of the core collapse

shock initiation.

As these simulations are relatively cartoonish, involving toy models, we look to create some bipolar overdensity or overvelocity in the ejecta, and hopefully some qualitative chemical inhomogeneity.

At first, we consider the raw effect of the companion, for various orbital, mass, and gravitational softening parameters as the ejecta passes over it, shown below.

Results

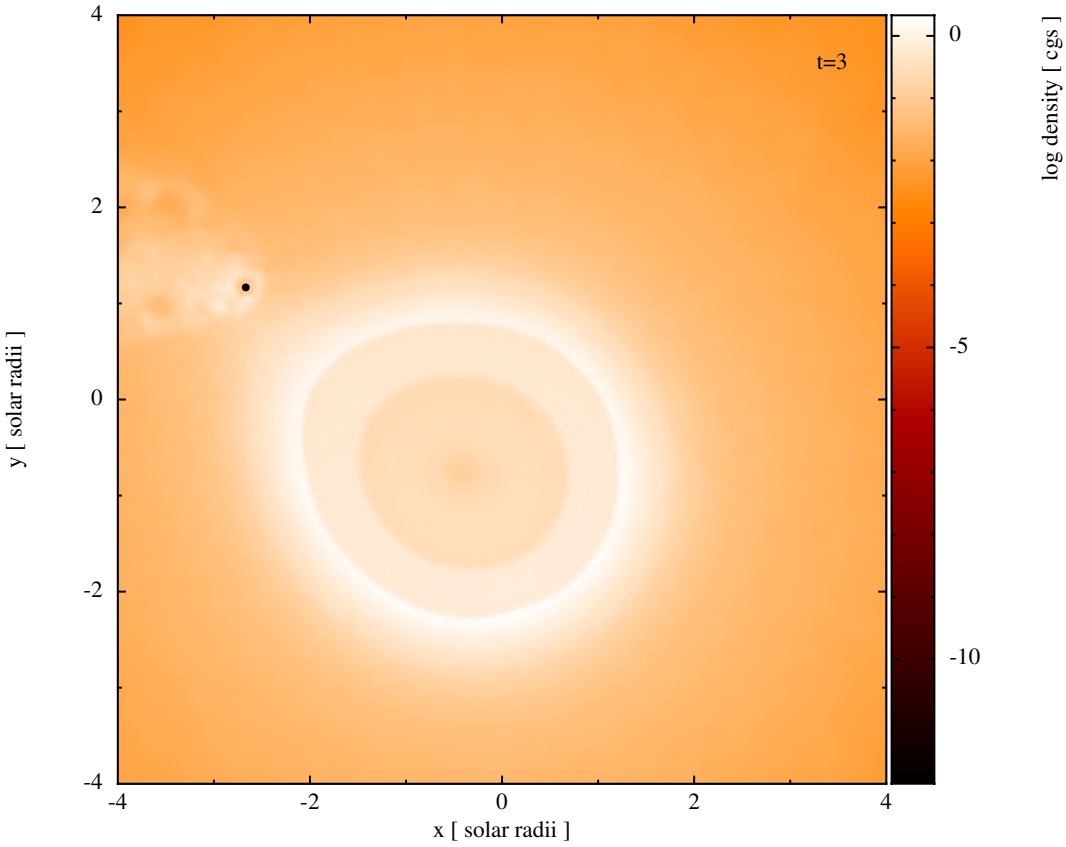

Figure 4.5: Early weak jet/tail production (top left) from the companion (solid black circle) in a density-highlighted cross section of a test simulation. The time is about 3 primary dynamical timescales post-injection of energy. Axes are cartesian coordinates in solar radii, density is in log cgs.

Figures 4.5, 4.6, and 4.7 show the density evolution of the primary's ejecta over

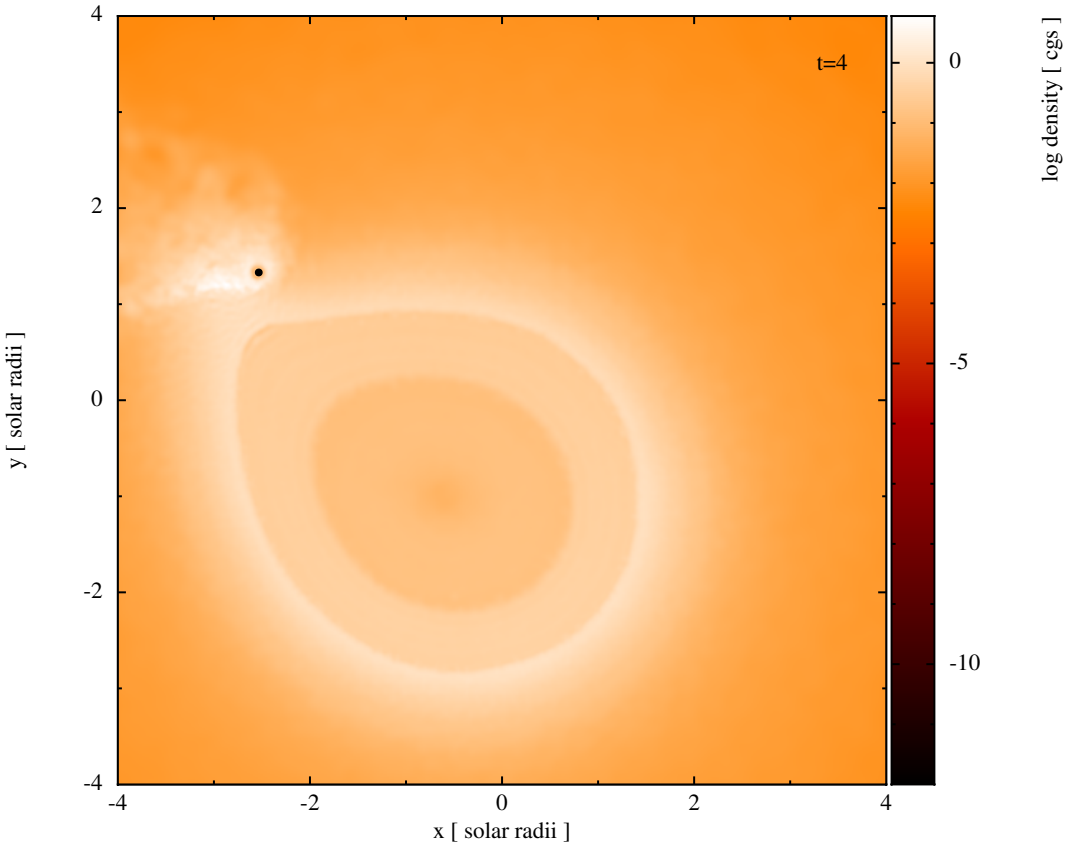

Figure 4.6: Jet/tail production in the top left from the companion (solid black circle) in a density-highlighted cross section of a test simulation. The time is about 4 primary dynamical timescales post-injection of energy. Axes are cartesian coordinates in solar radii, density is in log cgs.

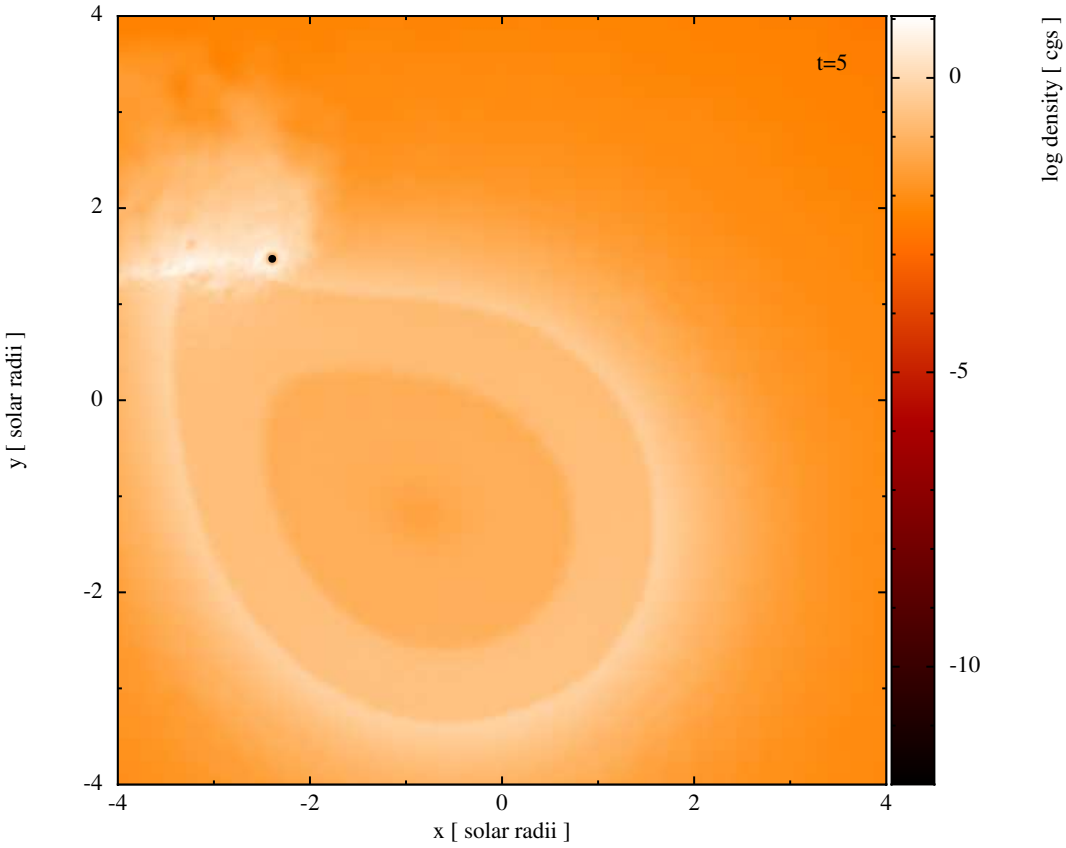

Figure 4.7: Late, strong jet/tail production relative to Figure 4.5 from the companion (solid black circle) in a density-highlighted cross section of a test simulation. The time is about 5 primary dynamical timescales post-injection of energy. Axes are cartesian coordinates in solar radii, density is in log cgs.

the course of a few dynamical timescales. Pixels which do not contain particles are shaded at the minimum colour. The shock becomes noticeably distorted as it passes close to the companion, which precedes the main distortion in its orbital direction. As material flows close to the companion (blue circle), it is focused into a density-enhanced tail as seen in mass transfer simulations (e.g. Mohamed et al. 2010) which is truncated after the substantial majority of material passes outside the companion's orbit.

The corresponding absolute velocity over time relative to the centre of mass velocity of the system can be seen in Figures 4.8, 4.9 and 4.10. The formation of an accretion disk can also be seen in the top left of Figure 4.7 around the companion, due to the shaded velocity field. The unbound movement of the companion in an approximately perpendicular direction to the tail/jet velocity vector can be seen as the displacement of the black solid circle from the axis of the top left jet feature in Figure 4.7. While the jet is not particularly distinct in velocity space, unlike the Cas A remnant jet-counter-jet velocities, we posit that some significant uniform circumstellar medium interaction (sufficient to decelerate the highest velocity ejecta slightly) would allow the feature to be relatively enhanced in velocity compared to the rest of the ejecta.

We do not observe a jet in the other direction, which leads us to explore other possibilities for the companion's influence.

The jet produced can be seen in cross section in Figure 4.11 at a later time. The distortion in the ejecta can be clearly seen in the top left. The jet also has a slightly bifurcated morphology, as seen in the NE jet in Cas A - however the reproduction of this precise piece of morphology is not strictly necessary, as various instabilities in the SNR could create this level of disruption in any event (c.f. the knots in Figure 4.3).

To assess the likely strength of the jet formation process, we have performed a parameter study over companion mass, orbital separation, and companion gravitational softening, shown in Figure 4.4.1. The companion mass not only affects the companion tidal asymmetry and the SN ejecta through gravitational influence, but controls the orbital velocity of the companion and the primary relative to each other and to the system centre of mass. The orbital separation has a similar effect, and has a particularly strong effect on the solid angle of ejecta that can be substantially

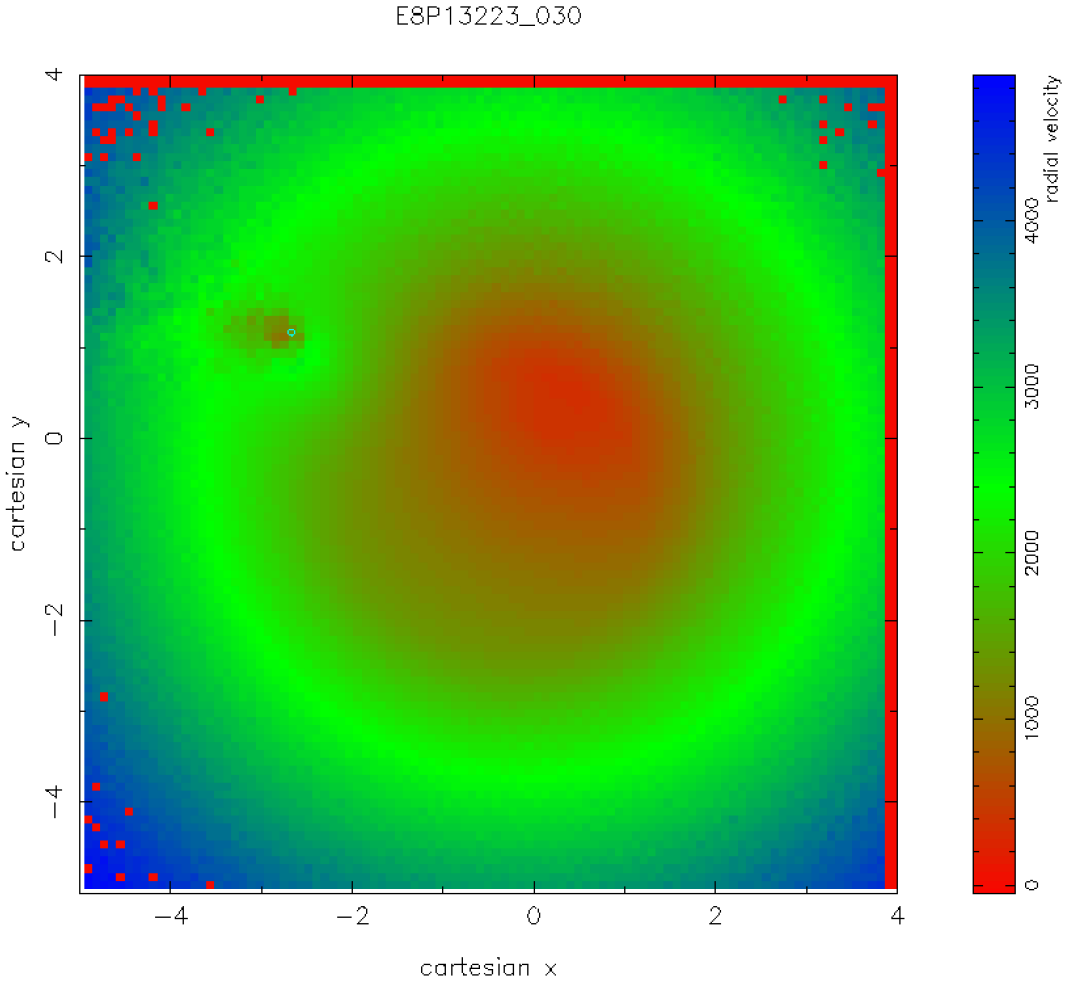

Figure 4.8: Early weak, fast jet/tail production from the companion (blue circle) in a radial velocity-highlighted cross section of a test simulation. The time is about 3 primary dynamical timescales post-injection of energy. Axes are cartesian coordinates in solar radii and radial velocity is in kms^{-1}.

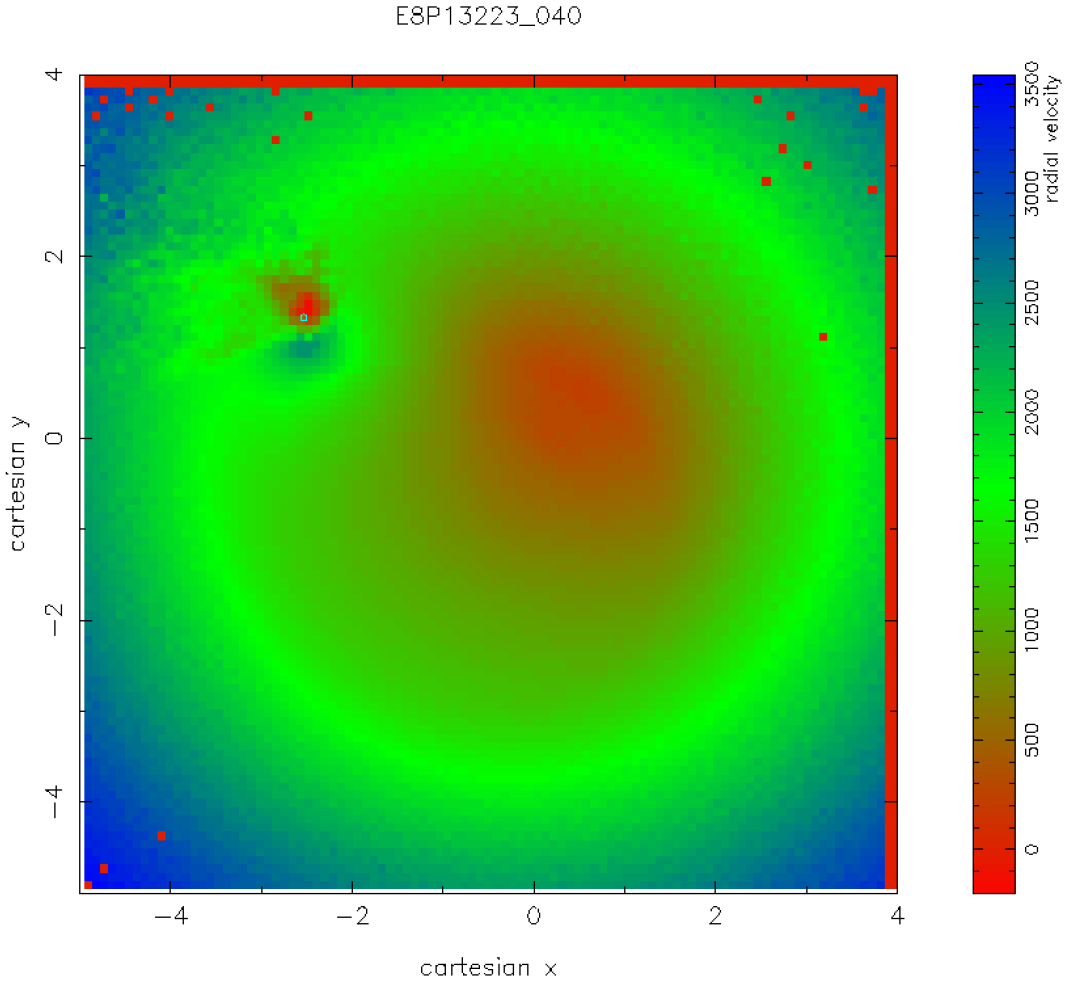

Figure 4.9: Jet/tail production from the companion (blue circle) in a radial velocity-highlighted cross section of a test simulation. The time is about 4 primary dynamical timescales post-injection of energy. Axes are cartesian coordinates in solar radii and radial velocity is in kms^{-1}.

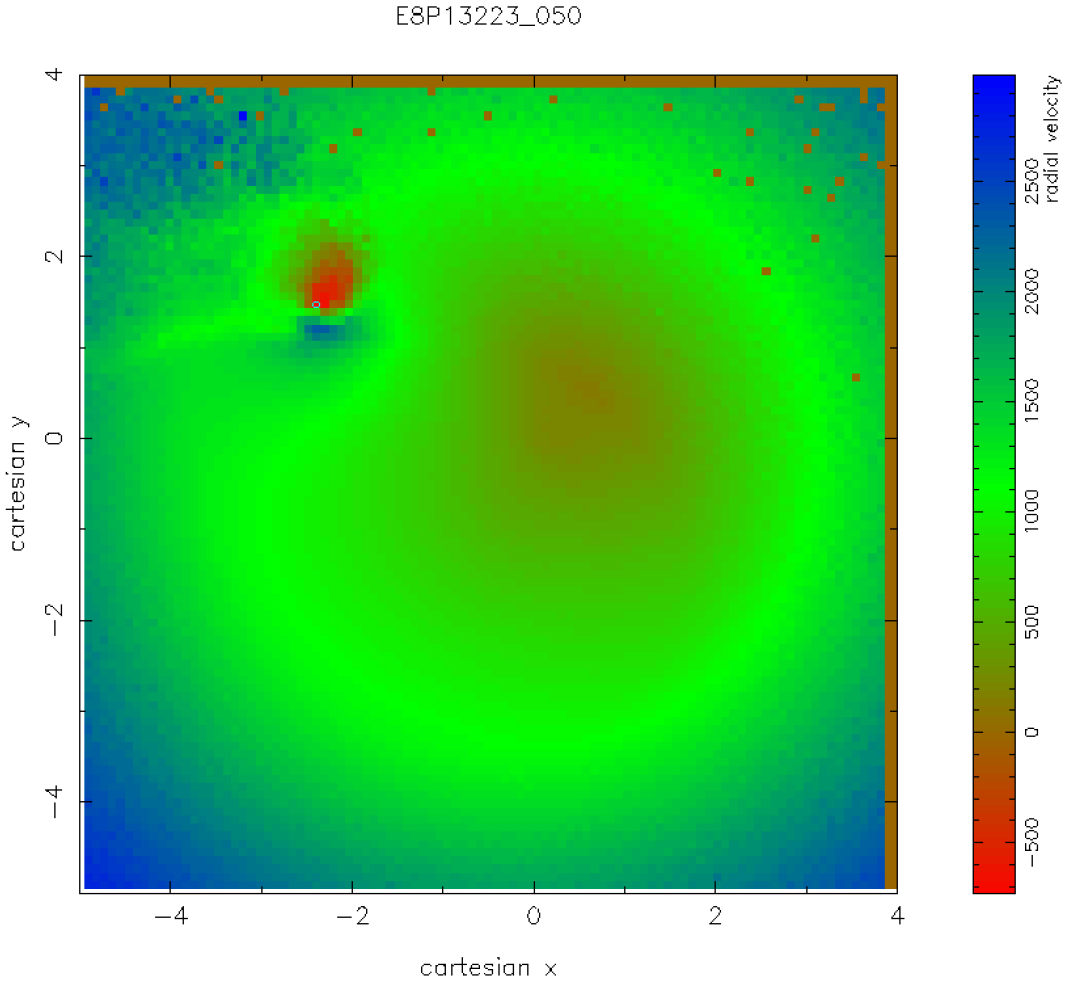

Figure 4.10: Late strong, slow jet/tail production from the companion (blue circle) in a radial velocity-highlighted cross section of a test simulation. The time is about 5 primary dynamical timescales post-injection of energy. Axes are cartesian coordinates in solar radii and radial velocity is in kms^{-1}.

gravitationally influenced by the companion. The gravitational softening parameter is notorious in N-body and SPH simulations for producing spurious accelerations of particles that approach within approximately this value, depending on the formalism adopted. Here we have the magnitude of the gravitational force from the companion as:

$$F_{i_g} = \frac{\mathrm{GM_{comp}m_i}}{\mathrm{r_i^2}}(\mathrm{r_i} > \epsilon) \tag{4.1}$$

$$F_{i_g} = \frac{\mathrm{GM_{comp}m_i}}{\epsilon^2}(\mathrm{r_i} \leq \epsilon) \tag{4.2}$$

where ϵ is the gravitational softening, $\mathrm{m_i}$ is the distance between the companion and the SPH particle, $\mathrm{m_i}$ the mass of the SPH particle, $\mathrm{M_{comp}}$ the mass of the companion, and G as the gravitational constant. While only a fraction of ejecta is Bondi-Hoyle accreted by the companion and will approach ϵ-magnitude distances (substantial losses of angular momentum are needed), this material will be quite capable of influencing the surrounding ejecta hydrodynamically. The gravitational softening is therefore an important factor to test, which is shown in Figure 4.4.1.

The knots in the NW jet are S-rich (Fesen et al. 2006) and therefore should originate from deeper inside the star than would otherwise be expected. Although the stellar model is not a close match to a pre-supernova, iron cored star, we attempt to test the predicted inversion qualitatively by colour coding the material in the ejecta by its original depth in the star. This can be seen in Figure 4.12. This shows a slight increase in deeper-layered ejecta relative to the rest of the star, which could explain the S-rich knots at further distances, but suggests that the jet is not qualitatively different in other elements.

We originally hoped to create not only a disturbance or enhancement following from the ejecta flowing past the secondary, but also some enhancement in the ejecta in the opposite direction, as observed. This was not evident in the simulations performed above, leading to a slightly different examination of how another jet could have been produced in that direction, below.

We term the most promising jet production method, above, the primary, and the following method the secondary.

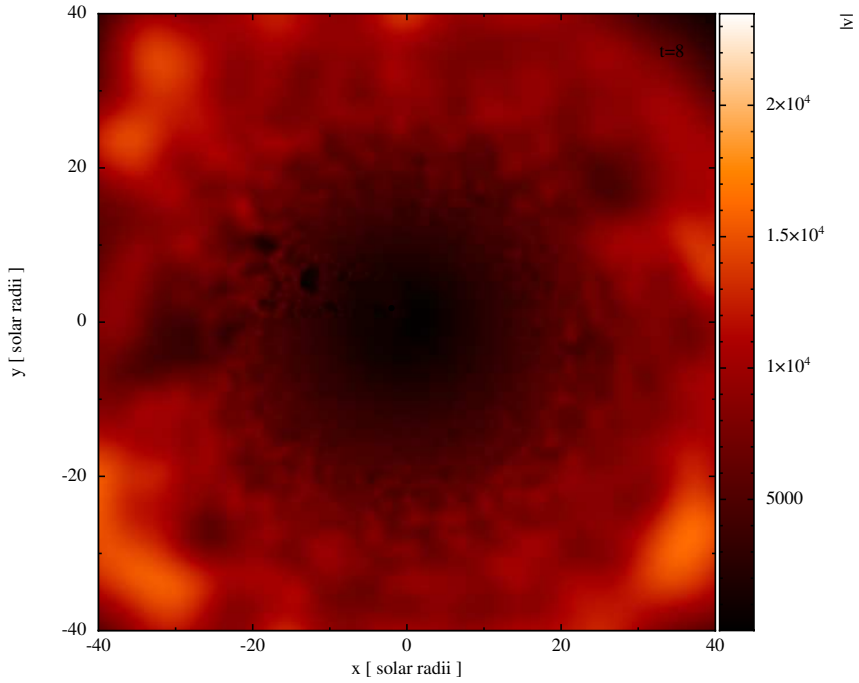

Figure 4.11: Jet appearance at 8 dynamical timescales post-injection of energy in the example simulation. Axes are cartesian coordinates in solar radii, with a cross section in z, and colour coding is by velocity magnitude in cms^{-1}.

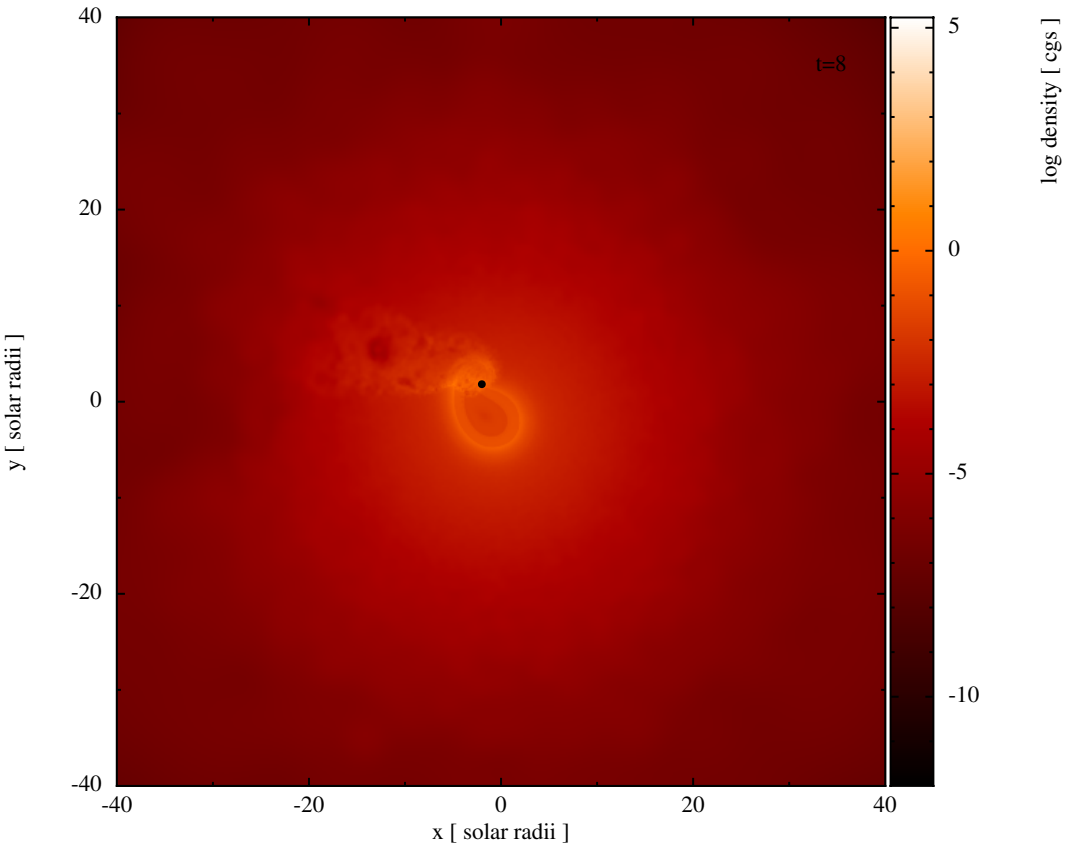

Figure 4.12: Jet appearance at 8 dynamical timescales post-injection of energy in the example simulation. Axes are cartesian coordinates in solar radii, with a cross section in z between -0.5 and 0.5 (plot units), and colour coding is by original density of the material in the star before the explosion, as rendered by SPLASH in place of the normal particle density, if this is to be trusted. The jet is mildly enhanced relative to the rest of the ejecta.

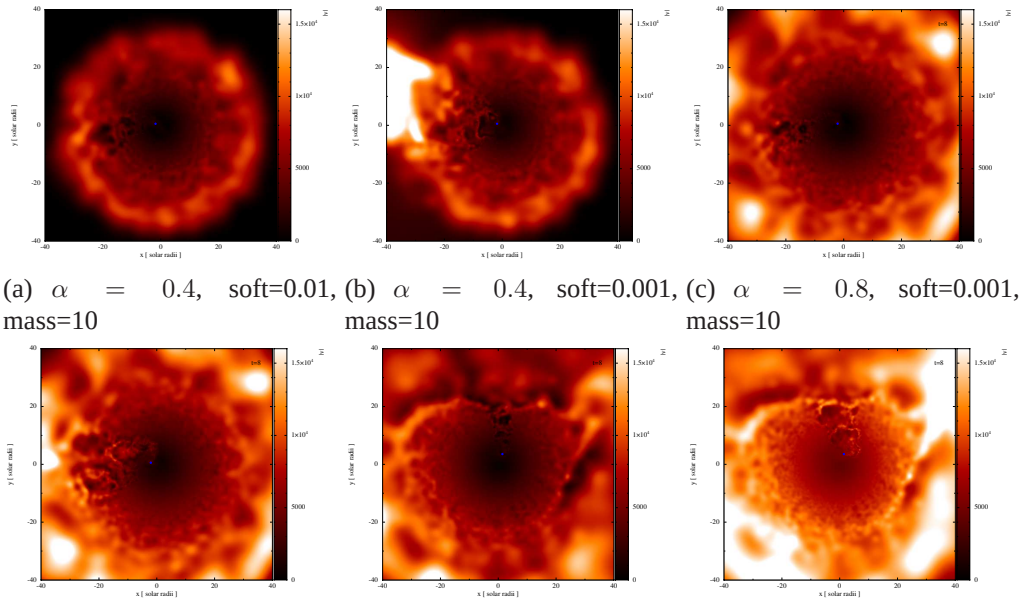

(a) $\alpha = 0.4$, soft=0.01, mass=10 (b) $\alpha = 0.4$, soft=0.001, mass=10 (c) $\alpha = 0.8$, soft=0.001, mass=10

(d) $\alpha = 0.8$, soft=0.001, mass=10 (e) $\alpha = 0.4$, soft=0.01, mass=7 (f) $\alpha = 0.4$, soft=0.001, mass=7

Figure 4.13: A small parameter study of companion influence on the ejecta, colour coded by velocity magnitude. The two columns have differing companion softenings - the left, 0.01 solar radii and the right 0.001 solar radii. The top row contains the results for a 10 solar mass companion, with a semi-major axis of 3 solar radii, with an α of 0.4. The middle row contains the same simulation with an α of 0.8, and the bottom row contains a simulation with a 7 solar mass companion again at 3 solar radii. Although the details of the disturbance vary, and in particular the softening appears to have some effect, all figures show notable distortion.

4.4.2 Secondary jet

Method

Using the same $7.7M_{\odot}$, $\approx 1R_{\odot}$ core radius model, we explore the effects of an asymmetric envelope around the core of the star at the moment of core-collapse. This is directly motivated by the ideas of Danail Obreschkow, my collaborator on this research. In zero-gravity water droplet experiments, a small off-centre cavity is induced within the droplet, and the resultant collapse can create a strong jet / weaker counter-jet system as seen in Figure 4.14 (Obreschkow et al. 2006). Having worked on this, Danail came across Cas A and immediately noticed the parallels.

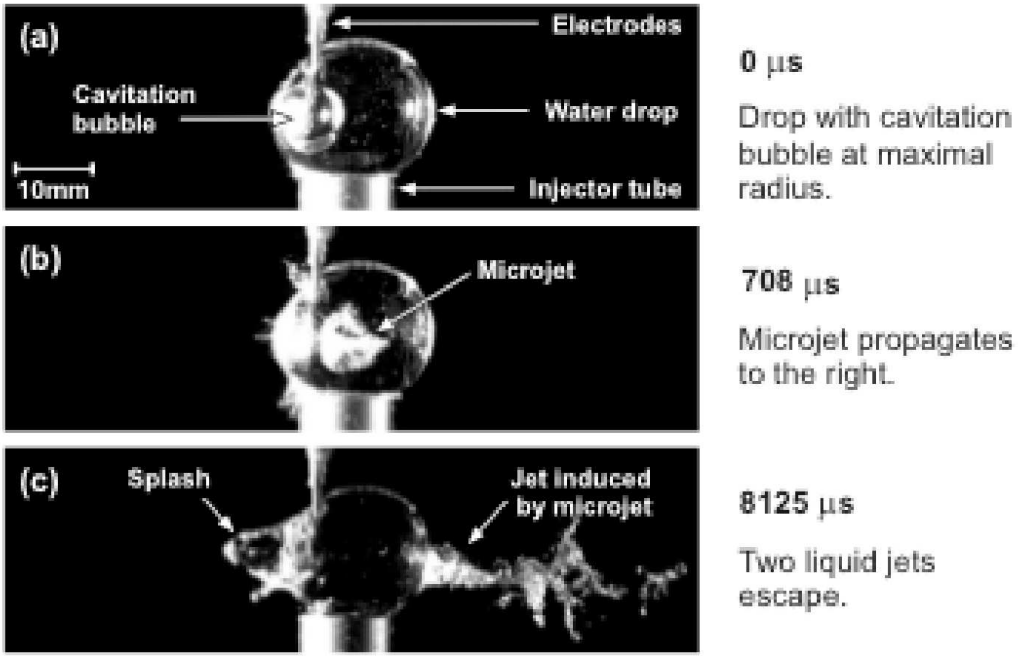

Figure 4.14: Double jet production in a water droplet in zero gravity from an aspherical cavity collapse (from Obreschkow et al. 2006). There are clear visual parallels between the third panel and Figure 4.1. Danail Obreschkow inferred a similar off-centre core-collapse might reproduce the NE/SW jet-counter-jet system in Cas A.

We induce a differential velocity between the core and the envelope, both to displace the core relative to the geometric centre of the envelope and to produce over

and under densities in a preferred direction. This produces a weak jet purely from the cavity collapse (Figure 4.15). Unlike the water droplet work, we do not find a strong double jet production from asymmetries around the core collapse cavity - instead we find strong single jet production, as seen in the results below (Figures 4.17 to 4.19). The physical similarities between the water drop experiment and the immediately pre-supernova star are limited; the communication between the extremely small scales in the core and the rest of the star is limited by their timescale differences, and the nearly incompressible equation of state for the water droplet leads to a direct immediate communication between the cavity and the surface through a column of fluid - substantially different coupling. The length scales of the core-collapse cavity and the rest of the star are also much more extreme.

The detailed physics and length/time scales in the actual core-collapse are extremely difficult to simulate, and assessing the likely effects of a velocity differential is slightly beyond the scope of this thesis - future work by Richard Booth may attempt this. Without modelling the cavity collapse and subsequent rebound itself, we note that a simple deposition of energy in this situation can also produce jets. We therefore concentrate mostly on this.

Results

In our test simulation, we impart a 1000 km/s kick to the inner 1.4 solar masses relative to the rest of the star. We let the core move noticeably off centre, and deposit a large fraction of the star's original binding energy into a few particles in the centre of the core. The subsequent shock is much stronger when it reaches the 'surface' of the star nearest to the core than in other areas, and ejects material at higher velocity. A schematic of this process can be seen in Figure 4.16.

In Figures 4.17 - 4.19 we show the effect of imparting a dramatic displacement to the core before explosion, which can produce an enhanced velocity asymmetry.

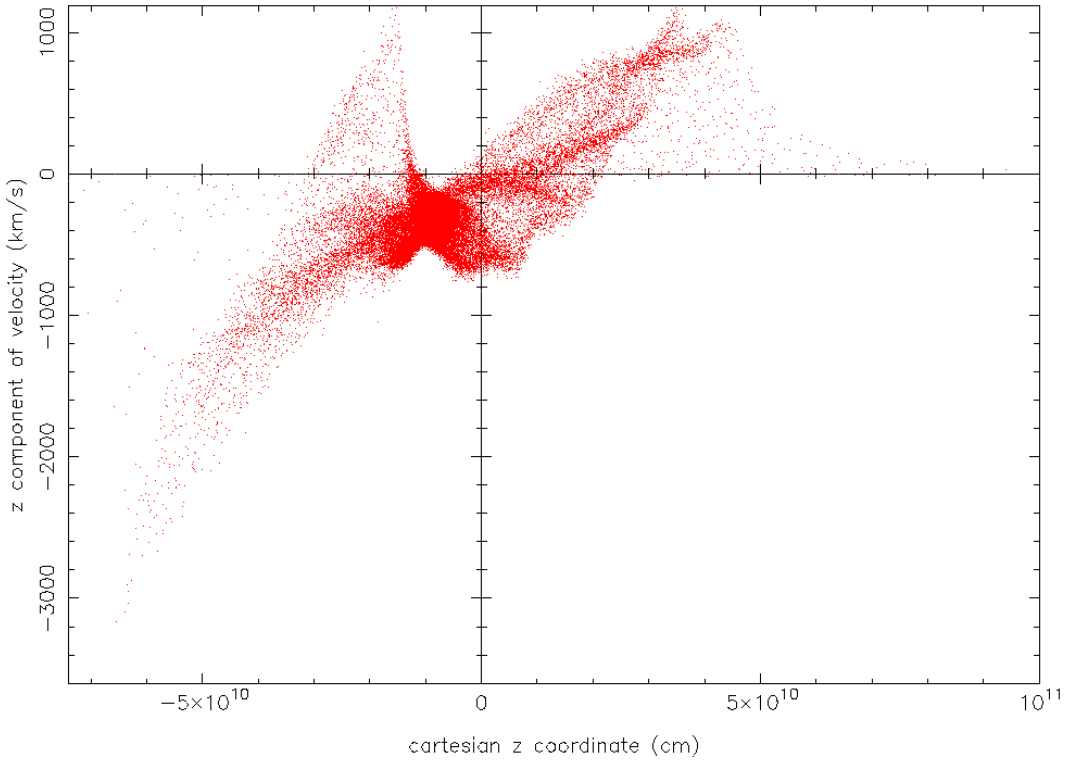

Figure 4.15: Cartesian z coordinate vs the z component of velocity at approximately half a dynamical time (200s) after the explosion. A jet is seen in the negative z direction.

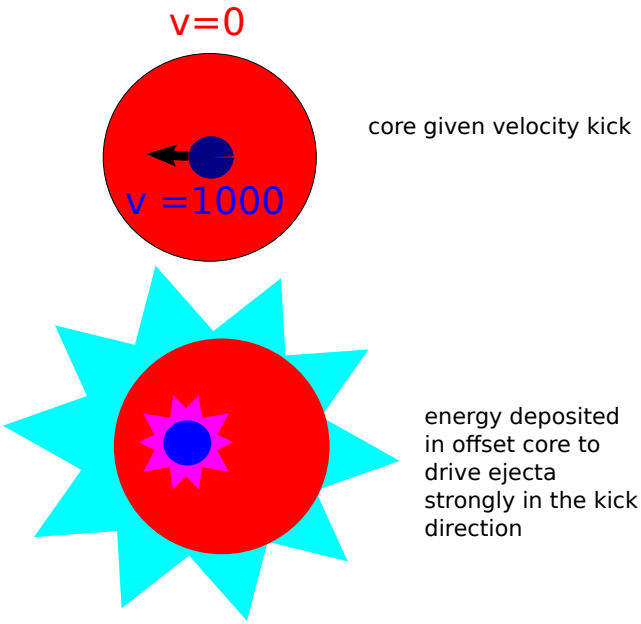

Figure 4.16: A schematic of the process for inducing our second jet. The core is given a velocity kick, then allowed to move off centre before energy is deposited. The ejecta will have a higher velocity in the direction the core has been offset.

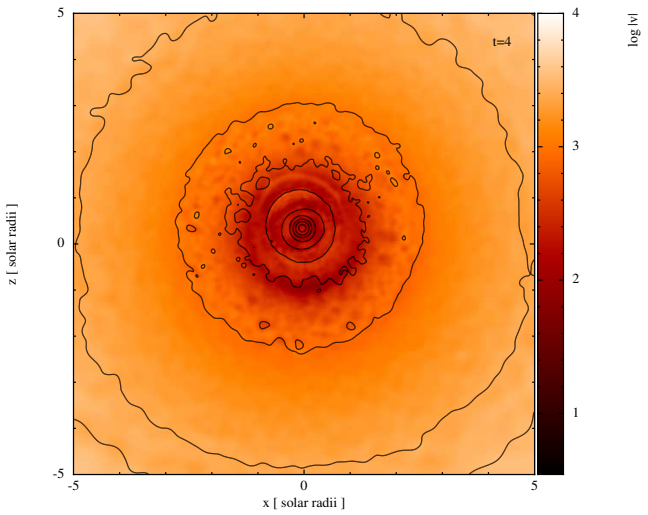

Figure 4.17: A cross section through the explosion at 8 dynamical times post-injection of energy, colour coded by the log of the velocity magnitude in cms^{-1} and contoured according to log density. The core was given a kick of $1000\mathrm{kms}^{-1}$ with a relatively weak α of 0.4.

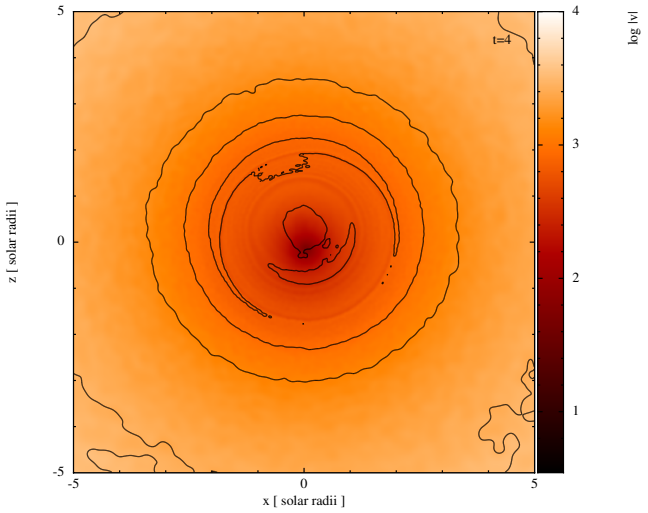

Figure 4.18: A cross section through the explosion at 8 dynamical times post-injection of energy, colour coded by the log of the velocity magnitude in cms^{-1} and contoured according to log density. The core was given a kick of $1000\mathrm{kms}^{-1}$ with an α of 0.8. There is a small asymmetry in outflow roughly along the z axis.

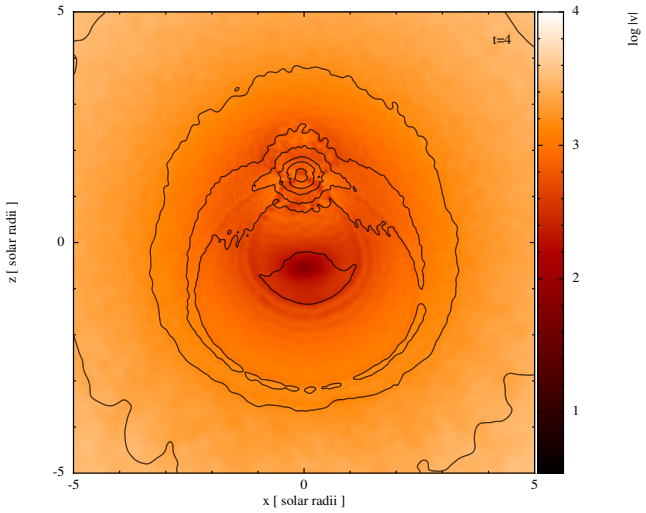

Figure 4.19: A cross section through the explosion at 8 dynamical times post-injection of energy, colour coded by the log of the velocity magnitude in cms^{-1} and contoured according to log density. The core was given a kick of $2000\mathrm{kms}^{-1}$ with a relatively strong α of 0.8. There is a substantial asymmetry in outflow along the z axis.

4.5 Discussion

While the models here are relatively simplistic, and are not specifically representative of core collapse processes, they demonstrate general mechanisms for the production of asymmetries such as those in Cas A. The distortion of the ejecta flowing past the companion should in theory be relatively universal, though in need of much more study and likely to vary in absolute effect. The tidal distortion will be much more dependent on the length-scales (such as the core size to semi major axis ratio) and mass ratios used, together with the stellar structure which should be much more strongly condensed in a realistic iron core progenitor, and less liable to tidal effects in the interior.

The variation of the primary jet with softening is an interesting issue, as the lowest gravitational softening used for the companion was 0.001 solar radii, less than white dwarf length-scales but considerably higher than neutron star or black hole length-scales - the two latter classes of object that it was intended to represent. In view of the average spatial resolution of the ejecta particles passing the companion, and the undesirability of artefact production, it is probably best for the purposes of this thesis to stop at this lower limit. Higher resolution simulations, localised to the region around the companion would help to shine a light on the processes and the dependence on parameters used.

4.6 Conclusion

While the two (classical) jets of Cas A have a roughly similar proper motion velocity of 14,500 and 13,500 kms^{-1} in the NW and SE jets respectively, we suggest they may have a separate, but connected, origin. A companion's influence could distort the passage of the supernova ejecta into a jet as it distorts the internal structure of the star to give a preferred direction for the ejected material. Although the jets produced in our simulations here are not particularly strong in velocity, the 'primary' jet mechanism certainly contains a additional, significant source of momentum in the companion to give the ejecta a relative velocity boost. The 'secondary' jet mechanism is a little more uncertain, and a little too undirected in our simulations. It has the most to gain from future work, and is perhaps the easiest to test. If the jets were

produced by these two mechanisms, primary (perhaps the NW jet) by explicit ejecta gravitational shaping, and secondary (perhaps the SE jet) by tidal distortion of the star, it produces a natural way to create a weakly preferred axis in the ejecta without having to resort to changes at the heart of the supernova itself.

This story also naturally explains a perpendicular kick to the remnant companion, as Philipp Podsiadlowski and Danail Obreschow suggest, to give a perpendicularly displaced X-ray point source. The companion's existence is strongly suggested by the mass-transfer hydrogen stripping of the core-collapse progenitor. The jets in our model are not particularly energetic, nor are they implicated in the processes of the supernova itself, and they do not create a toroidal pattern aligned along the line of sight, which has not been discovered. They would be, instead, the defining and lasting mark of the progenitor's binarity.

4.7 Future work

Future work is planned by a fellow student, Richard Booth, and will incorporate both jet models with realistic pre-supernova stellar models with more accurate treatment of the core collapse process, which is particularly relevant for any secondary jet production and affects the mass flow rate past the companion to influence the primary jet. He is already studying the first jet in a collisionless ballistic calculation. The two jets need to be tied together in a single simulation, and a wide parameter study needed with detailed chemical and kinematical predictions which can be checked against observations.

Chapter 5

Common envelope mergers and their ejecta

5.1 Introduction

Common envelopes were first invoked as a mechanism for explaining the very short periods of cataclysmic variables (CVs) - systems where a white dwarf accretes matter from a late main sequence star, leading to classical thermonuclear novae. The orbital period of these systems was found to be of the order of hours, implying an orbital separation far too small to be reconciled with ab initio binary star formation and the predicted white dwarf progenitor sizes. In addition, the large angular momentum loss needed to form such a system from standard binary formation assumptions remained a mystery. Comparisons with W Ursae Majoris systems, short period semi-detached common envelope binaries, led to the theory that the angular momentum and mass loss required to form CVs occurred in a common envelope phase of the system after Roche lobe overflow (Paczynski 1976, Ostriker 1975, Ritter 1976).

Roche lobe overflow occurs through the overspilling of one stellar atmosphere into the gravitational domain of the other star. This is reached when the atmosphere of one extends past the Roche radius:

$$r_l = \frac{0.49q^{\frac{2}{3}a}}{0.6q^{\frac{2}{3}} + log(1+q^{\frac{1}{3}}} \tag{5.1}$$

where q is the ratio of the masses of the binary stars $\frac{M_1}{M_2}$, and a the separation of the centres of mass of each star(Eggleton 1983).

If a system reaches a point where one star (the donor star) can overlow its Roche lobe and transfer mass to the other, a common envelope stage can still be avoided if the companion can accrete or expel the mass transferred efficiently (such as accretion onto a neutron star or other compact object - King and Begelman(1999)) or if co-rotation in the binary stars is established quickly (Taam and Sandquist 2000). In some systems with a mass ratio lower than a critical value (dependent on envelope response and other factors) dynamically stable mass transfer will lead to a widening of the binary (Hjellming and Webbink 1987). Additionally, the different responses of a radiative and a convective envelope to mass loss can affect the creation of a common envelope phase - the entropy gradient in a radiative envelope results in a reduction in size with mass loss (although a net shrinkage with respect to the Roche radius) whereas a convective envelope as in a post hydrogen core burning star can expand rapidly, forcing a dramatic runaway of the system into a common envelope phase.

When the transfer happens too quickly, or the atmosphere swells too rapidly, for the matter to be expelled or accreted, the envelope of the donor star engulfs the companion, forming a common envelope around the two. The gravitational wake of the companion, and the differential rotation or hydrodynamical drag of the envelope around the donor star core and companion transfers orbital angular momentum into spin-up of the envelope, which is eventually ejected through the deposition of a fraction of the binding energy of the orbits.

The common envelope pathway that we study here is described in Figure 5.1. The donor star (larger filled circle) evolves to a point where it transfers mass to the companion (smaller filled circle), which leads to a common envelope around both stellar cores. This envelope is spun up by the decay of the stellar core orbits, and the final exponential core orbital decay drives a shock through the envelope.

A large number of stellar systems are expected to pass through a common envelope stage, and the resulting complication in stellar evolution from accretion and pollution, orbit modification, mergers and untimely envelope loss is capable of reproducing many unusual observed stellar systems (e.g. Battacharya 1996, and see Taam and Sandquist 2000). In this report we are primarily interested in the mass

ejected from putative common envelopes in the final merger phase of the envelope.

Mass loss from common envelopes has been used in the context of bipolar planetary nebulae, usually in the form of supplying a dense equatorial enhancement to deflect winds along the polar directions (Morris 1981, Soker and Livio 1988). Morris and Podsiadlowski (2006) showed that the morphology of mass loss from orbital energy deposition in a common envelope is not necessarily confined to the orbital plane; ranges of envelope angular momenta and the proportion of orbital energy injected can produce ejecta in exclusively polar directions as well; this was used in the reproduction of the three-ringed SN 1987A nebula (Morris & Podsiadlowski 2007).

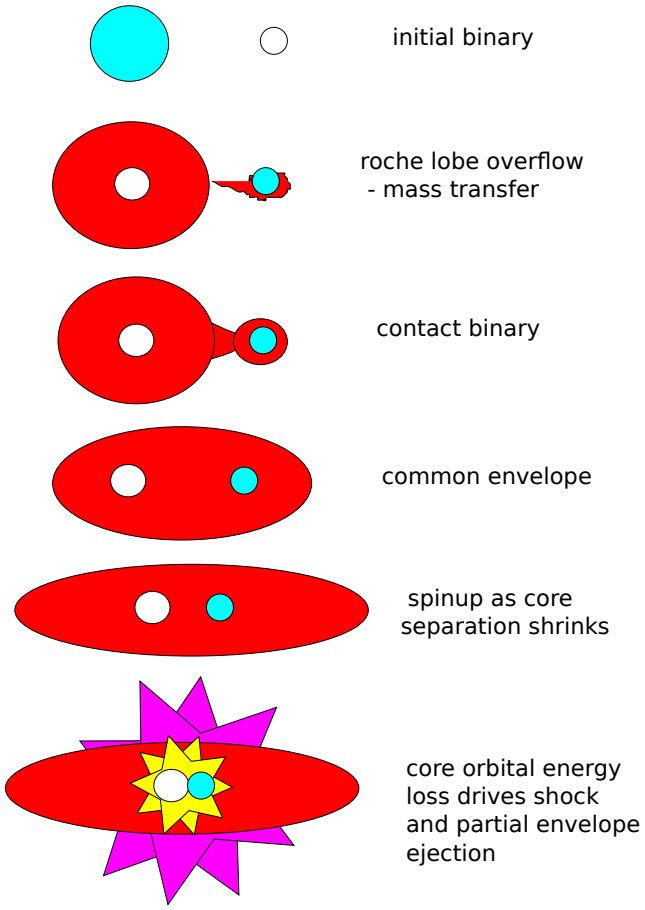

Figure 5.1: A schematic of one common envelope evolutionary pathway. One star in a binary system evolves, expands, and transfers mass to the other, inducing a common envelope phase which ends with a merged stellar core and some envelope ejection.

The work in this chapter is to further investigate the morphology of common envelope mass loss, with particular reference to bipolar nebulae. Optical transient surveys such as the Palomar Transient Factory and Skymapper will hopefully observe plentiful common envelope ejection events, such as the putative 'mergeburst' (Soker & Tylenda 2007) M85OT 2006-1 (Kulkarni et al. 2007).

Extracts from this work were presented in the APN5 planetary nebula conference, and were written into an accompanying conference paper (Fitzpatrick and Podsiadlowski 2010).

5.2 Method

We construct two polytropic models of a 50 solar mass, 30 solar radii star by numerically solving the Lane-Emden equation for values of n of 1.5 and 3, where n determines the pressure-density relation:

$$P = K\rho^{\frac{n+1}{n}} \tag{5.2}$$

and K is a constant. These values of the polytropic index n (1.5 and 3) were chosen to represent two different modes of stellar structure - roughly speaking, a convective envelope and a radiative envelope, respectively. The difference between the two envelopes in our simulations is a good indicator of the difference in behaviour between real stellar envelopes in these regimes. A polytropic index of $\mathrm{n} = 3$ is also a good fit for stars on the main sequence such as the Sun.

The profiles, once transferred into an SPH realisation, appear as in Figure 5.2. The low index (red,$n = 1.5$) has an almost flat density profile, whereas the high index has much higher contrast between the central regions and the outer envelope. An adiabatic index of $\gamma = \frac{5}{3}$ is used, except where noted in section 5.3.5.

Each envelope, or toy star, is designed to be a simulacrum of the common envelope process. In order to produce a general result across different stages of stellar evolution and different mass ranges, a point mass core for the donor star is not included - the simulations are pure envelope. Additionally, the companion that is engulfed by the common envelope is not explicitly modelled. This is for the reason that in order for the standard common envelope process to be valid, the stellar diam-

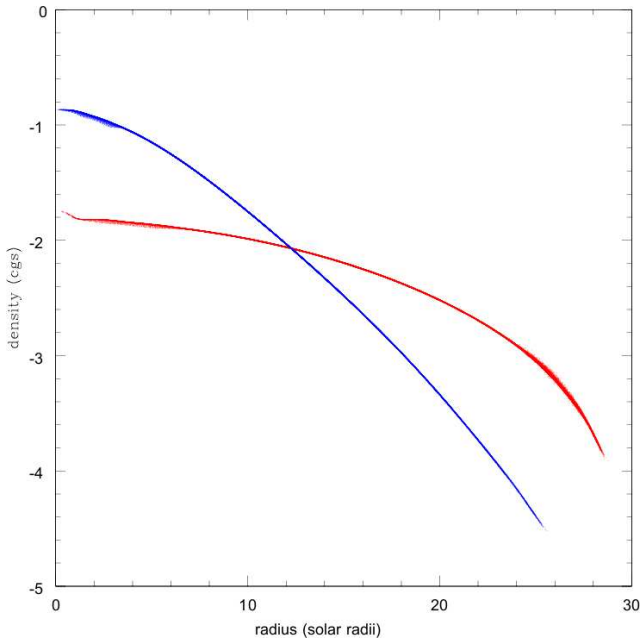

Figure 5.2: Density profiles of the two polytropic models as represented in the SPH relaxed initial conditions for a 50 solar mass, 30 solar radii star. The red profile has the index $n = 1.5$ and the blue has the index $n = 3$. The lower index model has much more mass in the outer regions, but much less in the core. The higher index is much more centrally concentrated. The profiles reach a critical density limit before the limiting radius of 30.

eter of the companion must be significantly smaller than the extent of the envelope. The influence of specific values for companion mass and radius is also a problem for producing general results.

The influence of the companion on our toy star is modelled by adding angular momentum to the envelope in a way that mimicks the effect of a spiralling in point mass. The final deposition of orbital energy by the companion and the putative donor core is treated as an instantaneous injection of thermal energy into an inner region of our toy star. Provided that the actual effects in a common envelope pathway of an inspiralling companion and the merging cores do not qualitatively differ from this regime, these assumptions will produce qualitatively valid results. They will not apply very well, for example, in situations with relatively large companion stellar diameters or mergers between main sequence stars with very similar masses and radii.

We add angular momentum on dynamical timescales to each model, roughly following the methodology of Morris & Podsiadlowski 2005. We add tangential velocity incrementally (using an interval of time between each addition which is small compared to the dynamical timescale of the star) reaching the highest angular momentum absorbable by the star after tens of dynamical timescales. We should note that in contrast to the standard methodology of Morris (PhD thesis) we increment the tangential velocity by $v_{t_{\rm new}} = v_{t_{\rm old}} + (\omega_{\rm new} - \omega_{\rm old}) r_{xy}$ instead of imposing a velocity field $v_{t_{\rm new}} = \omega_{\rm new} r_{xy}$ where $v_{t_{\rm new}}$ is the new value of a particles tangential velocity, ω is the angular velocity, and r_{xy} is the cylindrical radius where the cylindrical axis is the axis of rotation of the star. We stop the angular momentum addition when the particle achieves critical velocity - when a particle's centrifugal pseudo-force exceeds the gravitational force component in the plane of rotation.

At certain values of angular momentum in the models, we add varying energies $E_{\rm dep}$ to the core regions (by default in the central 5 solar radii) as follows:

$$u_i = u_i + \frac{E_{\rm dep}}{M_{\rm core}} \tag{5.3}$$

where$i$ is the particle index, u_i the specific internal energy of the particle and M_{core} the mass contained in the region. The standard region of deposition, of 5 solar radii radius (or 1/6 envelope initial radius, which is more appropriate), was chosen

as a rough boundary beyond which assumptions of point mass inspiral would not be appropriate.

The amount of energy to add is calculated by

$$E_{\rm dep} = \alpha E_{\rm bind} \tag{5.4}$$

where $E_{\rm bind}$ is the gravitational binding energy of the star at the time of energy addition, and α has $0 < \alpha < 1$.

The energy added is therefore model-dependent, and coupled partly to the momentum parameter.

5.3 Results

5.3.1 Density profiles after spinup

Solid body spinup of the envelopes gives the most angular momentum to the particles furthest from the axis of rotation. More importantly, it imparts the largest increase in tangential velocity, relative to their critical velocity, in these particles. As they begin in hydrostatic equilibrium, all particles experience an outward drift as their effective potentials reduce, due to the imbalance in the equatorial plane between the existing pressure force plus the centrifugal pseudo-force and the gravitational force on the particle. The envelope becomes increasingly oblate, and towards the equatorial plane the pressure gradient decreases adiabatically as the density profile is stretched. The gravitational force decreases as well, and these effects with the increased tangential velocity increment at increased radii allow the outer layers to expand increasingly rapidly until they reach critical velocity, whereupon they spiral outwards under the effect of expanding underlying non-critical layers, and the velocity shear forces from them. The pressure gradient profile and the degree to which the gravitational potential becomes disk or point-like with rotation affect the rate at which these outer layers evolve outwards.

Figure 5.3.1 shows the morphological evolution of the two polytropes during spinup, colour coded by the logarithm of the density. The $n = 1.5$ polytrope is much less centrally condensed, whereas the $n = 3$ polytrope is dominated by the gravitational influence of the inner regions. The particles furthest from the rotation axis in the $n = 3$ polytrope in effect break away from the main body once they become critical (see Figure 5.3.1 and form a new toroidal envelope dominated by small local differences in pressure forces, centrifugal force and the rotation axis-parallel components of the gravitational force. The $n = 1.5$ polytrope can absorb much more angular momentum with its greater mass at mid and large radii and the outer layers do not become critical as quickly.

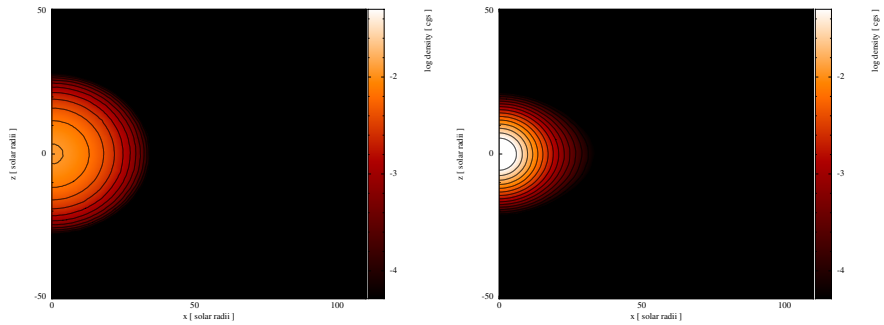

(a) n=1.5, low angular momentum (b) n=3, low angular momentum

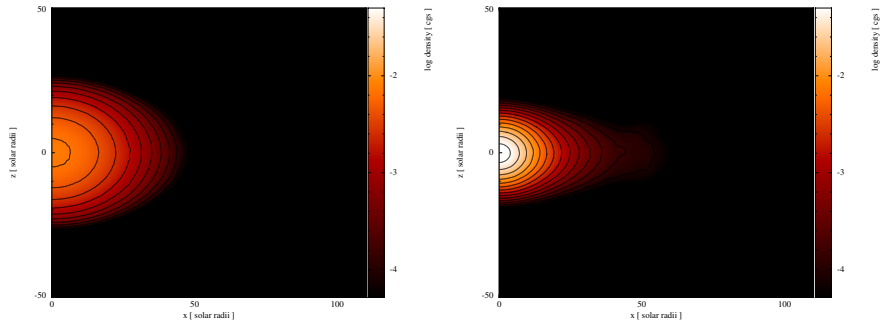

(c) n=1.5, mid angular momentum (d) n=3, mid angular momentum

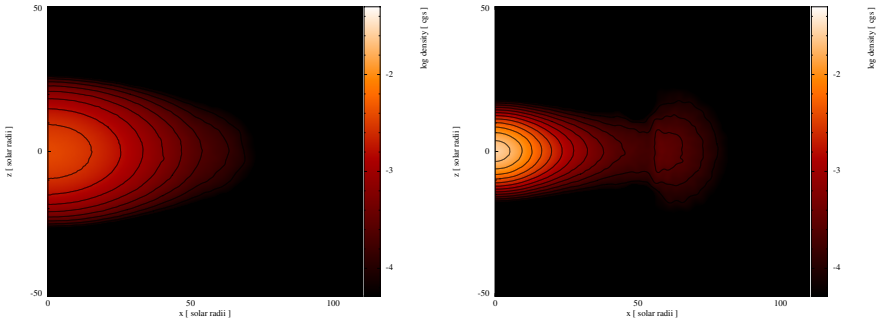

(e) n=1.5, high angular momentum (f) n=3, high angular momentum

Figure 5.3: Contour plots of cross-sections of the two polytropic models ($n = 1.5$ on the left, $n = 3$ on the right) during angular momentum addition highlighted by log density. The final value of angular momentum is approximately a third of the total angular momentum the models can absorb under these conditions. The lower index polytrope becomes increasingly ellipsoidal, but the higher index polytrope experiences breakaway particles forming into a toroidal pattern.

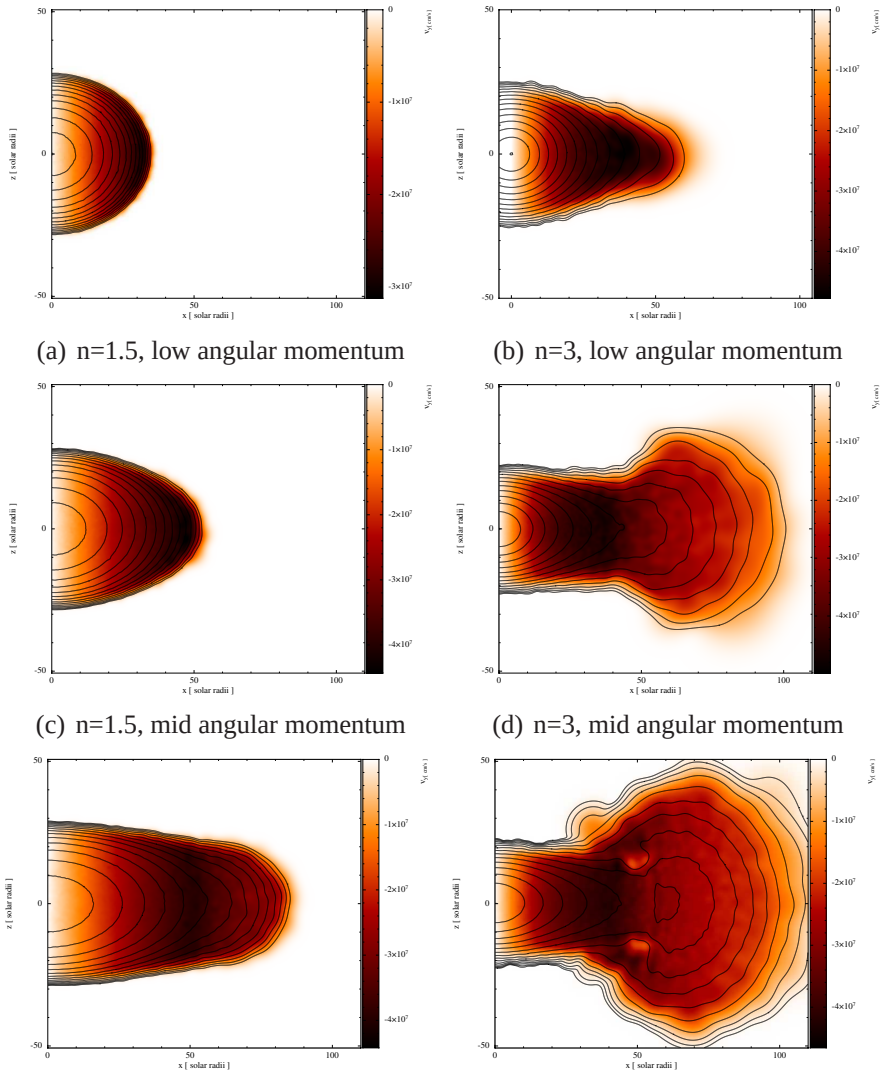

(a) n=1.5, low angular momentum

(b) n=3, low angular momentum

(c) n=1.5, mid angular momentum

(d) n=3, mid angular momentum

(e) n=1.5, high angular momentum

(f) n=3, high angular momentum

Figure 5.4: Contour plots (x-z cartesian) of cross-sections of the two polytropic models ($n = 1.5$ on the left, $n = 3$ on the right) during angular momentum addition highlighted by velocity in the cartesian y direction. The final value of angular momentum is approximately a third of the total angular momentum the models can absorb under these conditions. The higher polytropic index model has more critical particles at the same value of angular momentum.

5.3.2 Explosion evolution

Figures 5.3.2 to 5.3.2 show the evolution of the two envelopes after the deposition of a moderate amount of energy ($\alpha = 0.2$) after a typical angular momentum addition of $L = 6.0e54\mathrm{gcm}^2\mathrm{s}^{-1}$. The interface between the hot deposition region and the rest of the envelope gives rise to a shock which propagates approximately spherically outwards and reaches the polar regions first, while weakening by the time it reaches the outer extent of the envelope in the equatorial plane. The hot deposition region expands as a pressure-driven 'cavity' and subsequently launches lobe-like structures in both envelopes. However the toroidal envelope developed in the $n = 3$ model blocks and refocuses some of the ejecta into a bi-conical structure - to some extent this happens in the equatorial plane in the $n = 1.5$ model, where a slight focussing can be seen in the top row of Figure 5.3.2.

Figure 5.3.2 also shows a secondary ejection event caused by a dynamical 'slosh-back' of the inner regions, driven by the infall of material that was displaced by the cavity expansion and shock.

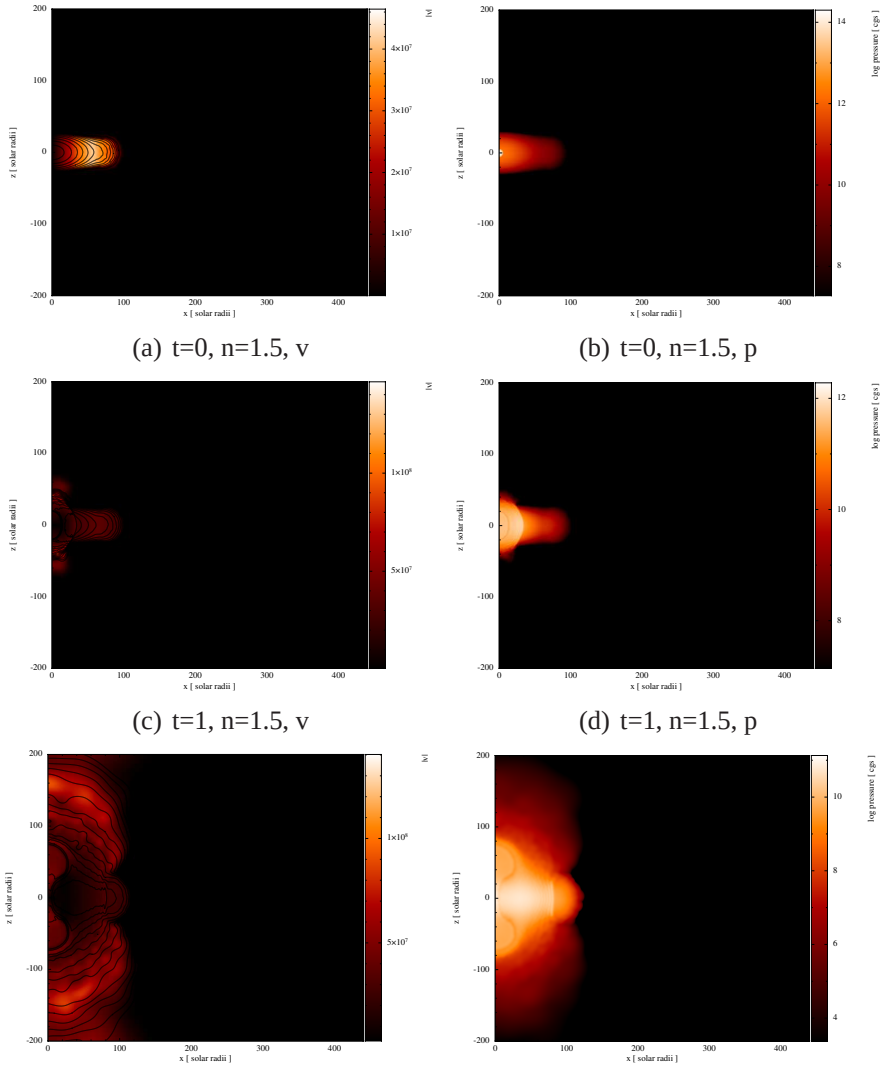

(a) t=0, n=1.5, v

(b) t=0, n=1.5, p

(c) t=1, n=1.5, v

(d) t=1, n=1.5, p

(e) t=4, n=1.5, v

(f) t=4, n=1.5, p

Figure 5.5: Cross section plots in cartesian x and z of the $n = 1.5$ model evolution after the deposition of energy, colour coded by velocity magnitude (left column) and the logarithm of the cgs pressure (right column). At early times, the deposition region gives rise to a hot under-dense, expanding region with a shock that generates initial bipolar loss and progresses in the equatorial plane.

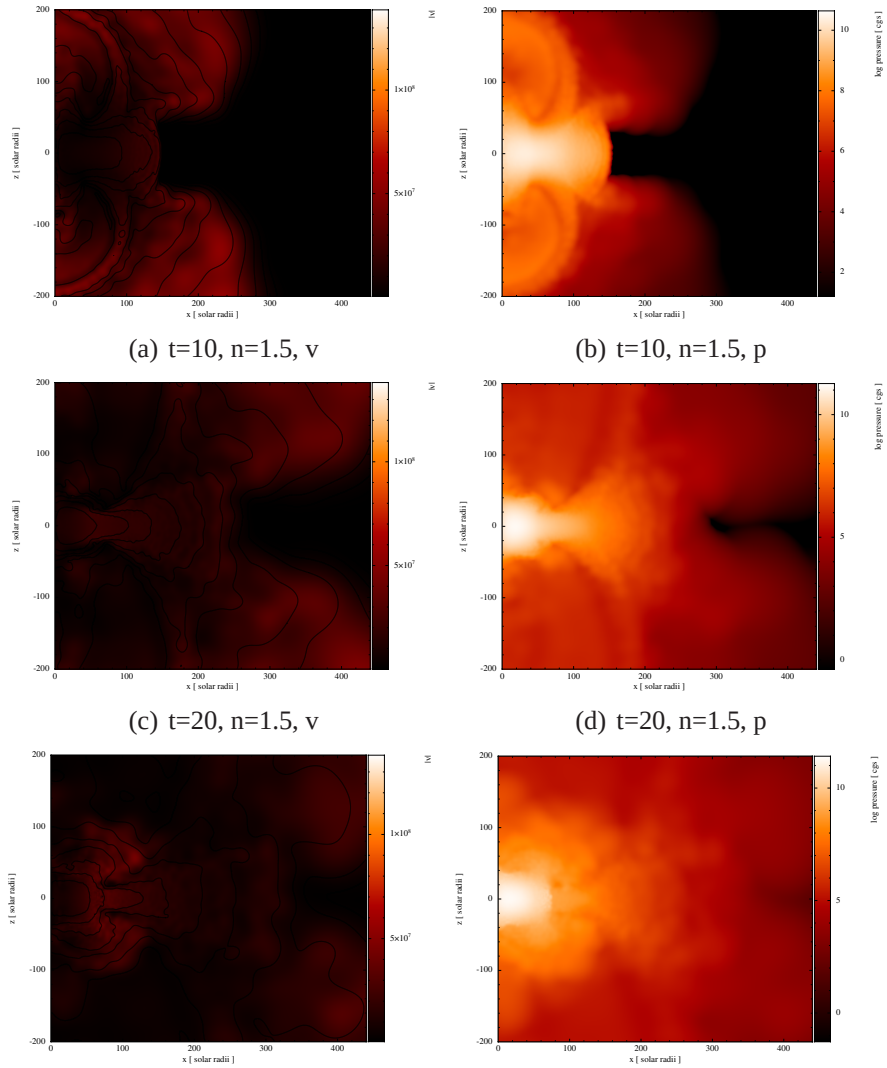

(a) t=10, n=1.5, v (b) t=10, n=1.5, p

(c) t=20, n=1.5, v (d) t=20, n=1.5, p

(e) t=30, n=1.5, v (f) t=30, n=1.5, p

Figure 5.6: Cross section plots in cartesian x and z of the $n = 1.5$ model evolution after the deposition of energy, colour coded by velocity magnitude (left column) and the logarithm of the cgs pressure (right column). This is a continuation of Figure 5.3.2. At later times, the weakened shock finally ejects some slower moving material in the equatorial plane, and a relatively violent implosion/explosion takes place in the 'core' as material infalls to eject more material.

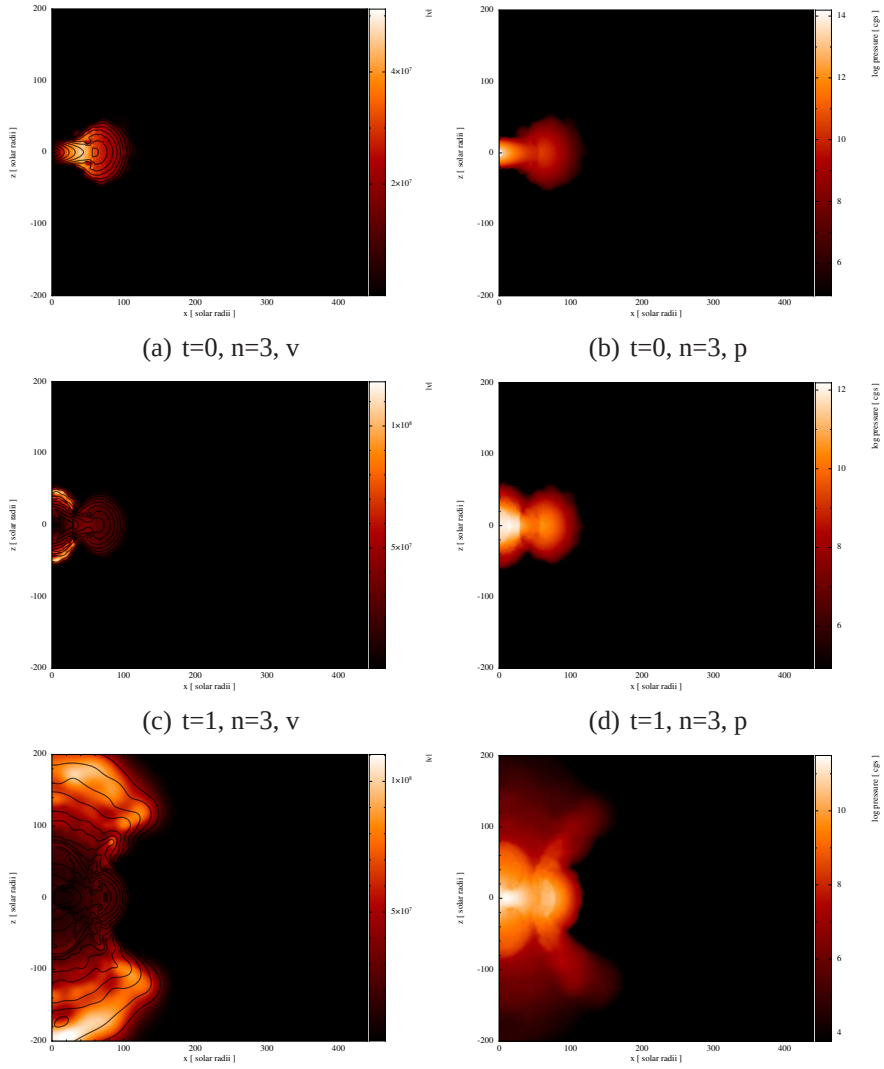

(a) t=0, n=3, v (b) t=0, n=3, p

(c) t=1, n=3, v (d) t=1, n=3, p

(e) t=4, n=3, v (f) t=4, n=3, p

Figure 5.7: Cross section plots in cartesian x and z of the $n = 3$ model evolution after the deposition of energy, colour coded by velocity magnitude (left column) and the logarithm of the cgs pressure (right column). At early times, the evolution is similar to the $n = 1.5$ model in Figure 5.3.2, but the interaction with the complex structures near the toroidal envelope gives rise to a bi-conical enhancement.

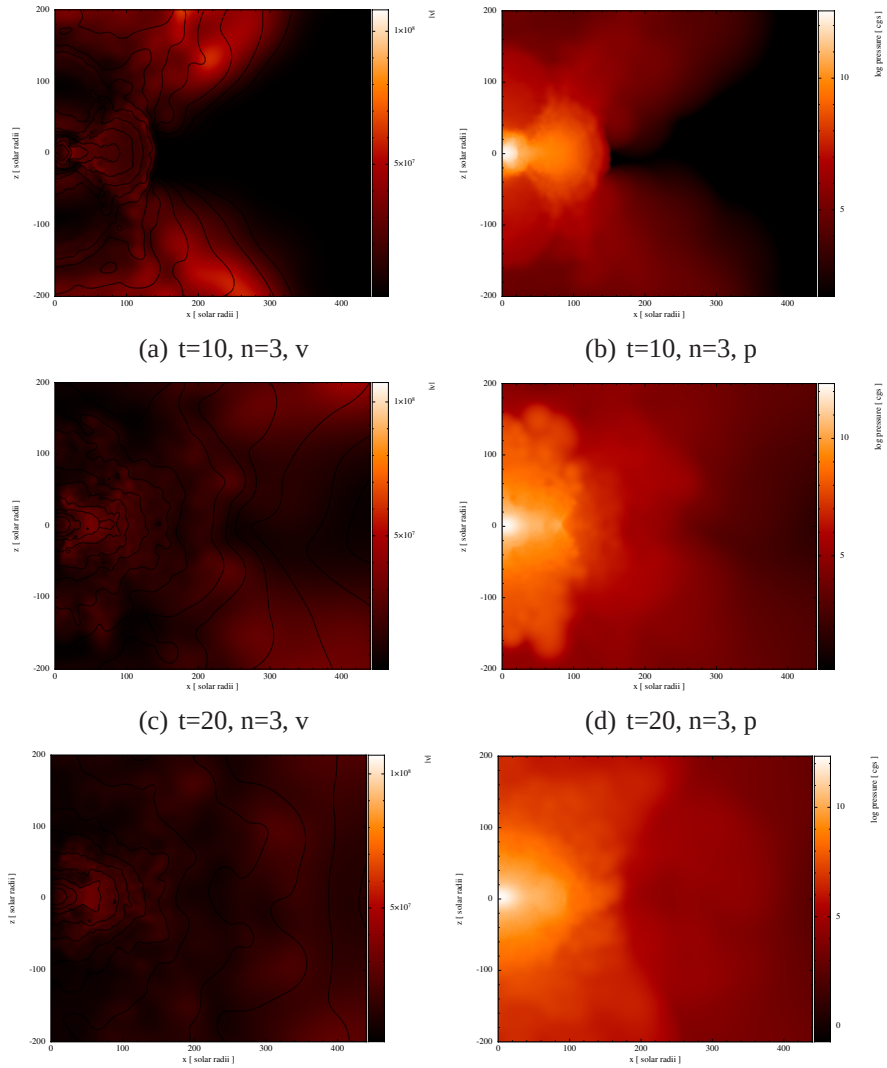

(a) t=10, n=3, v (b) t=10, n=3, p

(c) t=20, n=3, v (d) t=20, n=3, p

(e) t=30, n=3, v (f) t=30, n=3, p

Figure 5.8: Cross section plots in cartesian x and z of the $n = 3$ model evolution after the deposition of energy, colour coded by velocity magnitude (left column) and the logarithm of the cgs pressure (right column). This is a continuation of Figure 5.7. At later times, there is no dramatic secondary explosion, but the shock finally reaches the edge of the toroidal envelope and ejects a very small amount of material in the equatorial plane.

5.3.3 Energy, momentum and structure effects

We see the appearance of inner bipolar structures in some ejecta in Figure 5.9. These are not formed by the initial shock, but by the inflation of the hot gas in the deposition region causing a second mass loss event. The corresponding velocity field is shown in Figure 5.10, which broadly reflects the position map - where they are similar, this indicates a ballistic regime or 'Hubble' expansion of the relevant ejecta.

The bipolarity of the ejecta for lower deposition energies can be seen from Figure 5.11 which displays the mass distribution by altitudinal angle measured from the z-axis. As each bin in the histogram represents equal solid angle, it can be seen that while there is some mass loss near the equatorial plane, the greatest density of ejecta is at or above $\pi/4$ from the rotation axis (z-axis). Figure 5.11 demonstrates the higher momentum in these regions as well, which would be less suppressed than the slower moving equatorial ejecta by any circumstellar material, and thus enhance bipolarity.

Figures 5.9 to 5.11 have on the y-axis descending values of $\alpha = 0.1, 0.15, 0.2, 0.3$ and on the x-axis momentum left to right $L = 150, 200, 150, 200$. The left two columns are $n = 1.5$ models and the right two $n = 3.0$.

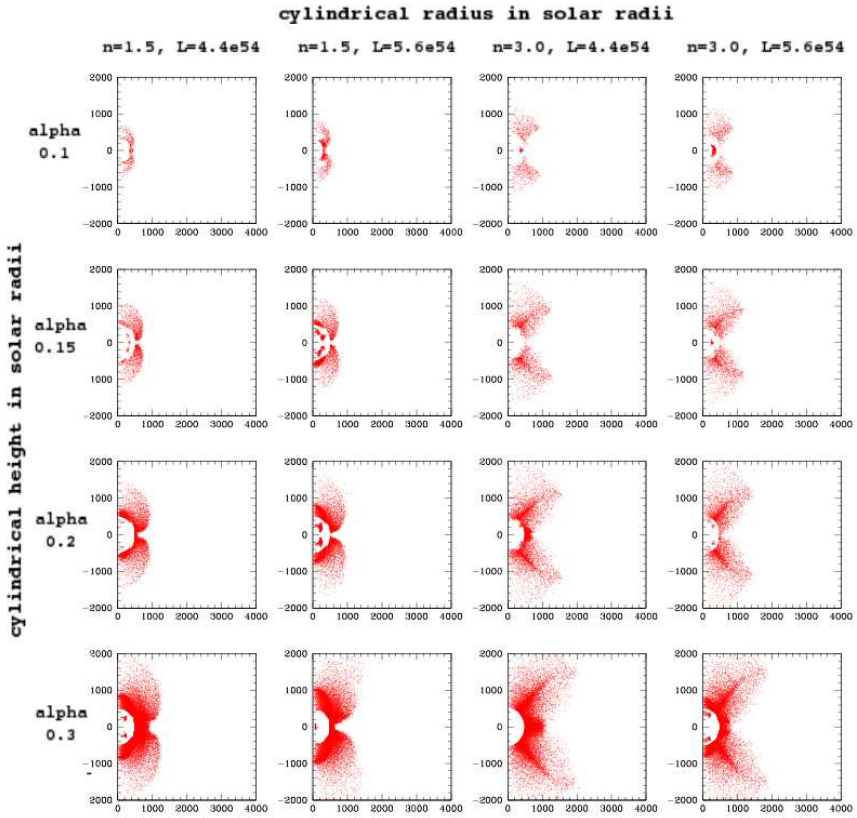

Figure 5.9: Particle position plots of unbound ejecta at late times $t \approx 40 t_{\rm dyn}$. Lower deposition energies produce slower moving ejecta, as expected, and there is a clear morphological difference between high and low polytropic indices.

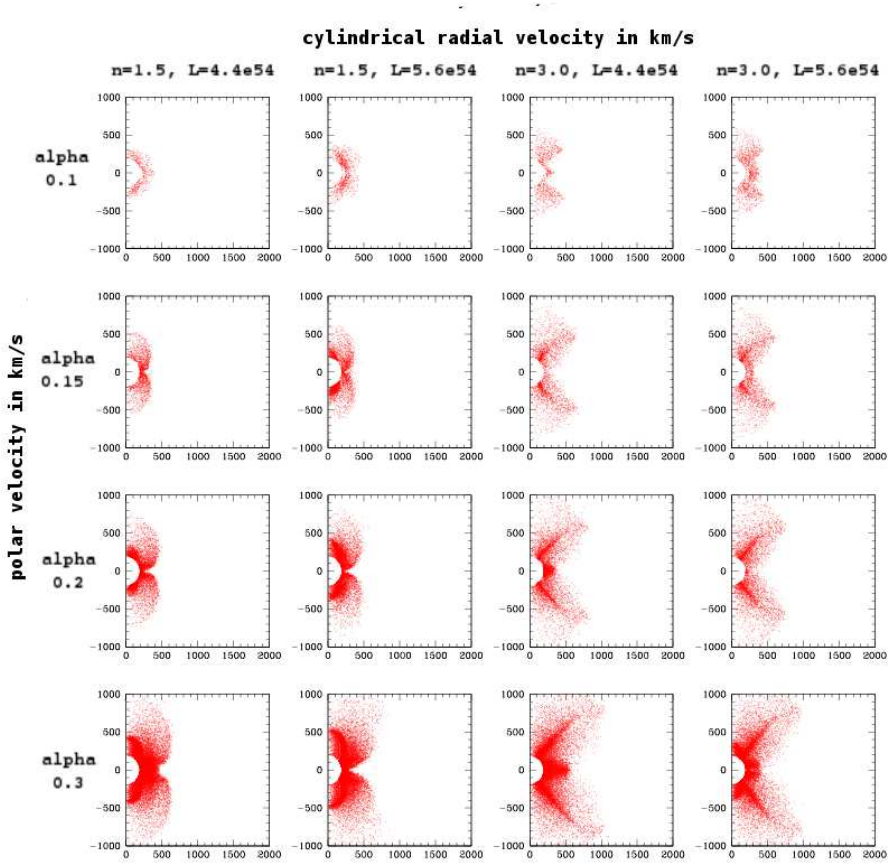

Figure 5.10: Particle velocity plots of unbound ejecta at late times $t \approx 40 t_{\rm dyn}$. The similarity to the position plots in Figure 5.9 is a test of how ballistic the ejecta is - differences in morphology between the two indicate a spread in time of the ejecta. Ejecta emitted at a single point in time will produce roughly identical plots.

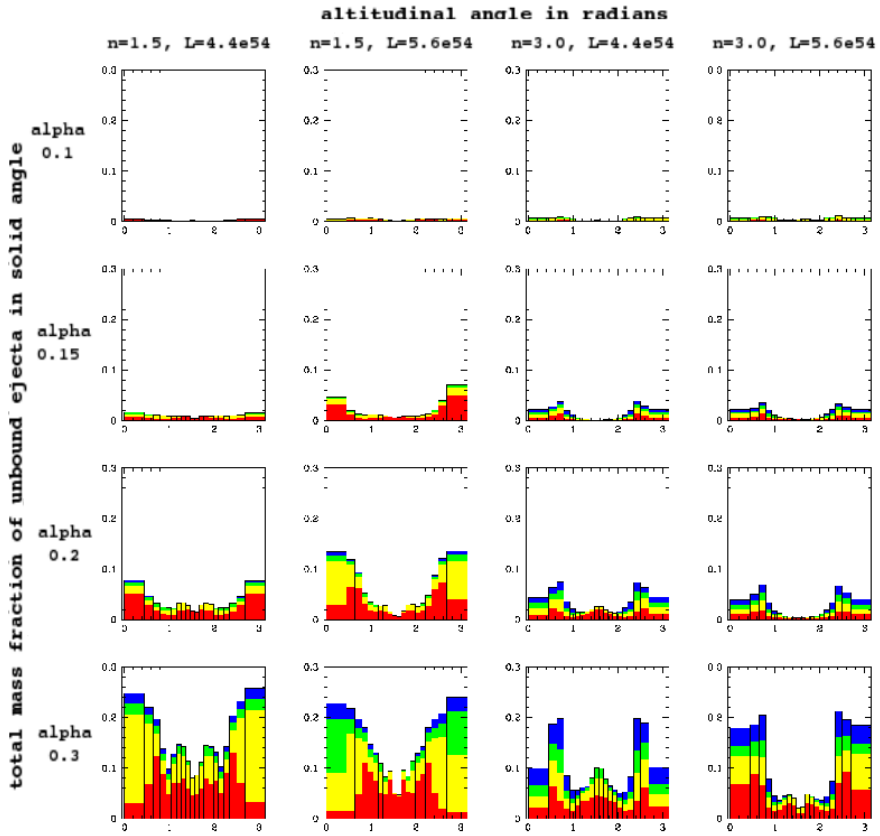

Figure 5.11: Histograms of mass per solid angle of unbound ejecta at late times $t \approx 40 t_{\rm dyn}$. The high index models can produce ejecta strongly peaked at $\frac{\pi}{4}$ from the poles. Velocities less than $300\,{\rm kms}^{-1}$ are in red, less than $450\,{\rm kms}^{-1}$ in yellow, less than $600\,{\rm kms}^{-1}$ in green, and more than $600\,{\rm kms}^{-1}$ in blue. Total amounts are in fraction of stellar mass.

5.3.4 Effects of energy deposition method

The relative size of the energy deposition region should be a major factor in determining the morphology of the ejecta, both in terms of strong shock production and in the inflation of a central hot cavity to produce lobes, as can be seen in the low index polytrope models above. We choose the deposition region to be $r_{dep} = 1.0$ solar radii, as it is substantially smaller than the volume encompassed by the standard $r_{dep} = 5.0$ and at these resolutions, after spinup of the star, contain of order an $N_{\rm ngb}$ neighbour number of particles, and therefore is something of a lower limit.

Figures 5.12 to 5.14 have on the y-axis descending values of angular momentum and on the x-axis, odd columns are original $r_{\rm dep} = 5.0$ and even columns are their $r_{dep} = 1.0$ equivalents. The left two columns are $n = 1.5$ models and the right two are for models with $n = 3$. The value of α is in all cases 0.2.

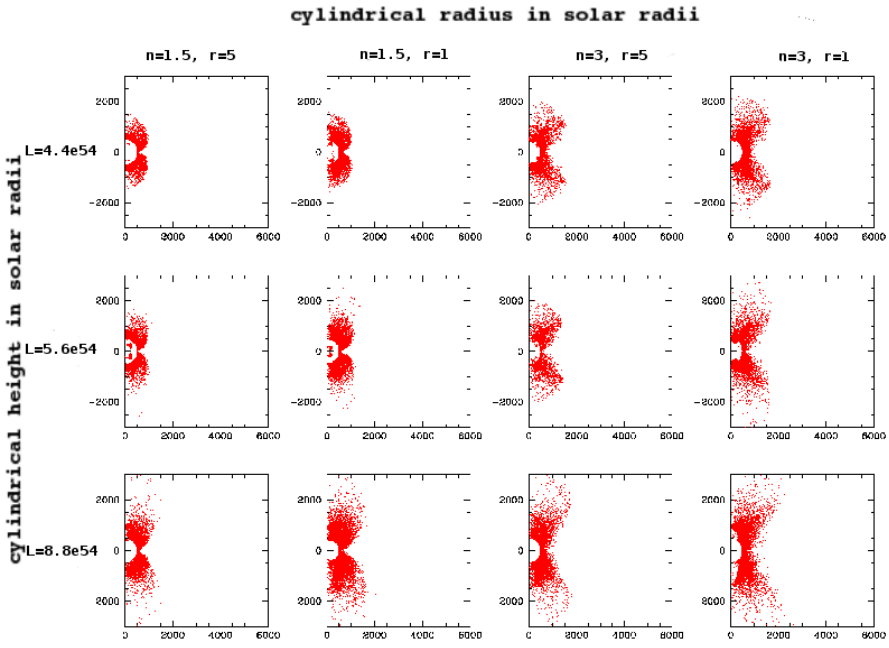

Figure 5.12: Particle position plots of unbound ejecta at late times $t \approx 40 t_{\rm dyn}$. Smaller deposition regions (first and third columns from the left) produce stronger shocks than the standard (second and last columns from the left).

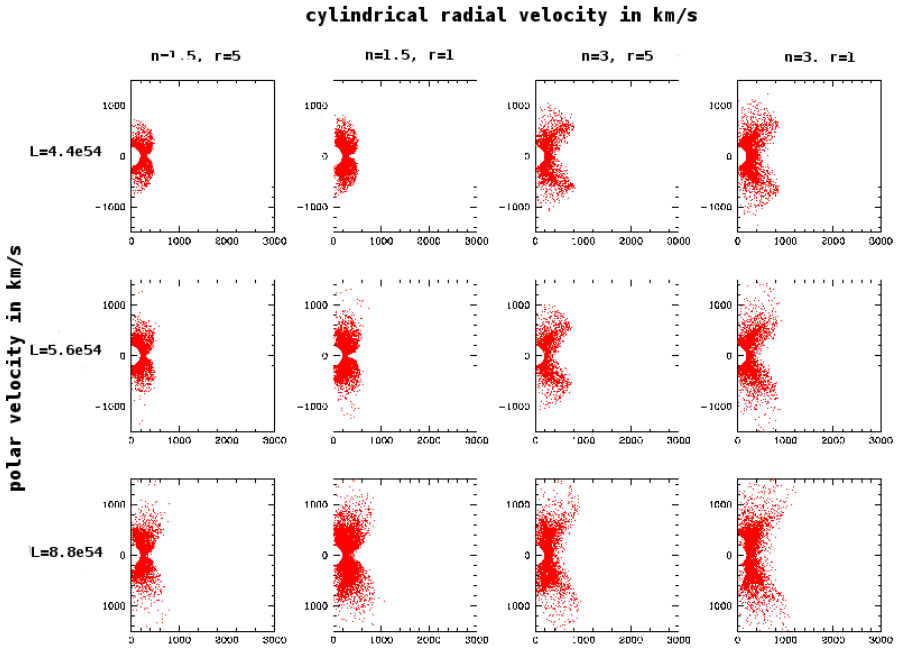

Figure 5.13: Particle velocity plots of unbound ejecta at late times $t \approx 40 t_{\rm dyn}$.

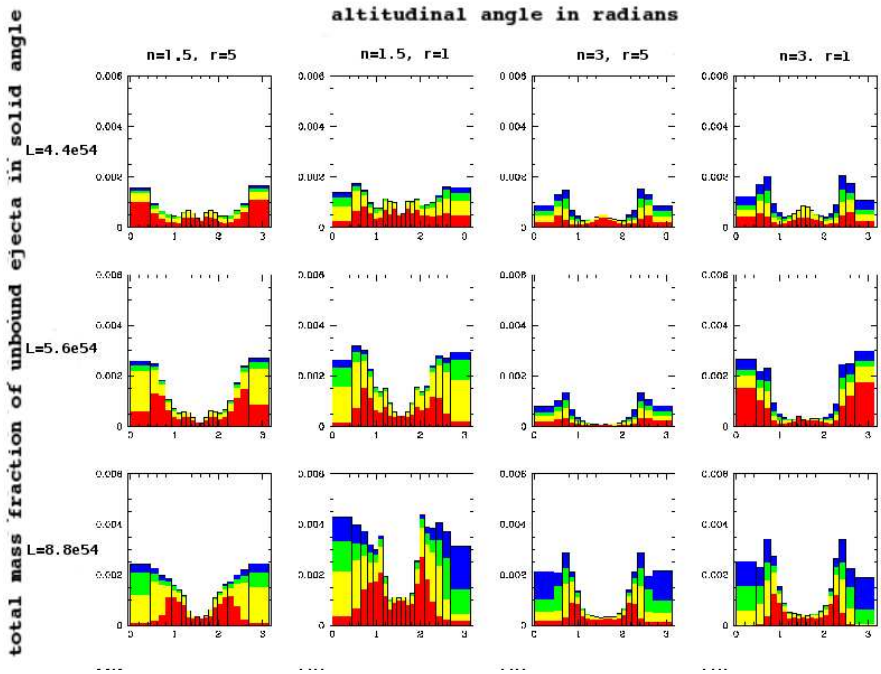

Figure 5.14: Velocity -coded histograms of mass per solid angle of unbound ejecta at late times $t \approx 40 t_{\rm dyn}$. Smaller radii (2nd and 4th columns) depositions increase the mass loss by driving a stronger shock, although still producing a bipolar flow. Some noise resulting from the small deposition region is noticeable.

While the size of the deposition region is undoubtedly a large factor in the strength of the generated shock, the geometry of the deposition is a strong factor - indeed it could be expected to be disk or ellipsoid shaped, as the companion spirals in in the equatorial plane. For envelopes where the deposition region can be reasonably approximated as a point, or at least where the shock from a flattened region becomes indistinguishable from a spherical region shock, this makes no real difference.

However, especially when considering relatively large deposition regions such as the 5 solar radii out of 30 standard in this chapter, it is worthwhile studying the effect of a flattened morphology deposition region.

In order to facilitate comparison with the 1 solar radii and the 5 solar radii cases, and to provide a strongly flattened geometry, the region is defined as an ellipsoid with minor axis of 2 and major axis of 10; it is the region where $\mathrm{x}^2+\mathrm{y}^2+(5\mathrm{z})^2 < \mathrm{r}^2$ where x,y,and z are the cartesian coordinates, with z parallel to the axis of rotation, and r as a constant of 5 solar radii. We apply the same energy increase formalism as before.

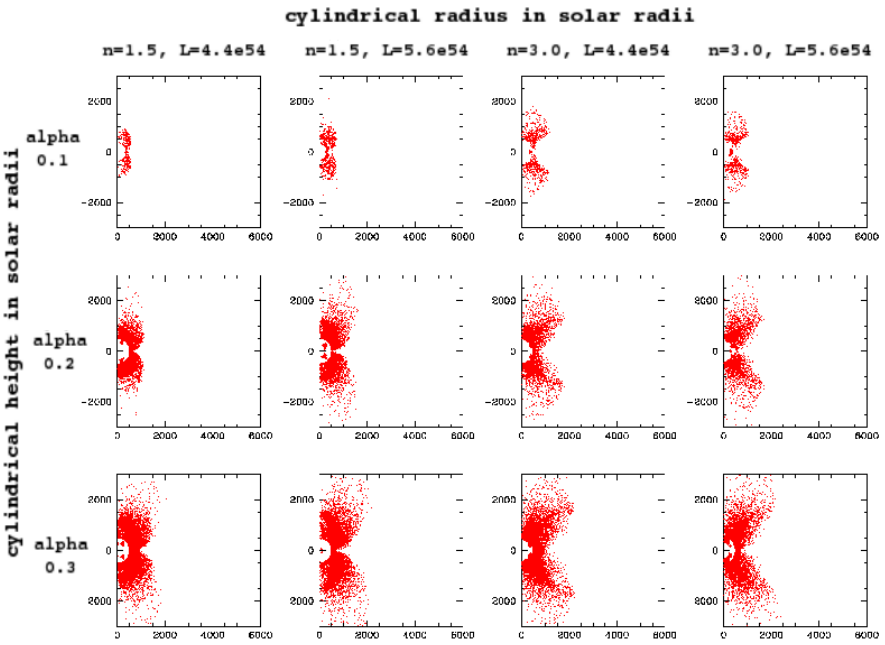

Figure 5.15: Particle position plots of unbound ejecta at late times $t \approx 40t_{\rm dyn}$ resulting from an ellipsoidal deposition of energy. The first two columns show an $n = 1.5$ model for (left column) $L = 150$ (code units), right column $L = 200$, with descending rows as $\alpha = 0.1, 0.2, 0.3$. To be compared with Figure 5.9 on page 126.

It is useful to compare these figures with those in subsection 5.3.3 - in particular it is apparent from Figures 5.9 and 5.15 that the qualitative difference between the $n = 1.5$ and the $n = 3$ polytrope models remains - polar lobes in the case of the lower index model, roughly bi-conical in the case of the higher index model. In particular, many of the inner structures (closer to the origin and within the lobes) are very similar. This is an interesting result, given that the structures should be highly sensitive to the size of the deposition region. However, the shapes in general are significantly larger in extent, implying much larger velocities as seen in Figures 5.10 and 5.16. The mass ejected is also larger, and the momentum output is significantly higher, as seen by a comparison between Figures 5.11 and 5.17. At lower energies ($\alpha = 0.1$) the distribution is significantly more bipolar for the $n = 1.5$ model; we should note the number of particles in each bin is still statistically significant at these

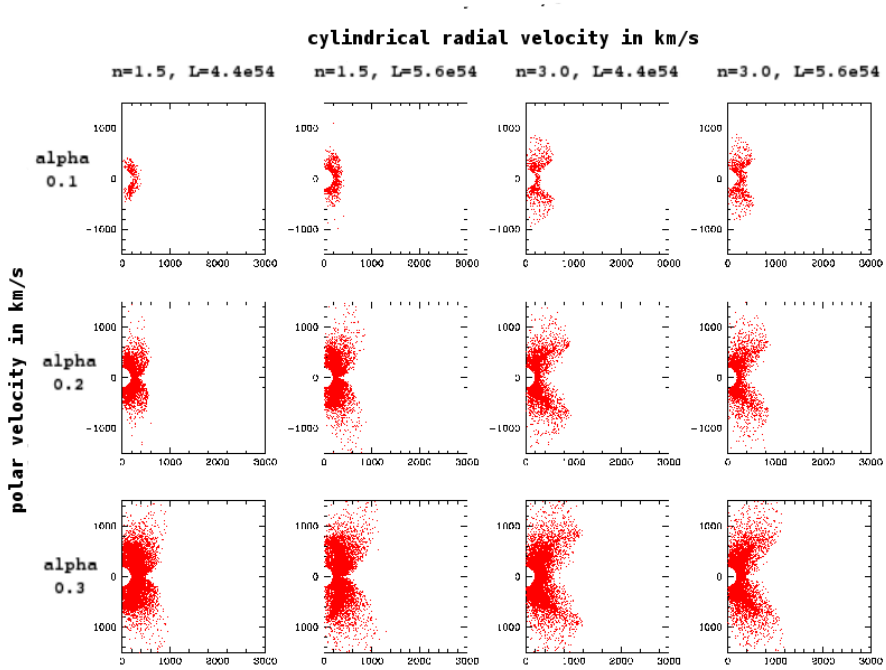

Figure 5.16: Particle velocity plots of unbound ejecta at late times $t \approx 40t_{\rm dyn}$ resulting from an ellipsoidal deposition of energy. Compare with Figure 5.10 on page 127.

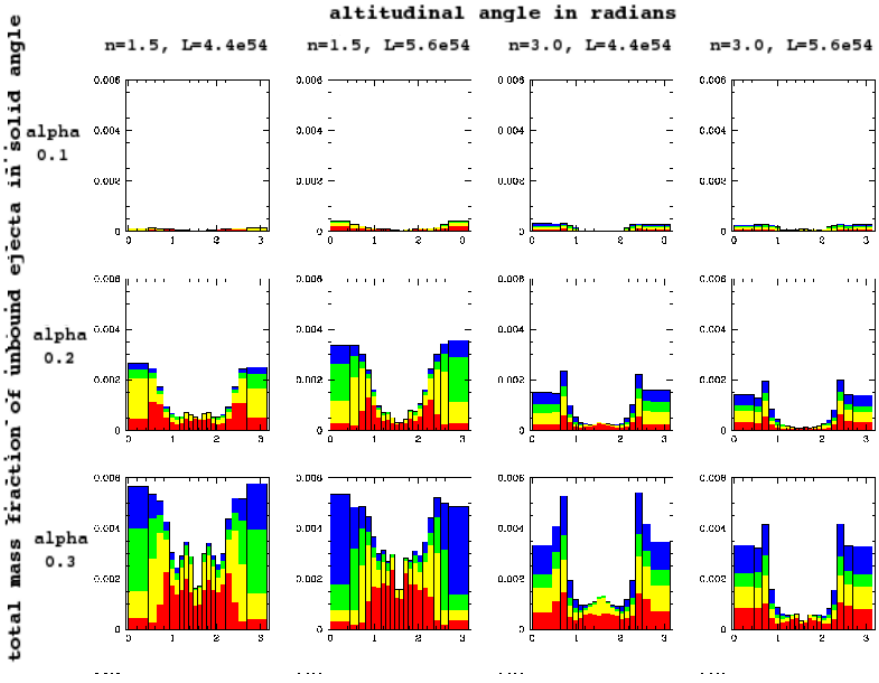

Figure 5.17: Histograms of mass per solid angle vs altitudinal angle of unbound ejecta from the above simulation at late times $t \approx 40\, t_{\rm dyn}$, colour coded by radial velocity. Velocities less than $300\,{\rm kms}^{-1}$ are in red, less than $450\,{\rm kms}^{-1}$ in yellow, less than $600\,{\rm kms}^{-1}$ in green, and more than $600\,{\rm kms}^{-1}$ in blue. Compare with page 128.

levels. The mass distribution is also slightly more bipolar in most cases, examining the bins between ≈ 1 and 2 radians versus the ≈ 0 to 1 and ≈ 2 to 3.14 bins. In all cases, the mass and velocity distribution is at least as bipolar as the standard cases, and much more than in the $r_{\rm dep} = 1$ solar radii cases. These features can be explained by the asymmetry of the driven shock - it should behave to zeroth order as strong as the $r_{\rm dep} = 1$ solar radii cases in the poleward direction, and as weak in the $r_{\rm dep} = 5$ solar radii case in the equatorial plane.

We find that ellipsoidal deposition regions, where they are of non-negligible size relative to the rest of the envelope, should also produce distinctively bipolar mass loss with sufficiently weak shocks (low $alpha$ or large deposition regions). We suggest that together with the $r_{\rm dep} = 1$ and the $r_{\rm dep} = 5$ spherical deposition region studies that this qualitatively covers the likely effects of varying size and morphology in deposition regions. Interestingly, if the deposition is somewhat staggered and a series of shocks propagates outwards, multiple inner structures may be formed, in a possible link with the many nested bipolar structures found in many bipolar planetary nebulae.

5.3.5 Adiabatic index effects

We use pressure-density relation of $P \propto \rho^{\gamma}$ where γ is $5/3$ as standard, which reflects a standard ideal monatomic gas, not dominated by radiation pressure. However, especially in higher mass stars, the envelope can be largely radiative, and an index of $\gamma = 4/3$ would be more appropriate. The change in index should also strongly affect the spinup density profiles in the equatorial plane, as the pressure drops more slowly with decreasing density. We found that a spinup on the same timescales as a $\gamma = 5/3$ simulation produced a substantial amount of nearly isotropic mass loss, rendering the comparison of deposition event produced ejecta nearly void. The results below were produced assuming the same spinup profile as standard, with only the explosion performed in a $\gamma = 4/3$ context, and are for illustration purposes.

The following results displayed in Figure 5.18 has on the y-axis descending values of angular momentum and on the x-axis the first column has $\gamma = \frac{5}{3}$ and the second column has the $\gamma = \frac{4}{3}$ equivalents. The value of α is in all cases 0.2.

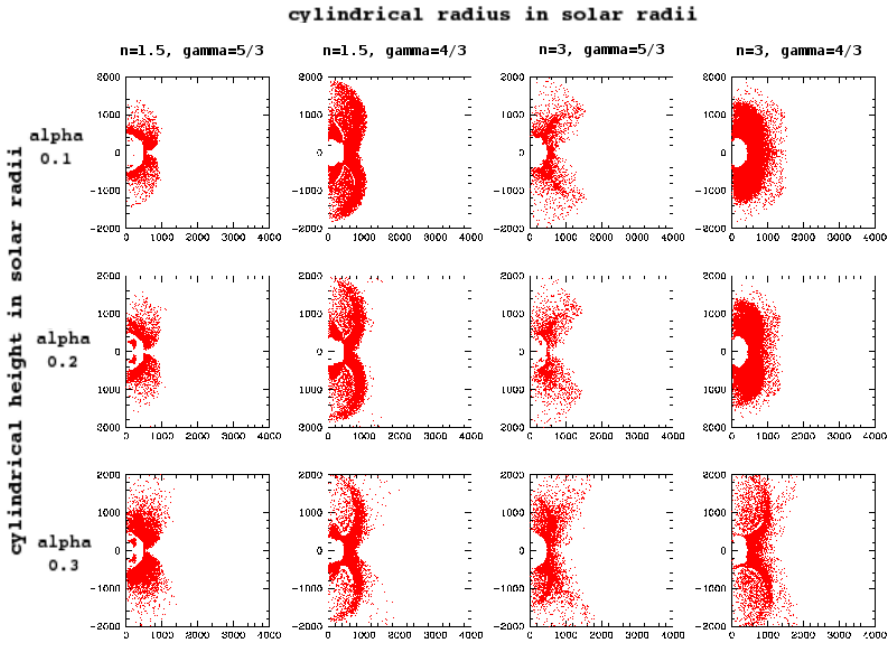

Figure 5.18: Particle position plots of unbound ejecta at late times $t \approx 40 t_{\rm dyn}$, from the standard set of simulations (1st and 3rd columns) and a $\gamma = 4/3$ set (2nd and 4th). Columns are in ascending order of angular momentum and with $\alpha = 0.2$.

5.3.6 Extremely low mass loss

The simulations presented so far have used ≈ 500000 equal mass particles to trace the envelopes. This allows reasonable resolution of shocks in the lower density parts of the envelope, but is not prohibitively high for the purposes of a parameter study. However as α decreases to low levels the number of particles in the ejecta becomes negligible (see, for example, Figure 5.9), and values below $\alpha = 0.1$ need a higher number of particles to resolve in three dimensions. Testing these low values would be a valuable experiment in studying conditions where the shocks are very weak, possibly from inefficient or non-instantaneous energy deposition. While objects such as Eta Carinae have lost $\approx 10 - 20\%$ of their mass to produce a visible nebula, smaller amounts from less massive stars may still produce planetary nebulae if the density of the ejecta is high enough, depending on the ionising source). Future work will use higher resolution models, with a factor of 10 higher number of particles, to model this.

5.3.7 Planetary Nebulae

The origins of planetary nebulae (PNe) that are bipolar are not well constrained; a single star losing mass on the AGB, in the absence of sufficient equatorially enhanced circumstellar material, cannot produce strongly bipolar mass loss without rapid rotation. This requires angular momentum addition, whether by tidal spinup from a companion or by a merger with a stellar or planetary companion (e.g. Soker 2003, Nordhaus (PhD thesis)). Significant mass loss from post-main sequence stars can also occur as part of a merger which leads to a common envelope phase, in which a relatively compact companion enters the envelope (Paczynski 1976, Ostriker 1975). Angular momentum is deposited in the envelope as the companion spirals in, and energy can be released thermally in a dynamically short timescale during the final fast spiral in / core merger phase.

We find that distinctly different envelope structures can produce bipolar ejecta under our methodology. Although the model is simplistic and makes no allowance for the gravitational and hydrodynamic influence of the spiralling-in secondary other than in angular momentum addition, it is a qualitative demonstration of the types of ejecta produced by reasonably weak shocks propagating into high angu-

lar momentum envelopes. The bipolarity of the ejecta under certain parameters in mass and momentum reinforces the role of common envelope processes as a possible cause of bipolar planetary nebulae. The differing morphology produced by varying envelope structures suggests that given a CE origin for a particular PNe, the envelope structure of the PNe progenitor could be deduced.

5.3.8 Population studies

As we deal with low deposition energies insufficient to unbind the envelope completely (although we do not have a core as a realistic remnant) our results apply to merged objects, not close binaries. If the envelope is unbound completely, the ejecta will tend to be strongly equatorially enhanced in mass, following the distribution of mass in the envelope. The polar loss should be faster, though, as the shock strength will decrease with distance from the origin. We therefore suggest that our simulations support an association of ejecta with strong mass loss along an axis, or strongly bi-conical mass loss could be associated with a proportion of merged stars, whereas no close binaries should have this by this mechanism- mass transfer causing jets, bipolar winds and magnetic fields may play their part in this. Unless another mechanism can eject material with similar timescales and energetics, this should be a very testable hypothesis.

Furthermore the differing ejecta morphologies produced by different mass distributions gives the opportunity to trace back the progenitor structure of many nebulae, once they are disentangled from the disturbances of magnetic fields and interacting winds.

5.3.9 Observability

We have chosen 50 solar mass, 30 solar radii envelopes for this study, which sets our absolute energy deposition amount, our dynamical timescales, and our photon diffusion time. The light curve produced by partial common envelope ejections in nature will depend heavily on mass, extent, density profile and the observer's polar angle of sight - the last two demonstrated in the above work. However, two immediate observable properties can be deduced - the energy released in our models is a substantial fraction of the star's binding energy (although substantially less than

pre-core-collapse core binding energy); for large red giant envelopes at least, the observed colour index should be red.

Good candidates for observed common envelope ejections are the luminous red novae or 'V838 Mon-like objects' , notably M85 OT 2006-1 (Kulkarni et al. 2007) and especially Nova Scorpii 2008, known as V1309 Sco. This class has energies in an intermediate range between the ranges of supernovae and the ranges of novae, with relatively cool spectra, and low ejecta expansion velocities by supernovae standards. In the case of V1309 Sco, Tylenda et al. (2011) showed that pre-existing observations proved that it had been a 1.4 day contact binary, with a decaying period and changing light curve immediately before the event. The post-burst morphology of the region was examined by Mason et al. (2010), who found what may have been an emissive polar region and absorbing equatorial torus. The pace with which new transients are being found in the modern day means that our simulations are eminently testable, not just post-event as in planetary nebulae, but actually in the moments of rapid spiral-in and merging.

5.4 Conclusion

Our simulations demonstrate a bipolarity in mass loss under the standard set of parameters: small deposition energies, and a medium to strong amount of angular momentum sufficient to produce significant distortion (at least a factor of 2 axis ratio). Increasing deposition energy will tend towards more spherically symmetric and ultimately equatorially enhanced mass loss. Differing initial density profiles in our simple models will produce differing features - across our simulations we have found a generally bi-conical product in the more centrally condensed $n = 3$, while the flatter profile $n = 1.5$ generally produces a polar-peaked double lobe structure. However, the differing adiabatic index models ($\gamma = 4/3$) seem to produce a large amount of premature mass loss during spin-up, suggesting that this would overwhelm an ejecta signal from a deposition event.

Future work will utilise the higher resolution model already produced (5 million particles for $n = 3$) and another for the $n = 1.5$ profile to update and ideally support these results. Equation of state effects and more realistic models (including cores) would also be important to investigate further.

Chapter 6

Eta Carinae

6.1 Introduction

Eta Carinae is a massive binary located in the Carina nebula, principally remarkable for the high inferred luminosity of the central star ($\approx 5 \times 10^6 L_\odot$ (Cox et al 1995, Hillier et al 2001) and the dramatic brightening and ejection of $> 12 M_\odot$ (Smith et al 2003) by the system in the 1840s-50s, now observed as a nebula surrounding and obscuring the central stars. The 'Great Eruption' causing the Homunculus nebula released a huge amount of energy ($\approx 10^{49.6-50.0}$ergs) into liberating this ejecta over a 20 year period (Smith et al. 2003). At its peak in 1841 Eta Carinae became the second brightest star after Sirius in the night sky, although more than 2,000 parsecs away. It attracted great attention for an event in the southern hemisphere (Frew 2004), and even became part of Aboriginal oral traditions (Hamacher & Frew 2010). Events such as these in stars like Eta Carinae are good candidates for relatively low-luminosity 'supernovae imposter' Type IIn SN (van Dyk 2005).

As one of the closest and easily observable massive stars in the Galaxy, Eta Carinae also offers insights into massive star formation and evolution. Understanding its single most defining and unique characteristic, the Homunculus nebula and the Great Eruption, can give us valuable clues to these outstanding issues and to the still unresolved nature of bipolar structures in astronomy.

Parameter	Value
Mass of primary	$120M_{\odot}$
Mass of secondary	$30M_{\odot}$
Orbital period	5.54 yrs
Eccentricity	0.9
Semi-major axis	16 AU
Periastron separation	1.6 AU

Table 6.1: Tabulated orbital parameters for the Eta Carinae system from Soker 2005

6.2 Eta Carinae A and B

Eta Carinae possesses a 5.54 year periodicity in radio (Duncan & White 2003) through to the X-ray band (Corcoran 2005) which has been inferred as the effects of an orbitally eccentric (0.9) binary companion (Daminelli 1996) with an identical period (eg Hillier et al 2006). In particular, the observed 70 day X-ray minima is associated with the binary companion going through periastron.

The parameters of the system can be recovered in most cases only through modelling the binary interaction from the observed multi-band light curve. Adopting the values from the compilation of literature model results by Soker (2005), parameters are listed below.

6.3 The Homunculus

The Homunculus nebula is an approximately axisymmetric bipolar nebula, with two large lobes and a 'ragged skirt' of material around the equatorial plane. These can be seen in Figure 6.1. The maximum extent of each lobe from the central stars is $\simeq$ 0.1 pc (Morse et al. 1998) ($3x10^{17}\mathrm{cm}$) and both contain the majority of the mass contained in the nebula of $>$ 12 $M_{\odot}$ (Smith et al. 2003) or as much as $\simeq$ 20 $M_{\odot}$ (Smith & Ferland 2006). Through spectroscopy, the lobes have been revealed to have a thin double shell structure, with [Fe II] emitting bulbs within a thin H_2 skin (Smith 2002). The expansion of the material, with a typical velocity of 650 km/s, and the thin-shelled structure of the lobes indicates a common origin in time coincident with the peak apparent luminosity of Eta Carinae in the 1840s-50s (Morse et al. 2001, Smith 2006). The same data indicates that the vast majority of

the nebula was ejected in a period spanning only 5 years.

Fast-moving outer ejecta ($> 2000\mathrm{kms}^{-1}$) can also be traced back to this event and are more filamentary in nature (Weis 2005), forming 'bullets' and 'strings' that are strong emitters in X-rays and contain very little dust. On a much smaller scale, the 'Lesser Eruption' in $\simeq$ 1887-1895 is thought to have produced the much smaller Little Homunculus (LH) (Ishibashi et al. 2003) which although significantly less massive and extended is similar in shape and axis. On the same scale is the infrared Butterfly structure, also nested in the Homunculus and hypothesised to have a common origin with the LH (Chesneau 2005).

The nebula as a whole is significantly depleted in C and O material (Verner, Bruhweiler & Gull 2005), and comparatively rich in helium and nitrogen (5 and 10 x solar abundances respectively), strongly indicative of CNO (carbon-nitrogen-oxygen cycle) processed material (Davidson et al. 1996, Smith et al. 2004).

The nebula features condensed structures close to the system, the Weigelt blobs (Weigelt & Ebersberger 1986). Proper motion studies with HST data have revealed potentially different temporal origins in the early 20th century (Dorland, Currie & Hajian 2004, Smith et al. 2004).

The Homunculus nebula surrounding Eta Carinae can be well described by an extremely energetic (although sub-supernova) prolonged expulsion of convectively mixed material from a massive star's envelope. The details of the expulsion and of the bipolar shaping of the ejecta are however uncertain.

6.4 Modelling the Homunculus

Early attempts to model the Homunculus followed from the ideas of Balick (1987), taking the theory of interacting stellar winds (ISW) from bipolar planetary nebulae and applying it to the similarly shaped Homunculus (Frank et al. 1995). In these models, a fast-moving stellar wind from the star or binary collides with a slower-moving pre-existing dense equatorial torus around the star, and is deflected towards higher latitudes. However the existence of an equatorial torus massive enough to deflect the outburst from Eta Carinae into polar lobes is not well established - the clumpy skirt of equatorial material is insufficiently dense or axisymmetric (Morse 1996). The apparent discovery of a $\simeq 15M_{\odot}$ torus around Eta Carinae (Morris et

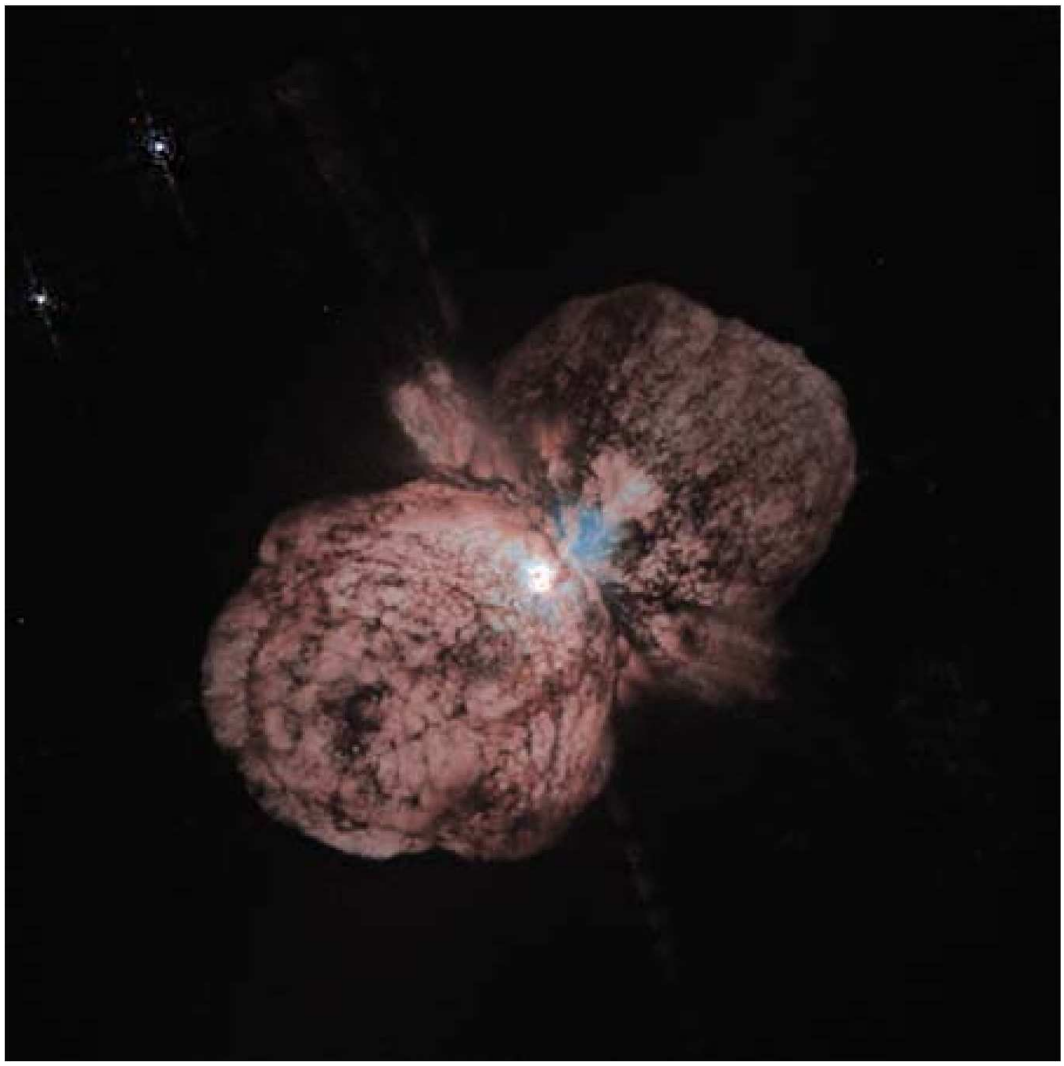

Figure 6.1: HST image of Eta Carinae (Jon Morse, NASA).

al. 1999) was later found to be lobe material (Smith et al. 2003).

Models have since studied the effects of asymmetric winds, such as Frank et al. (1998), motivated by theoretical models of the effects of gravity darkening (anisotropic distribution of surface gravity over the star) and rapid stellar rotation on stellar wind (Langer et al. 1999, Owocki et al. 1998, Maeder & Desjacques 2001, Dwarkades & Owocki 2002). While these enjoyed some success, the discovery by Smith et al. (2003) that the Homunculus was more massive than had been suspected and the mass loss rate in the Great Eruption was much larger (Smith 2006) (of order $1 M_{\odot} \mathrm{yr}^{-1}$) largely dampened conventional wind models.

A new approach came with the confirmation of Eta Carinae's binary companion (Damineli et al. 2000) in Soker (2001). Soker posited that following the ejection of a large amount of mass from the central star, the stagnation point between the primary and companion winds would occur within the Bondi-Hoyle accretion radius of the companion. A large fraction of the mass ejected (40 percent) would be accreted onto the companion and would form polar jets or collimated fast winds (CFW) to inflate the lobes and form a bipolar structure. While this has been expanded upon in (Soker 2005, 2007) problems remain with the choice of orbital and wind parameters for the system, and the mechanism proposed to inflate/eject the envelope.

Smith & Townsend (2006) successfully reproduced the equatorial skirt and lobes of the nebula by modelling an explosion normal to the surface of a rapidly rotating star followed by a parametrised radial force. It is not clear what physical mechanism could produce these phenomena, and angular momentum conservation seems to be violated (Soker 2004).

Indeed the outstanding problem in the modelling of the Homunculus, and in LBV (luminous blue variables, a phenomenological class of massive variable stars) giant eruptions in general, is the mechanism of ejecting the mass. The mass loss rate of Eta Carinae was approximately 10^{3-4} greater than a typical superwind, and yet continued on a timescale much greater than that of an explosion. Mechanisms have been proposed that invoke super-Eddington continuum-driven radiation pressure (Owocki et al. 2004, Belyanin 1999, Quinn & Paczynski 1985), extreme magnetic fields (Matt & Balick 2004, Soker 2007), ineffective convection driving density inversion (Arnett & Young 2005), and non-radial gravity mode oscillations in the core (Townsend & Macdonald 2006), but these invoke extremes of energy stor-

age or conversion over a timescale much less than the thermal (10^3 yrs) and much greater than the dynamical (10 days).

Ejection of the quantity of mass in the Homunculus over a period of years can be conventionally explained by common envelope ejection.

6.5 Binary companion and common envelope modelling

The binary companion of Eta Carinae is a massive, roughly 30 $M_\odot$ O star, with an orbital period of 5.5 years as deduced from the multi-wavelength periodicity of the central regions. In Soker's summarisation of the observational results (Soker 2005), the semi major axis of the orbit is around 16 AU, and the eccentricity extremely high, at about 0.9 (Note that there is still controversy over the exact values). This predicts a periastron of just 1.6 AU or around 320 solar radii, comparable to the radius of e.g. S Doradus, another blue hypergiant in the LMC, and certainly close or within the range of a spun up common envelope central system.

If Eta Car's Homunculus nebula originated in a common envelope ejection, we would assume that the most massive star was previously a close binary, with the surviving observed companion making a triple system, as described schematically in Figure 6.2. However, the orbit of the surviving companion, if it had similar orbital parameters, would pass extremely close to the close binary.

This close approach to the putative common envelope would almost certainly lead to mass ejection if the highly supersonic, high luminosity companion passes through it. This however would lead to a large velocity vector of the ejected material in the plane of rotation / orbit (assuming a common plane, which is not necessary to this conclusion). This anisotropy is not observed in the larger nebula, which does not preclude it being a smaller event. Critically, this interaction would lead to a slowing of the companion at periastron, which would act to decrease the eccentricity. Given the high eccentricity post-ejection, this is an argument against an extended common envelope phase. Tidal effects from close encounters with a common envelope would also act to decrease the eccentricity of the orbit.

If we assume that this disruption of the common envelope did not occur, the

Figure 6.2: A common envelope origin schematic for Eta Car. Before the Great Eruption that caused the Homunculus Nebula, the existing binary system may have been a triple. The putative inner binary pair may have merged to create the existing primary, and the mass outflow in the Homunculus Nebula.

periastron must have been further out in the past. This implies that the high eccentricity of the companion is partially a product of the mass loss event, corresponding to either time specific major mass loss from the interior (i.e. mass passing the orbit mostly near aphastron) or a braking in velocity near aphastron. The counterparts, a mass accretion or velocity increase near periastron, are less realistic.

It is important to note that an initially circular orbit is not required, and in fact a relatively high initial eccentricity could be obtained by a 3-body interaction during the birth of the system, leaving the lightest (the 'secondary') in an eccentric, distant orbit with the two heavier components relatively near to each other. The star that would become the primary would therefore have a more equal mass ratio than that of the primary / 'secondary' today.

Soker(2006) posited that a magnetically-driven inflation of the primary's radiative zone to 20 AU radius led to a Roche lobe overflow / slow wind accretion onto the secondary - mass loss is supposed to be drastically enhanced when the companion is outside the envelope, leading to the observed eccentricity.

The differences between an inflated slow rotating single star in Soker 2006 and a spun-up common envelope would become apparent in the drag terms and angular momentum transfer in the secondary's orbital evolution. Whether the Homunculus Nebula could be a result of common envelope accretion onto the secondary (tertiary at the time) rather than a secondary-influenced common envelope partial ejection can theoretically be distinguished by the morphology of the ejecta, the orbital parameters of the secondary and the rotation of the primary.

There are notable problems with modelling the Homunculus nebula as a common-envelope derived phenomenon, including accounting for the high eccentricity of the companion, possible pre-Great Eruption outflows (Bohigas et al. 2000), the Little Eruption 40 years afterwards, and the problem of modelling such high-mass progenitor stars. Nevertheless, common envelope ejection is one of the few plausible physical mechanisms for the scale of mass loss and axisymmetry of the Great Eruption. Common envelope ejection leads to a significant amount of mass loss in a high angular momentum, morphologically distorted environment - this distortion of the envelope can produce almost purely high-latitude or polar mass loss under the correct circumstances (Morris and Podsiadlowski 2005). If common envelope ejection is the correct mechanism, the problems above simply become valuable constraints on the process leading to the Homunculus nebula.

The first step in checking the plausibility of the Great Eruption as a common envelope related event is therefore to model the orbital evolution of the companion star under varying mass loss profiles and ejecta velocities. Morris (DPhil thesis) suggests that an asymmetry in the mass loss from a common envelope could further

increase the eccentricity of the companion.

6.6 Testing the triple hypothesis

One problem is the proximity of the (existing) binary companion to the proposed inner merging system. Using criteria from the literature (Mardling and Aarseth 1999), and assuming co-planarity, we can produce constraints on the inner binary system.

The closest allowed approach of the outermost star to the inner binary R_p^{crit} was given in Mardling and Aarseth (1999) (reproduced here from Saleh and Rossio 2009) as:

$$R_p^{crit} = 2.8(\frac{(1+q_{out})(1+e_{out})}{(1-e_{out})^{1/2}})^{0.4} a_{in} \tag{6.1}$$

where q_{out} is the mass ratio of the outermost star (mass $m3$) to the inner binary (masses $m1$ and $m2$) $\frac{m3}{m1+m2}$, a_{in} the inner binary semimajor axis, and e_out the outermost star orbital eccentricity.

Figure 6.3 seems to rule out a binary system of total 100 solar masses on the main sequence if the companion eccentricity was/is 0.9, and for a reasonable range of companion masses. However an eccentricity of 0.8 more than doubles the allowed semi major axis, as seen in Figure 6.4. An accurate value for the companion eccentricity would be a very useful test of the validity of the model.

6.7 Method

As in the generalised CE ejecta simulations in the above chapter, angular momentum is slowly added as solid body rotation to SPH particles representing a 50 solar mass, 50 solar radii star. If a particle reaches its critical rotation velocity, it is no longer spun up. This represents the decoupling of the outer, differentially rotating envelope and roughly solid body rotation of the inner regions where the merger is happening. After a predetermined amount of angular momentum is added, a substantial fraction of the star's binding energy is injected in the core. This follows work by Morris and Podsiadlowski(2006).

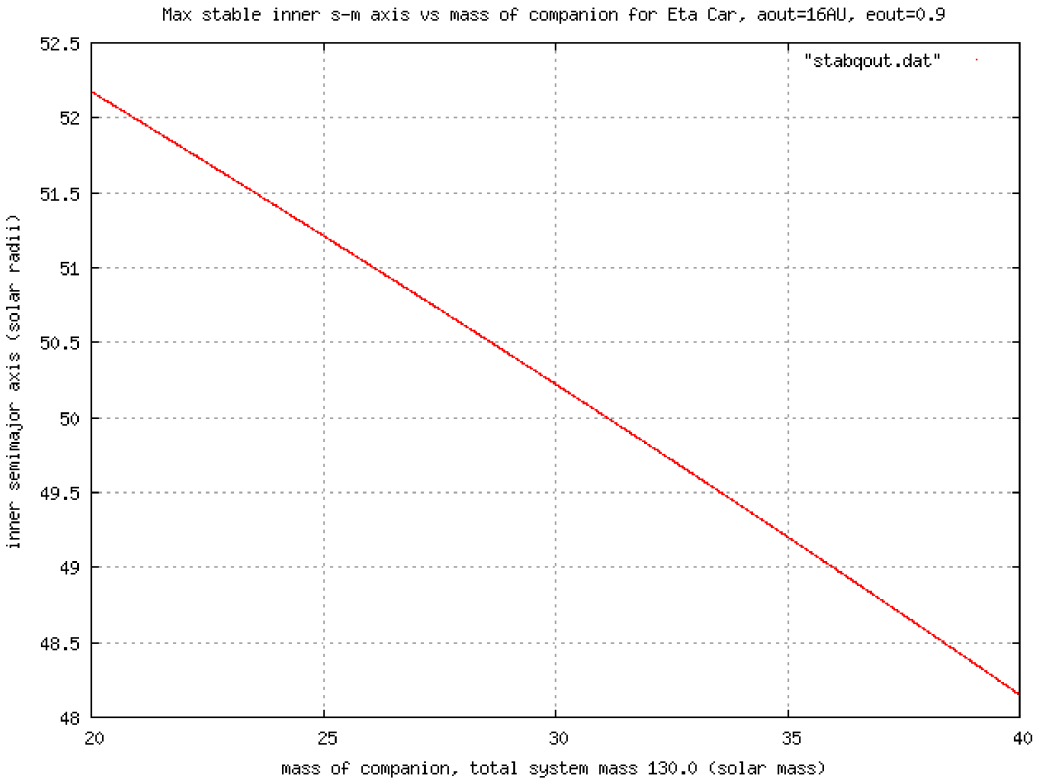

Figure 6.3: Upper limit on stable inner orbit semi major axis versus outer companion mass with an eccentricity of 0.9, from the equations presented in Mardling & Aarseth 1999. The total mass of the system is fixed. The upper limit on the semi-major axis is somewhat sensitive to the outer companion mass ratio.

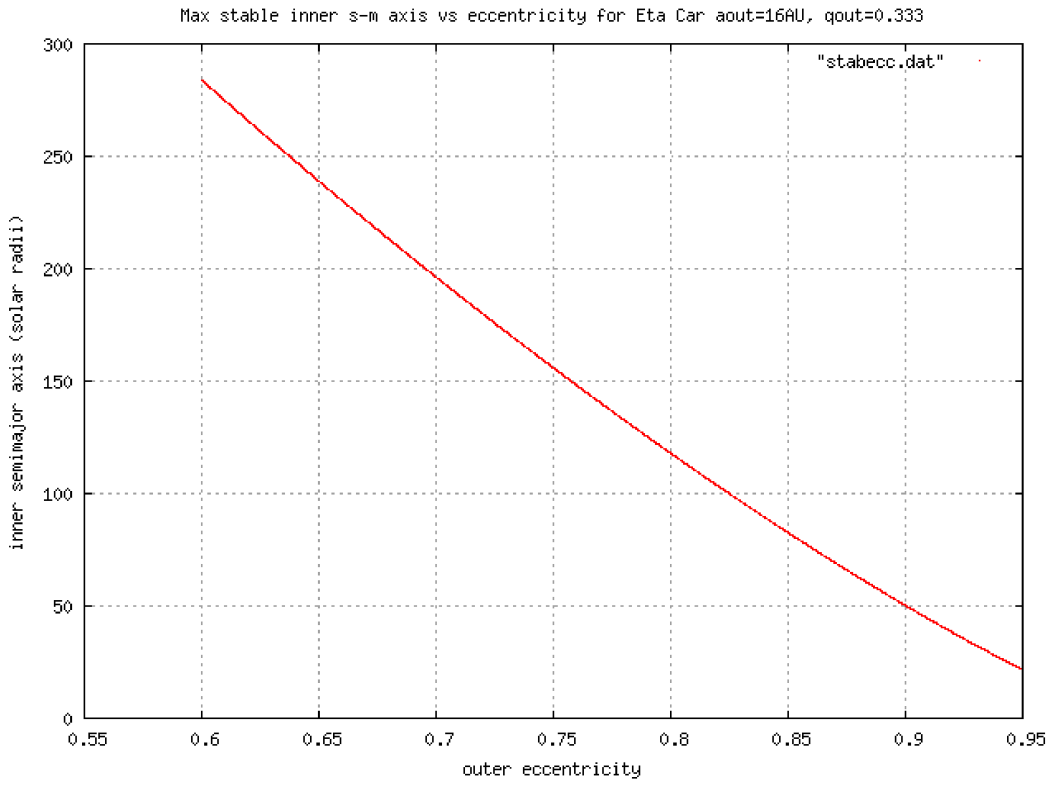

Figure 6.4: Upper limit on stable inner orbit semi major axis versus eccentricity of the companion orbit from the equations presented in Mardling & Aarseth 99, for an outer companion system mass ratio of 0.33. The upper limit is strongly dependent on the companion eccentricity, as it is inevitably bounded by the distance of closest approach. This upper bound varies by a factor of $/tilde4$ in the range 0.7¡e¡0.9 from 200 to 50 solar radii.

Property	Values
Stellar Structure model	realistic, low, high index poly
Fraction of binding energy deposited	0.3
Post-merger wind mass loss	1.6e-3, 3.2e-3, 6.4e-3 $M_{\rm sol}/{\rm yr}$

Table 6.2: Parameters used in these simulations.

We then extrapolate the ejecta from reasonably late times (roughly 2 weeks post energy deposition, at tens of dynamical timescales) to 1 year post eruption, before beginning a wind simulation. This step is purely to manage the transition from stellar radius scales to light year scales in the injection of wind, but is not completely rigorous - future work along these lines would probably contains separate wind simulation phases, or a more flexible framework. We inject a wind based on the c:2000 findings of Smith et al. 2003, with a mass loss rate of $1.6x10^{-3}M_{/odot}/yr$ and an angle-dependent wind as seen in Figure 6.5. We extrapolate at lower latitudes that are observationally incomplete, but do not explicitly include effects due to the interacting winds of the binary which is thought to cause periodic strong disturbances in the plane of the system (for example, see Icke 2010). The fit used, based on a Python polynomial fit routine for selected points on the Smith et al. 2003 dotted fit, can be seen in the corresponding figure, Figure 6.6.

We then run the wind simulation for 150 years (in simulation time) to mimic the Homunculus evolution timescale.

6.8 Results

We study the ejecta from a model star, a low index polytrope and a high index polytrope (the latter two from Chapter 5). The model star ejecta closely resembles the high index polytrope ejecta, which is quite encouraging given the mid-latitude mass loss enhancement in Eta Car, and the parallel feature in the high index polytrope ejecta.

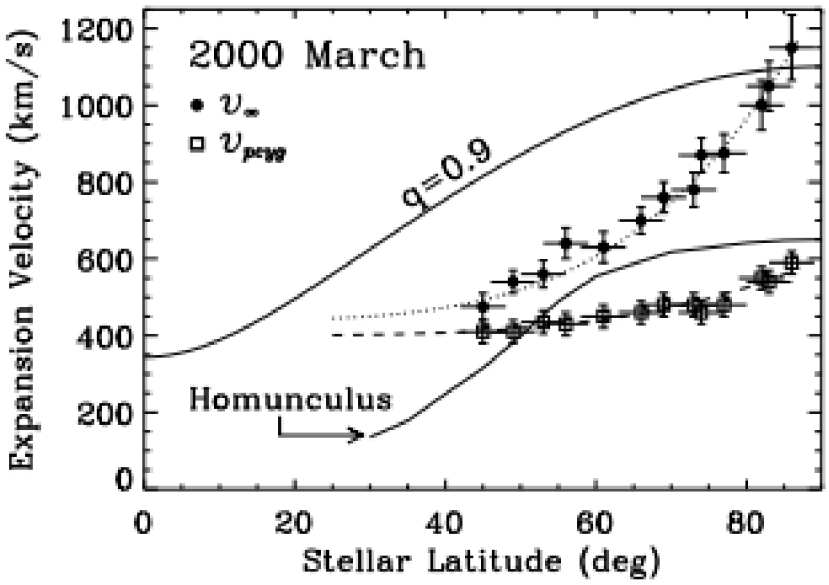

Figure 6.5: Figure 7 from Smith et al. 2003. The filled square points and their dotted fit indicate a significantly bipolar wind which exceeds the Homunculus expansion velocity (lower solid line) at all latitudes and should have had some effect on the evolution of the nebula at the stated observational mass loss rate. In particular , it should have a relatively large effect on the polar lobes at high latitudes compared to mid latitudes where the bulk of the mass lies, and where the disparity between wind velocity and nebular expansion velocity is lower.

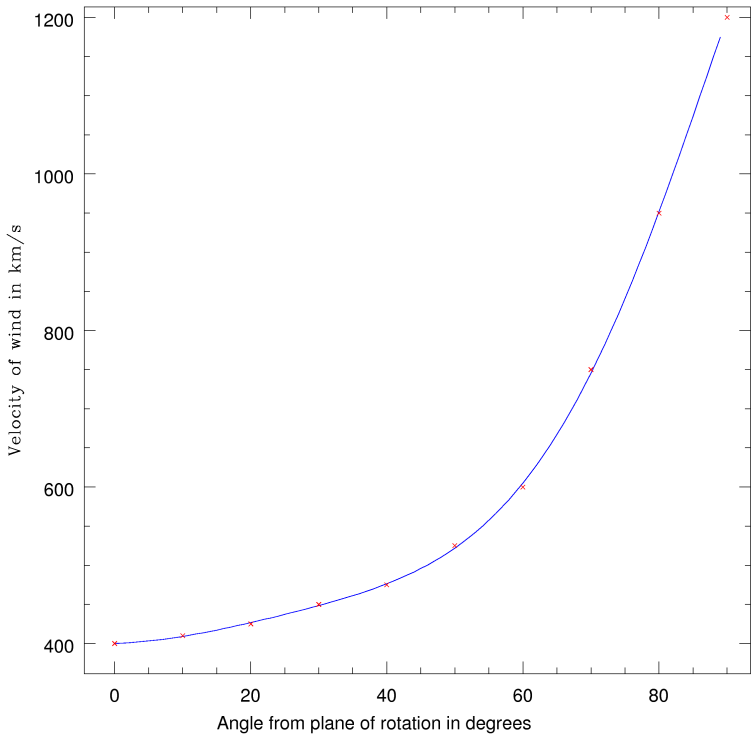

Figure 6.6: A fit (solid line) made with a Python polynomial fit routine, of order 6, to selected points on the dotted fit in Figure 6.5, which are shown in red. We extrapolate an approximately flat velocity profile near the equator, and follow the gradient of the 80-85 fit out to 90 degrees.

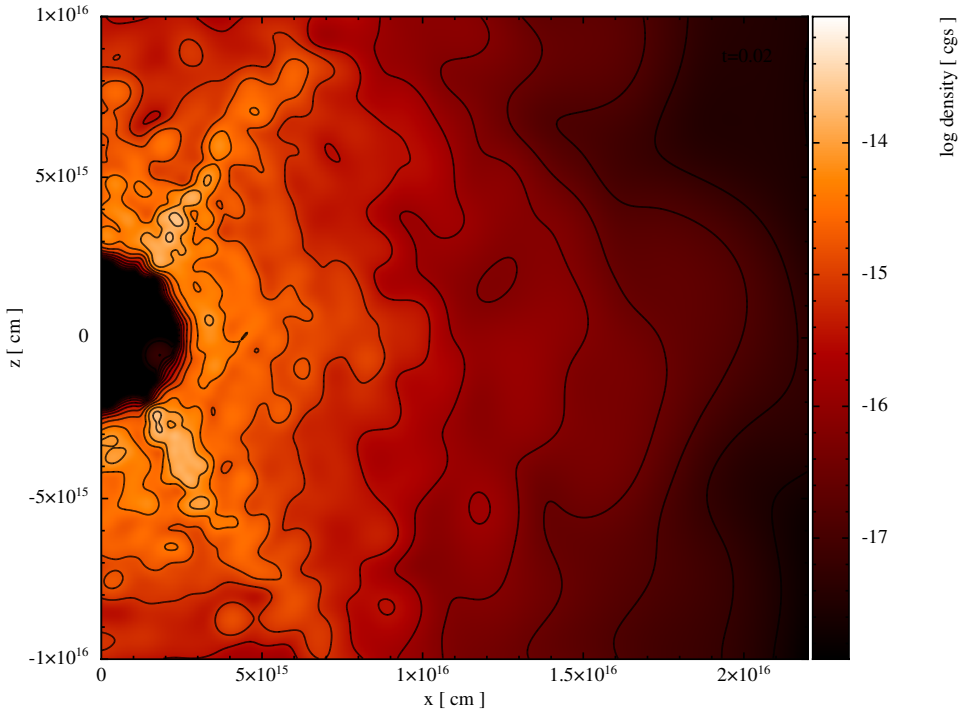

Figure 6.7: Ejecta from the 100 solar mass, 30 solar radii star for an α of 0.3 extrapolated to 1 year post-energy injection.

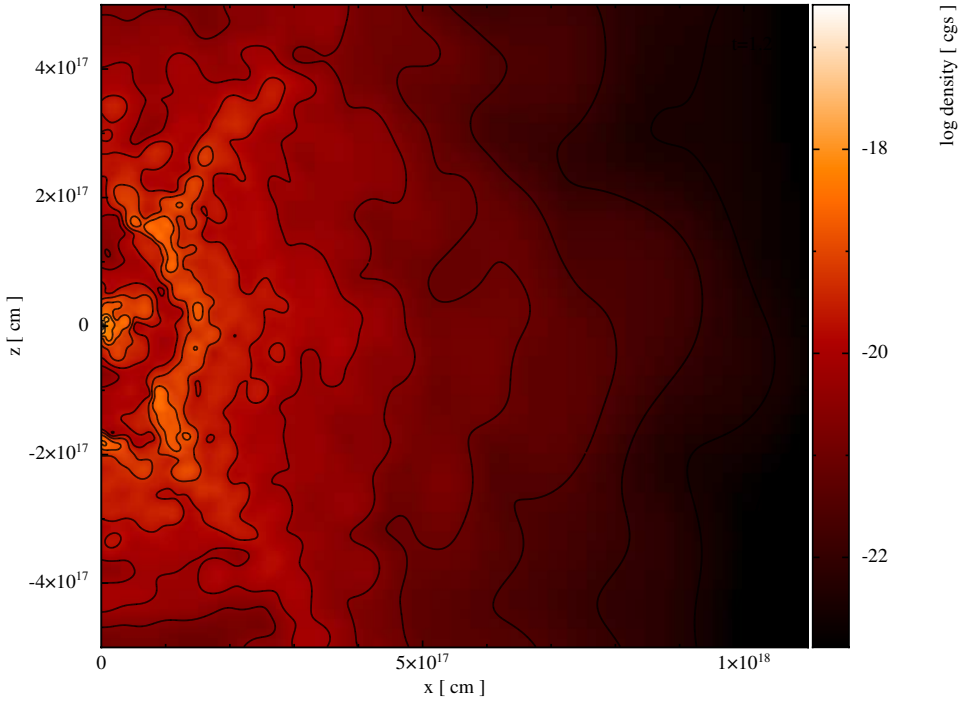

Figure 6.8: Cross section (in y) in cartesian coordinates of the wind simulation of the 100 solar mass, 30 solar radii star, $\alpha = 0.3$ ejecta at 150 years post-energy injection. The inner wind has blown a bubble of the approximate length scale of Eta Carinae's lobes.

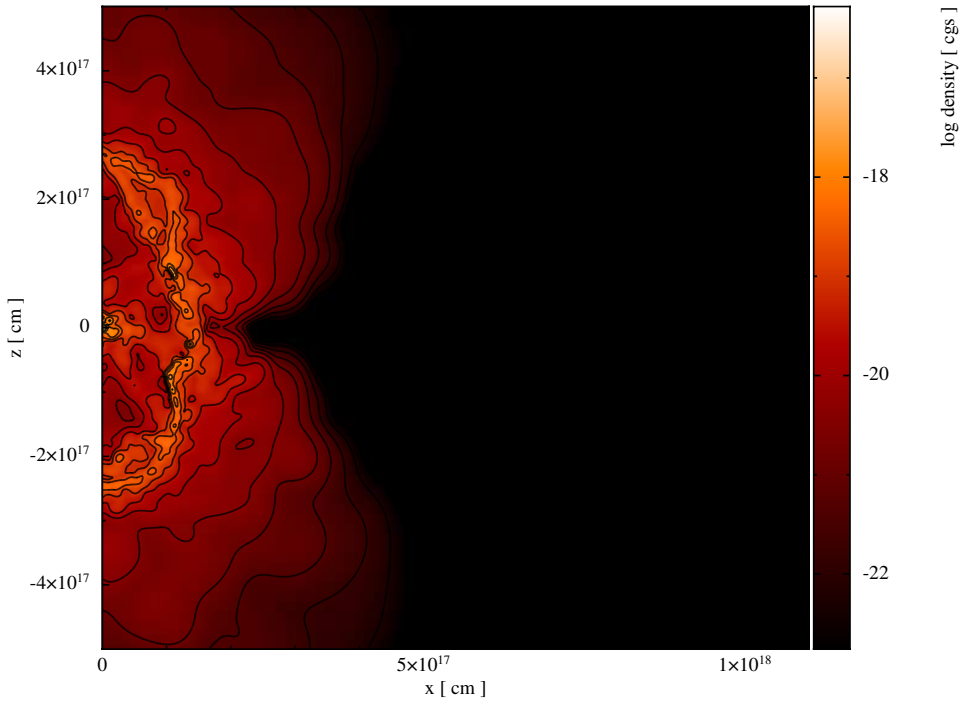

Figure 6.9: Cross section (in y) in cartesian coordinates of a wind simulation of the ejecta produced in Chapter 5 for a low index polytrope star with $\alpha = 0.3$ and moderate angular momentum evolving with a present-day Eta Car wind for 150 years. The wind particles occupy the inner cavity around the origin.

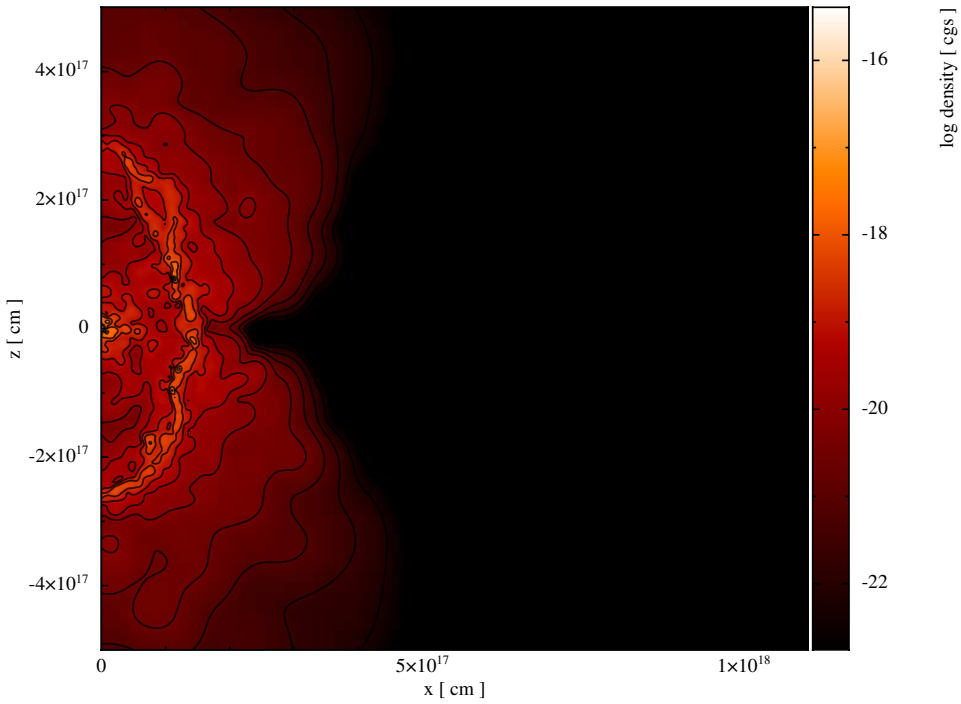

Figure 6.10: As Figure 6.9 - a wind simulation of the ejecta produced in Chapter 5 for a low index polytrope star with $\alpha = 0.3$ and moderate angular momentum evolving with a wind with twice the present-day Eta Car wind mass loss rate for 150 years ($6.4 \times 10^{-3} \mathrm{M}_{\odot} \mathrm{yr}^{-1}$). The wind particles occupy the inner cavity around the origin.

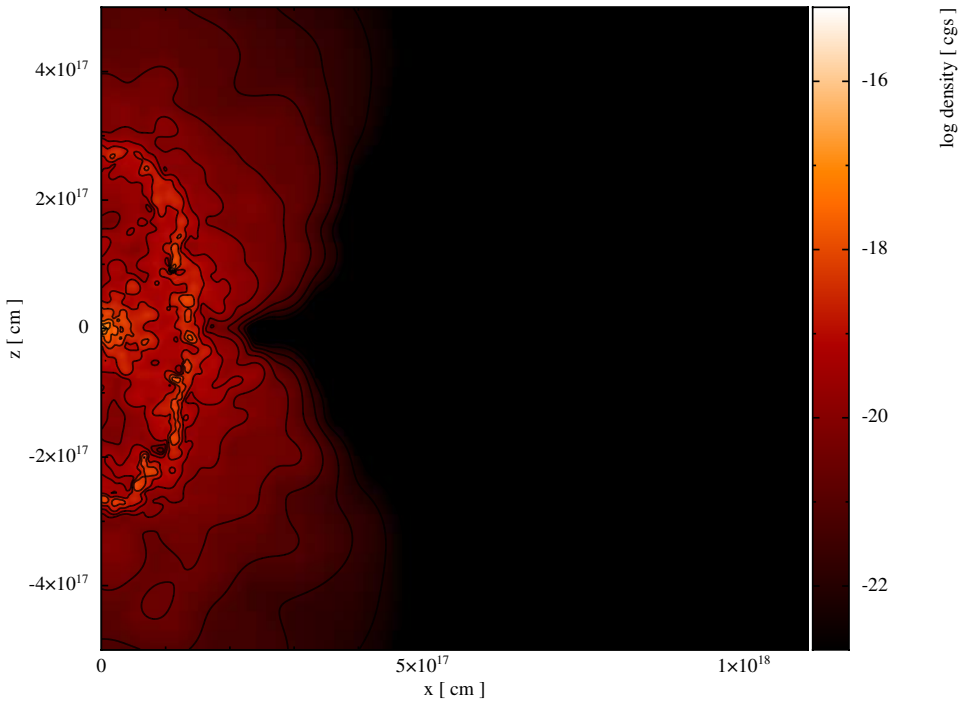

Figure 6.11: As Figure 6.9 - a wind simulation of the ejecta produced in Chapter 5 for a low index polytrope star with $\alpha = 0.3$ and moderate angular momentum evolving with a wind with four times the present-day Eta Car wind mass loss rate for 150 years ($6.4 \times 10^{-3} \mathrm{M}_{\odot} \mathrm{yr}^{-1}$). The wind particles occupy the inner cavity around the origin.

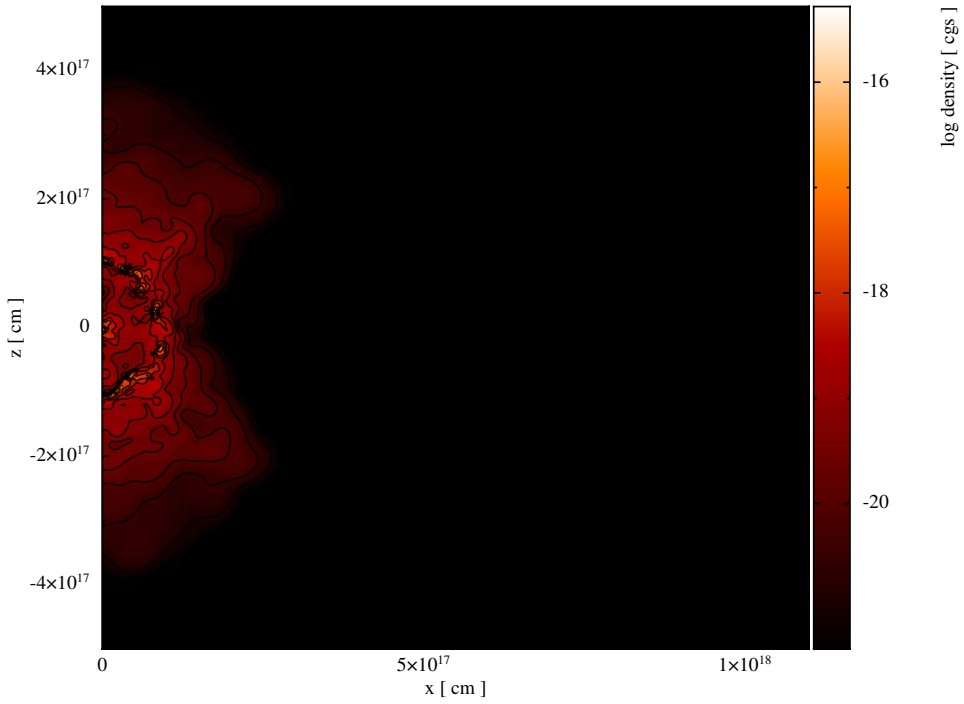

Figure 6.12: A wind simulation of the ejecta produced in Chapter 5, with a velocity scaling of 0.5, for a high index polytrope star with $\alpha = 0.3$ and moderate angular momentum evolving with a present-day Eta Car wind for 150 years. The wind particles occupy the inner cavity around the origin.

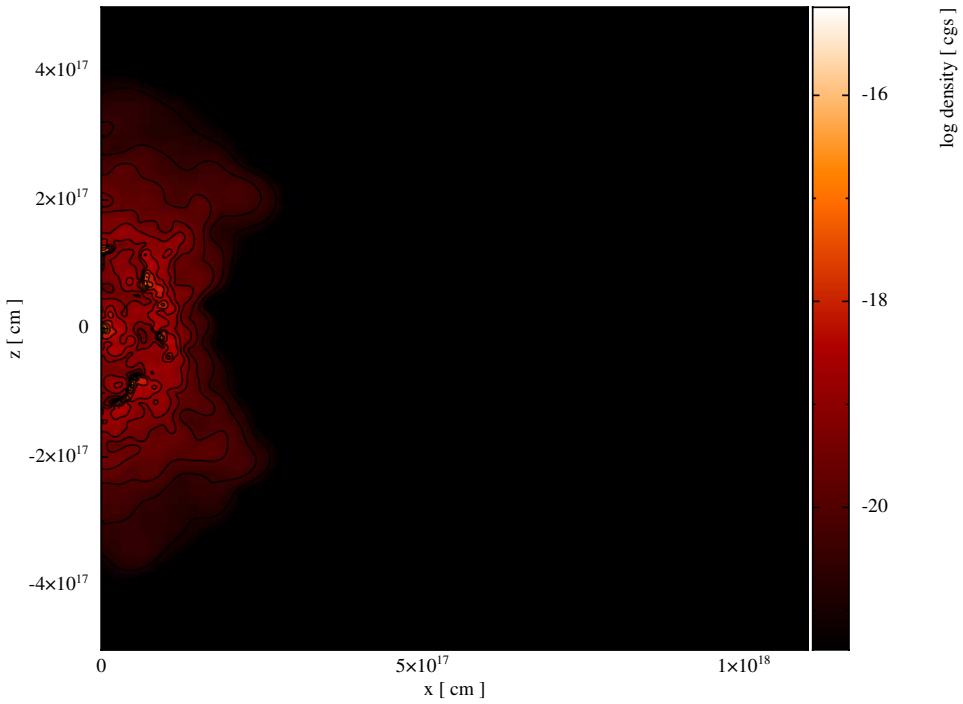

Figure 6.13: As Figure 6.12 - a wind simulation of the ejecta produced in Chapter 5, with a velocity scaling of 0.5, for a high index polytrope star with $\alpha = 0.3$ and moderate angular momentum evolving with a wind with twice the present-day Eta Car wind mass loss rate for 150 years. The wind particles occupy the inner cavity around the origin.

6.9 Discussion and future work

We find that a wind with similar parameters to Eta Car's present wind is sufficient to partly 'inflate' ejecta produced in a similar way to chapter 5 over similar timescales to the time since the Great Eruption. The length scales reached by the inflated lobes, of around 0.25-0.3 light years, is approximately the same as Eta Car's nebula. Ejecta is generally inflated into a rather more spherical shell than double lobed, as equatorial plane ejecta in our models offers less resistance to the merged star wind, even with a bipolar component. With this strength of wind, into these ejecta, we find that the hypothesis is definitely promising, but not necessarily very plausible.

The orbital constraints pose valuable questions as to the viability of this approach, given the size increase in the equatorial plane.

The method above simulates a stellar merger with simple spinup and energy deposition inside a single massive star. While this is appropriate for red giant/white dwarf mergers, or others with large envelope/core ratios, Eta Car is thought to be on the main sequence and so, potentially, were its binary progenitors. Proper, high resolution, full parameter study treatment of stellar mergers is the only satisfactory way to resolve the question of a binary merger for Eta Car.

Chapter 7

Conclusion

It could be argued that the many subjects of investigation in this thesis are too disparate to have a unified conclusion - however the hypotheses presented have a unifying theme, and a unified effect. Where bipolar nebulae are concerned, whether a SNR or eruptive mass loss event or planetary nebula, we have presented a range of simulations arguing the case for a binary origin. While the details differ, essentially we present a range of different ways of creating a preferred axis of mass loss from a binary starting point. Although this is often hard in single stars, especially stars on the AGB or stars which are no longer newborn and magnetically braked, it is a relatively natural product of a binary system - whether it is the axis normal to the orbital plane, through the centre of mass, or the line connecting the two objects.

In Chapter 3, we produced simulations suggesting that the bipolar outer nebulae as revealed by light echoes could be reproduced if early mass transfer in a binary such as that of Morris & Podsiadlowski 2007 produced jets that drove into a pre-existing progenitor wind. The mass transfer jets do not need particularly exotic physics to represent their launch mechanism, as the low mass loss rate and velocity near the companion surface escape velocity means that they could be described as a relatively massive, relatively focused bipolar stellar wind. We argue that the bipolar outer nebulae around SN 1987A is the final piece of evidence for the binary progenitor scenario.

In Chapter 5, we performed a parameter study of ejecta from simplified common envelope models (spun-up polytropes). For lower injections of energy into the interior, and significant angular momentum, the ejecta was strongly bipolar from

the distorted, oblate/toroidal envelopes in both mass and momentum. A range of structures from bi-conical enhancements to polar enhanced figure-8 shapes was produced, depending on the polytropic index of the envelope. Equations of state with different adiabatic indices are suggested to behave substantially differently. This set of simulations, although not performed with any one object in mind, is suggested to be relevant to planetary nebulae and eruptive events such as luminous red novae and Eta Car.

In Chapter 4, we (meaning also Danail Obreschow) tentatively suggest mechanisms for producing a SNR like Cas A, invoking a close binary companion. We initially sought to explain both jets with an offset core collapse within the star (tidally produced by the companion), in close analogy to microgravity fluid droplet implosion which produces this effect with an offset cavity. However, the analogy breaks down, as the conditions are fundamentally different - the equations of state (nearly incompressible water, versus compressible plasma) and the different length and timescale ratios of the core/envelope and cavity/droplet pairs. However, we do find that an offset core will produce a single 'jet' or increased velocity in one direction. We also find that a close binary companion can produce gravitational distortion of supernova ejecta as it passes. These two distortions should be in opposite directions, and together provide an interesting mechanism for producing jets within a supernova remnant such as Cas A.

In Chapter 6, we drove a wind into merger envelope ejecta such as is produced in Chapter 5 to study to what extent a fast double-lobed shell such as in Eta Car can be produced using the very general method of that chapter. We particularly studied the effect of a bipolar-enhanced fast wind (from a putative merger remnant). Although the morphology was not exact, these produced density enhancements or lobes at the approximate length scales of the present day Eta Car Homunculus.

These chapters have the unifying theme of bipolar nebulae from hypothesised binary transients. They also have unifying consequences - binary effects in particular affect both the rates at which various transients could be observed in upcoming and current transient surveys, and if decoded from the observed transients, the binary information could be used to place more constraints on star formation and actual binary rates.

Outside the field of stellar astrophysics (although, arguably, nothing is!), partic-

ularly in the age of rapidly evolving studies of galaxy evolution, a more significant conclusion is that at such time as it is possible to move away from simple parametrisation of mass loss from events such as supernovae, CE ejection and planetary nebulae formation, valuable adjustments could be made to the physics by including the effects of bipolarity and chemical inhomogeneity.

Chapter 8

Bibliography

Abdo A., and the Fermi LAT Collaboration, 2010, ApJ, 710, 1, 92

Arnett D., Meakin C., Young P.A., 2005, ASPC, 332, 75A

Balick B., 1987, ASSL, 132, 413

Belyanin A.A, 1999, A&A, 344, 199

Bhattacharya D. 1996. In Compact Stars in Binaries, IAU Symp., 165th, The Hague

Bionta R.M., Blewitt G., Bratton C.B., Caspere D., Ciocio A., 1987, PhRvL, 58, 1494

Blondin J.M., Lundqvist P., 1993, ApJ, 405, 337

Blondin J.M., Mezzacappa A., DeMarino C., 2003, ApJ, 584, 971

Borve S., Omang M., Trulsen J., 2005, JCoPh, 208, 345

Burrows A., Walder R., Ott C.D., Livne E., 2005, ASP, 332, 350

Burrows A., Livne E., Dessart L., Ott C.D., Murphy J., 2006, ApJ, 640, 878

Burrows C.J. et al, 1994, AAS, 184, 6602

Chesneau, O., Min M., Herbst T., Waters L.B.F.M., Leinert, Ch., Hillier, D.J., Leinert Ch., de Koter A., Pasucci I., Jaffe W., Kohler R., Alvarez C., van Boekel R., Brandner W., Graser U., Lagrange A. M., Lenzen R., Morel S., Scholler M., A&A, 435, 1043

Chevalier R.A., Fransson C., 2003, Lecture Notes in Physics, 598, 171

Chevalier R.A., Kirshner R., 1978, ApJ., 219, 931-941

Chevalier R.A., Kirshner R., 1979, ApJ., 233, 154-162

Chornock R., Filippenko A.V., Li W., Marion G.H., Foley R.J., Modjaz M., Rafelski M., Becker G.D., de Vries W.H., Garnavich P., Jorgenson R.A., Lynch D.K., Malec A.L., Moran E.C., Murphy M.T., Rudy R.J., Russell R.W., Silverman J.M., Steele T.N., Stockton A., Wolfe A.M., Woodward C.E., 2010, arXiv, 1001.2775

Church P., Dischler J., Davies M., Tout C., Adams T., Beer M., MNRAS, 395, 2, 1127-1134

Colgate S.A., Grasberger W.H., White R.H., 1961, AJ, 66S, 280C

Corcoran M. F., 2005, AJ, 129, 2018

Cox, P. et al 1995, A&A, 297, 168

Crotts A.P.S., Kunkel W.E., McCarthy P.J., 1989, ApJ, 347, 61

Damineli A., 1996, ApJ, 460, L49

Damineli A., Kaufer A., Wolf B., Stahl O., Lopes D.F., de Araujo, F., 2000, ApJ, 528, 101

Decin L., Hony S., de Koter A., Justtanont K., Tielens A.G.G.M., Waters L.B.F.M., 2006, A&A, 523, 18

De Luca A., 2007, AIPConfProc, 983, 311

DeLaney T., Rudnick L., Stage M.D., Smith J.D., Isensee K., Rho J., Allen G.E., Gomex H., Kozasa T., Reach W.T., Davis J.E., Houck J.C., 2010, ApJ, 725, 2038

Dorland B.N., Currie D. G., Hajian A. R., 2003, AAS, 203, 5812

Duncan R. A., White S. M., 2003, MNRAS, 338, 425

Dwarkadas V.V., Owocki S.P., 2001, AAS, 19913512

Eggleton PP. 1983. ApJ. 268:368?69

Fesen R., 2001, ApJ. Supp., 133, 161

Fesen R., Hammell, M. C., Morse J., Chevalier R., et al., 2006., ApJ., 645, 283-292

Frank A., Balick B., Davidson K., 1995, ApJ, 441, 77

Frank A., Ryu D., Davidson K., 1998, ApJ, 500, 291

Gingold R.A., Monaghan J.J., 1977, MNRAS, 181, 375

Gingold R.A., Monaghan J.J., 1982, CoPh, 46, 429

Gregg M.D., Kimble R., Davidsen A.F., 1985, BAAS, 19, 734G

Groenewegen M.A.T., Sloan G.C., Soszynski I., Petersen E. A., 2009, A&A, 506, 1277

Hammell M.C., Fesen R.A., 2008, ApJ, 179, 195

Heinke C.O., Ho W.C.G., 2010, ApJ, 719, 167

Hernquist L., Katz N., 1989, ApJ, 70, 419

Hillebrandt W., Meyer F., 1989, A&A, 219, 3

Hillier D. J., Davidson K., Ishibashi K., Gull T., 2001, ApJ, 553, 837

Hillier D. J. et al., 2006, ApJ, 642, 1098

Hirata K., Kajita T., Koshiba M., Nakahata M., Oyama Y, 1987, PhRvL, 58, 1490

Hjellming MS, Webbink RF. 1987. ApJ. 318:794?808

Hughes D., 1980, Nature, 285, 132-133

Hughes J.P., Rakowski C.E., Burrows D.N., Slane P.O., 2000, ApJ, 528, 109

Hwang U., Laming J.M., 2009, ApJ, 703, 883

Hwang U., Laming J.M., Badenes C., Berendse F., et al., 2004., ApJ., 615, 2, L117-120

Ishibashi, K., et al. 2003, AJ, 125, 3222

Janka H.Th., Langanke K., Marek A., Martinez-Pinedo G., Muller B., 2007, PhR, 442, 38J

Kalogera V., 1997, PhD Thesis, AAT 9812647

Kim Y., Rieke G.H., Krause O., Misselt K., Indebetouw R., Johnson K.E., 2008, ApJ, 678, 287

King AR, Begelman MC. 1999. ApJ. 519:L169?71

Kitsionas S., 2003, PhD thesis, Cardiff University

Krause O., Birkmann S., Usuda T., et al., 2008, Science, 320, 1195-1197

Krause O., Rieke G.H., Birkmann S.M., Le Floc’h E., Gordon K.D., Egami E., Bieging J., Hughes J.P., Young E.T., Hinz J.L., Quanz S.P., Hines D.C., 2005, Science, 308, 5728

Kulkarni S. R., Ofek E. O., Rau A., Cenko S. B., Soderberg A. M., Fox D. B., Gal-Yam A., Capak P. L., Moon D. S., Li W., Filippenko A. V., Egami E., Kartaltepe J., Sanders D.B., 2007, Nature, 447, 458-460

Langer, N., Garcia-Segura, G., Mac Low, M-M., 1999, 520, 49

Lloyd H.M., O'Brien T.J., Kahn F.D., 1995, MNRAS, 273, 19

Lucy L.B., 1977, AJ, 82, 1013

Luo D., McCray R., 1991, BAAS, 23, 1406

Lyne A.G., Lorimer D.R., 1994, Nature, 369, 127L

Maeder A., Desjacques V., 2001, A & A, 372, 9

Maran S.P. et al, 2000, ApJ, 545, 390

Mardling R., Aarseth S.J., 1999,
The Dynamics of Small Bodies in the Solar System,
ed. B.A. Steves & A.E. Roy (Dordrecht: Kluwer), 385

Mason E., Diaz M., Williams R. E., Preston G., Bensby T., 2010, A&A,
516, 108

Matt S., Balick B., 2004, ApJ, 615, 921

Matheson T., Filippenko A.V., Barth A.J., et al., 2000, ApJ, 120,
1487-1498

Matheson T., Filippenko A.V., Ho L.C., Barth A.J., Leonard D.C., 2000,
AJ, 120, 1499

Menzies J. W. et al. 1987, MNRAS, 227, 39

Minkowski R., 1968, "Stars and Stellar Systems", 7, 63

Morris, M. 1981. ApJ. 249: 572

Morris P. W. et al., 1999, Nature, 402, 502

Morris T., DPhil thesis, University of Oxford, 2005

Morris T., Podsiadlowski Ph., 2006, MNRAS, 365, 2-10

Morris T., Podsiadlowski Ph., 2007, Science, 315, 1103

Morris T., Podsiadlowski Ph., 2009, MNRAS, 339, 515

Morse J. A., Davidson K., Bally J., Ebbets D., Balick B., Frank A., 1998, AJ, 116, 2443

Morse J. A., Kellogg J. R., Bally J, Davidson K, Balick B, Ebbets D., 2001, ApJ, 548L 207M

Nordhaus J., Burrows A., Almgren A., Bell J., 2010, ApJ, 720, 694

Nordhaus J., PhD thesis, University of Rochester, 2008

Nozawa T., Kozasa T., Tominaga N., Maeda K., Hideyuki U., Ken'ichi N., Krause O., 2010, ApJ, 713, 356

Ona-Wilhelmi E., Vitale V., Cortina J., Mankuzhiyil N., Robert A., Torres D.F., MAGIC Collaboration, 2007,
Proceedings of the 30th International Cosmic Ray Conference, 2, 683

Ostriker JP. 1975. The Structure and Evolution of Close Binary Systems, IAU Symp., 73rd, Cambridge

Owocki S. P., Gayley K.G., Cranmer S.R., 1998, ASPC, 131, 2370

Paczynski B. 1976. In The Structure and Evolution of Close Binary Systems, IAU Symp.,73rd, Cambridge,ed. P Eggleton, S Mitton, J Whelan, pp. 75

Panagia N., 1999, IAUS, 190, 549

Panagia N. et al, 1996, ApJ, 459, 17

Phillips M.M., Heathcote S.R., Hamuy M., Navarrete M., 1988, AJ, 95, 1087

Plait P.C. et al, 1995, ApJ, 439, 730

Podsiadlowski Ph., 1992, PASP, 104, 717

Podsiadlowski Ph., Fabian A.C., Stevens I.R., 1991, Nature, 354, 43

Podsiadlowski Ph., Ivanova N., 2003, ASPC, 304, 339

Podsiadlowski Ph., Joss P.C., Rappaport S., 1990, A&A, 227, 9

Price D., 2007, Publ. Astron. Soc. Aust., 24, 159-173

Price D., 2008, J. Co. Ph., 227, 10040

Quinn T., Paczynski B., 1985, ApJ, 289, 634

Rest A., Foley R.J., Sinnott B., Welch D.L., Badenes C., Filippenko A.V., Bergmann M., Bhatti W.A., Blondin S., Challis P., Damke G., Finley H., Huber M.E., Kasen D., Kirshner R.P., Matheson T., Mazzali P., Minniti D., Nakajima R., Narayan G., Olsen K., Sauer D., Smith R.C., Suntzeff N.B., 2011, ApJ, 732, 3

Rest A., Sinnott B., Welch D. L., Foley R.J., Narayan G., Mandel K., Huber M.E., Blondin S., 2011, ApJ, 732, 2

Rho J., Jarret T.H., Chugai N.N., Chevalier R.A., 2007, 666, 1108

Ritter H. 1976, MNRAS, 175, 279, 95

Rosswog S. 2009, New Astronomy Reviews, 53, 4-6, 78

Ryle M., Smith G., 1948, Nature, 162, 462-463

Saleh L., Rasio F., 2009, ApJ, 694, 1566-1576

Schure K.M., Vink J., Garcia-Segura G., Achterberg A., 2008, 686, 399

Soker N., 2001, MNRAS, 325, 584

Soker N., 2003, IAU Symp, 20, 323,
Soker N., 2005, ApJ, 619, 1064

Soker N., 2007, ApJ, 661, 490

Soker N, Livio M 1988. ApJ. 339: 268-278

Sonneborn G., Kirshner R., Morel M., McNaught R., 1987, IAUC, 4366, 1

Smith N., 2002, MNRAS, 337, 1252

Smith N., 2006, ApJ, 644, 1151

Smith N., Ferland G. J., 2007, ApJ, 655, 911

Smith N., Gehrz R. D., Hinz P. M., Hoffmann W. F., Hora J. L., Mamajek E. E., Meyer M. R., 2003b, AJ, 125, 1458

Smith N., Morse, J. A., 2004, ApJ, 605, 854

Smith N., Townsend R.H.D, 2007, ApJ, 666, 967

Soker N., 2004, ApJ, 612, 1060

Soker N., 2005, ApJ, 619, 1064

Springel V., 2005, MNRAS, 364, 1105

Springel V., Hernquist L., 2002, MNRAS, 333, 649

Sugerman B. et al, 2005, ApJS, 159, 60

Taam R. E., Sandquist E. L., 2000, ARA&A, 38, 113

Tananbaum H., 1999, IAU Circ., 7246

Thorstensen J., Fesen R., van den Bergh S., 2001, AJ, 122, 297

Townsend R.H.D., MacDonald J., 2006, MNRAS, 368, 57

Tylenda R., Hajduk M., Kaminski T., Udalski A., Soszynski I., Szymanski M. K., Kubiak M., Pietrzynski G., Poleski R., Wyrzykowski L, Ulaczyk K., 2011, A&A, 528, 114

van Dyk, S. D., 2005, ASPC, 332, 47

van Veelen B., Langer N., Vink J., Garcia-Segura G., van Marle A.J., 2009, A&A, 503, 495

Verner E., Brhuhweiler F. B., Gull T. R., 2005, ApJ, 624, 973

Vink J., Kaastra J.S., Bleeker J.A.M., 1996, A&A, 307, 41

Vogt F., Dopita M.A., 2010, ApJ, 721, 597

Wang L., Mazzali P., 1992, Nature, 355, 58

Weigelt G., Ebersberger, J., 1986, A&A, 163, 5

Weis K., 2005, ASPC, 332, 271W

Wheeler J.C., Maund, J.R., Couch S.M., 2008, ApJ, 677, 1091

White G.L., Malin D.F., 1987, Nature, 327, 36

Whitworth A.P., 1888, MNRAS, 296, 442

Willingale R., Bleeker J.A.M., van der Heyden K.J., Kaastra J.S., 2003, A&A, 398, 1021

Woosley S.E., 1987, BAAS, 19, 740

Woosley S.E., Janka H.-T., 2005, Nature Physics, 1, 147

Woosley S.E., Pinto P.A., Weaver T.A., 1988, PASA, 7, 355

Chapter 9

Appendices

9.1 Geometric Warping

9.1.1 Introduction

In order to produce a radial density profile from a uniform SPH glass, it is usual to divide the profile into discrete bins with a certain number of particles each. Starting from an arbitrary point, a search iterating out in radius to gather the particles into the correct radial bin is made. In the case of simple profiles such as $\rho \propto \frac{1}{R^2}$, I wondered if a global transform applied to the radial coordinate of the particles could produce the requisite density profile. I discovered through trial and error that cubing the radial coordinate ($R_{i_{\rm new}} = R^3_{i_{\rm old}}$) produced the $\rho \propto \frac{1}{r^2}$, then the following values for other profiles (Table (9.1.1).

I found the cubed radial coordinate approach above ($n = 2$,$m = 3$) in the

n	m
3	not found
2	3
1	1.5
0	0 (triv)
-1	0.75

Table 9.1: Numerically found transforms to produce radial density profiles: n from ($\rho \propto R^{-n}$, m is $R_{i_{new}} = R^m_{i_{old}}$)

literature, but did not find an analytical justification. I derived it myself, and found the equation linking m and n below - in the next section is the derivation.

$$m = \frac{3}{3-n} \tag{9.1}$$

9.1.2 Derivation

A density distribution of the form

$$\rho = kR^{-n} \tag{9.2}$$

where $n \neq 0$ and k is a constant, has mass interior to a radius R of

$$M(< R) = \frac{4\pi k R^{3-n}}{3-n} \tag{9.3}$$

and can be defined, relative to others of its type by

$$\frac{M(< 2R)}{M(< R)} = 2^{3-n} \tag{9.4}$$

which characterises the distribution as R is scalable to any value. The challenge is to apply a transform of the form

$$R_{i_{\text{new}}} = R^m_{i_{\text{old}}} \tag{9.5}$$

with a certain m, to a uniform distribution such that it follows equation (9.1.2) for a given n. In a uniform distribution ($\rho(R) = const$), the mass interior to a radius R is

$$M(< R) = \frac{4\pi k R^3}{3}. \tag{9.6}$$

The required distribution requires that a certain fraction of mass be interior to R compared to within $2R$. We therefore need to find the radius $\alpha 2R$,$0 < \alpha < 1$ in the uniform distribution which contains this fraction. Whichever transform $R_{i_{\text{new}}} =$

$R^m_{i_{\rm old}}$ makes this radius $\alpha 2R$ equal to R is therefore the correct one.

So we need

$$\frac{M(<2R)}{M(<\alpha 2R)} = 2^{3-n} \tag{9.7}$$

and have

$$\alpha^m = \frac{1}{2}. \tag{9.8}$$

We know that

$$M(<\alpha 2R) = \frac{4\pi k 2^3 \alpha^3 R^3}{3} \tag{9.9}$$

and so

$$\frac{M(<2R)}{M(<\alpha 2R)} = \frac{1}{\alpha^3} = 2^{3-n} \tag{9.10}$$

$$\alpha = \frac{1}{2^{\frac{3-n}{3}}} \tag{9.11}$$

from equation (9.1.2),

$$\frac{1}{2^{\frac{3-n}{3}}} = \frac{1}{2^{1/m}} \tag{9.12}$$

and so equating powers of 2:

$$m = \frac{3}{3-n}. \tag{9.13}$$

QED